# Development and Numerical Prediction of a Comprehensive Analytical Model of an Indirect-Internal-Reforming Tubular SOFC

AUTHOR(S):

Nishino, Takafumi

Master Thesis

# Development and Numerical Prediction of a Comprehensive Analytical Model of an Indirect-Internal-Reforming Tubular SOFC

**by**

**Takafumi NISHINO**

Department of Mechanical Engineering
Graduate School of Engineering
Kyoto University

February 9, 2004

# Abstract

A comprehensive analytical model of an indirect internal reforming type tubular Solid Oxide Fuel Cell (IIR-T-SOFC) has been developed. Two-dimensional axisymmetric multicomponent gas flow fields and quasi-three-dimensional electric potential/current fields in the tubular cell are simultaneously treated in the model with consideration of the involved phenomena such as internal reforming, electrochemical reactions and radiative heat transfer. By using this model, the characteristics of the operating state of an IIR-T-SOFC were numerically examined. As a result, it was shown how the thermal field and power generation characteristics of the cell were affected by the gas inlet temperature, air flow rate, steam-methane ratio, reforming catalyst distribution and thickness of the electrodes. In particular, the optimized catalyst distribution greatly reduced both the maximum temperature and temperature gradients of the cell with little negative impact on the power generation performance of the cell.

# Contents

# Chapter 1

# Introduction

With the rapid progress of computer technology in these years, numerical analysis has become an "easy-to-use" tool for academic research and technical development of fuel cells, which are expected to play an important role as clean and efficient energy conversion devices in the near future. Simulation of the fuel cells, however, is essentially very complicated due to a variety of phenomena involved in them such as multicomponent gas flow, heat/mass transfer, electrochemical reactions and generation of the electric current. Therefore, how to model those involved phenomena is a critical issue in the numerical analysis of the fuel cells. Improving the model should lead to increase in the "real utility" of the numerical analysis, and consequently to advance in the fuel cell technologies. From this viewpoint, an original comprehensive numerical model of an indirect internal reforming type tubular Solid Oxide Fuel Cell (IIR-T-SOFC) has been developed in the present study. The first objective is to propose an appropriate numerical analytical method applicable to a wide variety of fuel cells, and the second one is to actually examine the feasibility of this advanced type of fuel cells.

Among several types of fuel cells, Solid Oxide Fuel Cells (SOFCs) have an advantage that they can operate with not only hydrogen but also common hydrocarbon fuels. This is due to the oxide ion conductivity of the electrolyte. High operation temperature is also a major advantage of the SOFCs, which makes it possible to employ hybrid systems with gas turbines or the like, and accordingly to improve overall energy conversion efficiencies [1][2]. In addition, steam reforming of the hydrocarbon fuels is possible in the SOFC systems with the aid of the high operation temperatures. When the reforming reaction takes place on the anode of the cell with heat and steam supplied directly from the electrochemical reaction, the process is referred to as direct internal reforming (DIR). In this case, the cell structure is relatively simple because no additional catalyst except the anode is needed. However, there are still some difficulties in properly controlling both reforming and electrochemical reactions with the anode itself [3][4][5]. On the other hand, the case in which the reforming reaction proceeds on the catalysts added inside the system but apart from the anode is referred to as indirect internal reforming (IIR). In this case, a variety of commercial materials can be used as a catalyst for the reforming reaction. Furthermore, it could be possible to control the thermal field in the system by the endothermic effect of the reforming reaction, judging from the earlier studies [6][7][8].

Another advantage of the SOFCs is that the electrolyte is solid, not liquid. This results in the geometric flexibility of the cell. At present there are several types of the cells proposed and tested for the SOFCs. Among them, tubular-type SOFCs are one of the most practically developed ones. The two major advantages of the tubular cells are that they have relatively

good thermal shock resistance and that there is no need for special sealing treatment. Owing to these advantages, a long-term operation test of an atmospheric pressure 100-kW tubular SOFC system has been successfully performed [9]. In this conventional system, natural gas fuel is fully reformed in "in-stack" reformers, which are placed between the cell bundle rows composed of many tubular cells and heated indirectly by them (hence, this SOFC system is also referred to as a kind of IIR-T-SOFC systems).

The concept of the IIR-T-SOFCs to be focused on in this study is that the hydrocarbon fuels are reformed indirectly in "each" tubular cell, rather than in the conventional in-stack reformers or the like. In the present case, the cell structure becomes a little more complicated in geometry due to the catalyst to be embedded in it, but the stack structure becomes fairly simple. That is, arbitrary number of the cells can be stacked both in electrical series and parallel in principle because there are no in-stack reformers. This should be a great advantage in producing SOFC systems of various output levels. Additionally, it could become possible with this type of fuel cell to control the thermal field in the system on a "per-cell" basis depending on how the catalyst is allocated in the cell. At present this type of fuel cell is just an idea, therefore it should be so meaningful to study the feasibility of it numerically.

For the development process of the high-temperature fuel cell systems, to predict the cell thermal field in detail is particularly important in order to avoid the risk of thermal crack failures caused by excessively high temperatures and too-large temperature gradients. At the same time, to figure out the details of the power generation characteristics of the cell is also very useful for further improvement of the energy conversion efficiencies of the system. Those detailed information on the operating state of the cell, however, cannot be obtained by general experimental methods. This is also the reason why numerical analysis is suitable for the research of the fuel cells. Only recently have the numerical studies on the IIR-T-SOFCs been reported in literature, such as Aguiar et al. [7] and Nagata et al. [10]. However, the numerical models used in their studies were rather simplified ones. For example, the multicomponent thermo-fluid field within the cell was basically treated as one-dimensional in their models. In order to achieve the maximum benefit from the numerical analysis, all the involved phenomena within the cell need to be modelled as accurate as possible because they are closely related to each other. Hence in the present study, two-dimensional axisymmetric gas flow field and quasi-three-dimensional electric current field in the cell have been simultaneously considered in the model. Moreover, all the effects of the internal reforming, electrochemical reactions, radiative heat transfer and porous media flow have been properly taken into account. In the following chapters, general remarks on the mechanism of the IIR-T-SOFCs will be described first, then the details of the model will be explained in a methodical way, and finally the calculated results, especially for the thermal field and power generation characteristics of the cell, will be examined.

# Chapter 2

# General Remarks on the Mechanism of IIR-T-SOFC

Prior to describing the numerical modelling and the simulated results, general remarks on the mechanism of the IIR-T-SOFCs will be given in this chapter. In contrast to the conventional tubular SOFCs extensively developed in some industrial firms such as Siemens Westinghouse Power, the IIR-T-SOFCs to be examined in this study are one of the most advanced (but not matured) types of fuel cells. Many advantages are shared with the conventional SOFCs (e.g. high operating temperature, oxide ion conductivity of the electrolyte, etc.) while the concept of indirect internal reforming in "each" cell is unique and less well known. Hence the mechanism of the IIR-T-SOFCs, particularly for the cell structure and internal reforming/electrochemical reactions, will be described below.

## 2.1 Tubular Cell

Figure 2.1 shows a schematic view of a single cell of IIR-T-SOFCs to be focused on in the present study. The cell consists of a cell tube and a feed tube, basically following a design of conventional tubular SOFCs [11]. The cell tube is composed of anode, cathode, electrolyte and support layers. Electrochemical reactions take place inside and outside the cell tube, and then electricity is generated accordingly. The variation from the conventional cell design is that the feed tube is filled with a porous medium containing the catalyst for the steam reforming, and that the hydrocarbon fuel, not air, flows inside the feed tube to be reformed "indirectly" in each tubular cell. That is to say, the fuel is reformed inside the feed tube, changes flow direction at the closed end of the cell tube, reacts electrochemically on the anode, and then flows out of the cell. Meanwhile, air flows outside the cell tube and reacts on the cathode. One drawback of this cell design is that the interconnects are exposed to the high-temperature air, that can cause serious oxidization of the interconnects. However, this problem is being resolved due to the development of new interconnect materials such as doped-lanthanum chromite series in recent years [12][13].

This tubular cell is stacked in both electrical series and parallel direction as shown in Fig. 2.2. The number of the cells can be decided depending on the required output power. When the number of the cells is sufficiently large, the operating condition of each tubular cell should be almost the same except for the cells located on the peripheral part of the stack. In other words, most of the cells are expected to be equally burdened. This is a big advantage in terms

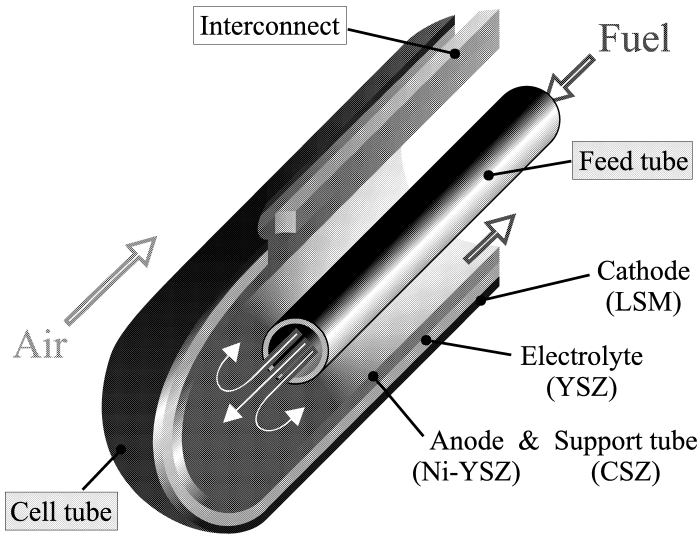


Figure 2.1: Schematic view of a single cell of IIR-T-SOFCs.

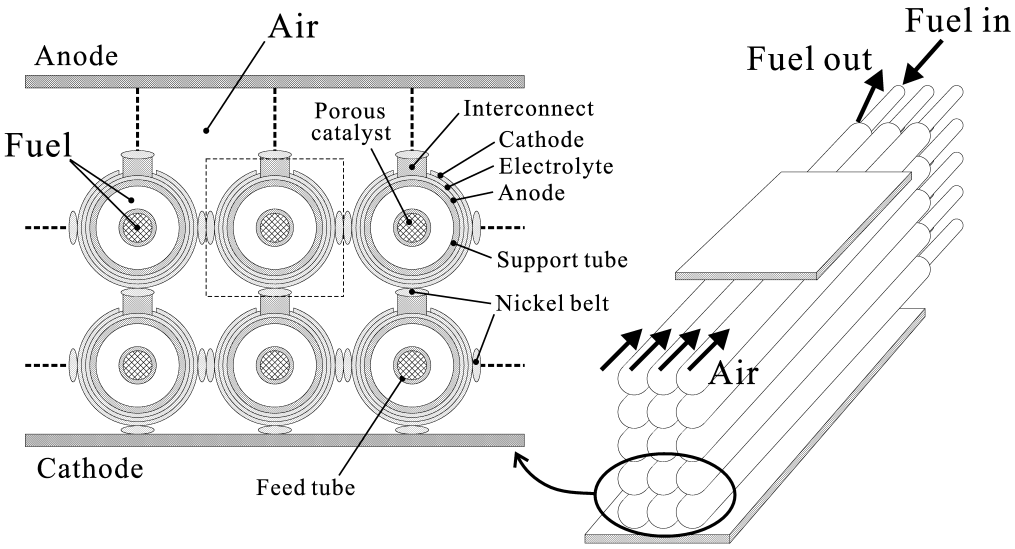


Figure 2.2: Schematic view of a cell stack.

of both design and maintenance of the cells because there is no need to consider where they are positioned in the cell stack. Therefore, the most important issue in the development of such IIR-T-SOFCs is to figure out the complicated phenomena seen in each tubular cell, which is the reason why a single cell, not a cell stack, is focused on in this study.

## 2.2 Internal Reforming Process

One of the important phenomena which take place in the tubular cell is the internal reforming of fuel. As mentioned above, the tubular cell is designed to reform hydrocarbons inside the feed tube. Although there are a variety of hydrocarbon fuels, only methane, a major component of natural gas, is focused on as fuel in this study.

For the methane fuel, methane-steam reforming process is widely known as a conventional process for producing hydrogen [14][15]. This reforming process, which takes place on the catalysts such as nickel-alumina, can be described by the following two chemical reactions:

≪ Steam Reforming of $CH_4$ ≫

$$CH_4 + H_2O \longleftrightarrow 3H_2 + CO \tag{2-1}$$

≪ Shift Reaction of CO ≫

$$CO + H_2O \longleftrightarrow H_2 + CO_2 \tag{2-2}$$

The steam reforming reaction, described by eqn (2-1), is a strongly endothermic reaction. From the viewpoint of chemical equilibrium, the methane is almost totally reformed at the operation temperature of the SOFCs, 700°C or higher in general. In other words, the equilibrium constant of the steam reforming is very large at such high temperatures. However, the reaction rate depends on not only temperature but also partial pressure of each chemical species and amount of the catalysts. Therefore, how the methane is reformed inside the feed tube is highly dependent on those locally-variable factors. Meanwhile, the water-gas shift reaction, described by eqn (2-2), is a weak exothermic reaction. Hence the equilibrium constant becomes larger as temperature becomes lower. Additionally, the shift reaction is always close to the equilibrium in the entire fuel path because the reaction rate is much faster than that of the steam reforming.

## 2.3 Electrochemical Process

Another important phenomenon in the tubular cell is a series of events associated with the electrochemical reaction. In the case where methane is used as fuel and is totally reformed inside the feed tube, the electrochemical process on the anode and cathode can be described by the following reactions:

≪ Anode Reaction of $H_2$ ≫

$$H_2 + O^{2-} \longrightarrow H_2O + 2e^- \tag{2-3}$$

≪ Anode Reaction of CO ≫

$$CO + O^{2-} \longrightarrow CO_2 + 2e^- \tag{2-4}$$

≪ Cathode Reaction of $O_2$ ≫

$$\frac{1}{2}O_2 + 2e^- \longrightarrow O^{2-} \tag{2-5}$$

These anode and cathode reactions are also described collectively as follows:

≪ Electrochemical Reaction of $H_2$ and $O_2$ ≫

$$H_2 + \frac{1}{2}O_2 \longrightarrow H_2O \tag{2-6}$$

≪ Electrochemical Reaction of CO and $O_2$ ≫

$$CO + \frac{1}{2}O_2 \longrightarrow CO_2 \tag{2-7}$$

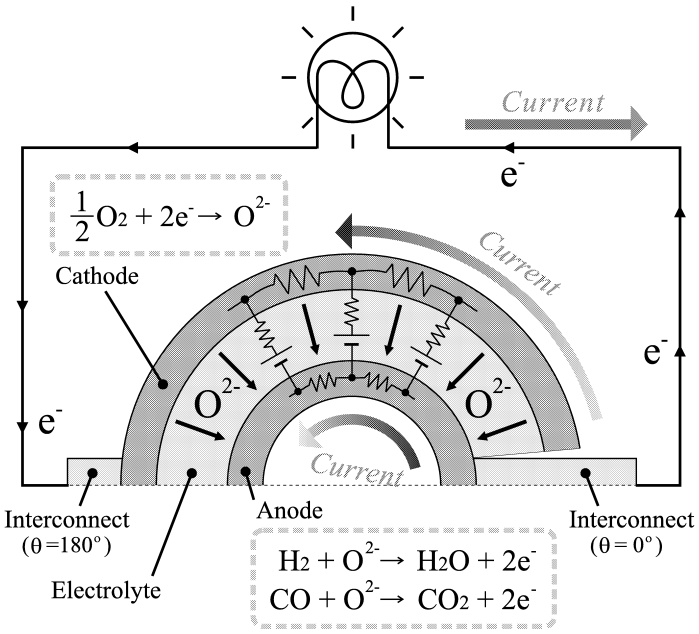


Figure 2.3: Basic concept of the electrochemical process.

Figure 2.3 illustrates the mechanism of the electrochemical process in the tubular cell. On the cathode side, oxygen molecules in the air combine with electrons to be oxide ions. The oxide ions move through the solid electrolyte to the anode side, and combine with hydrogen or carbon monoxide (CO) molecules in the fuel there. The electrons released through the anode reactions move to the cathode of the neighboring cell, and eventually return to the original location via an external circuit - i.e. electric current is generated through the tubular cells.

The amount of the electric current, which directly relates to the rates of the electrochemical reactions and the heat/mass generations involved, depends on several factors. Those factors can be roughly classified into three groups: electromotive force (EMF), internal resistance, and external load of the cell.

The EMF is largely determined by the composition of the fuel gas mixture. In general, the EMF decreases as hydrogen/CO are consumed and steam/$CO_2$ are produced. As for the internal resistance, oxide ionic resistivity of the electrolyte is one of the important factors. It tends to decrease as the temperature rises, which is said to be the main reason for the high operation temperature of the SOFCs. Electric resistivities of the electrodes are also important because the electric current flows largely in the circumferential direction in the electrodes as shown in Fig. 2.3, that is due to the geometric condition of the cell. The energy losses caused by the above resistances are called ohmic losses or ohmic overpotentials. In addition to this, activation and concentration overpotentials also arise in the electrochemical process of fuel cells, details of which can be found in a number of texts (e.g. Larminie et al. [16]).

The EMF and internal resistances vary from place to place because temperature and gas composition are non-uniform in the cell. Therefore, how the electric current flows in the cell is generally very complicated. Finally, the external load of the cell is closely related to the cell terminal voltage as well as to the amount of the electric current: the electric current becomes larger and the terminal voltage becomes lower as the external resistance decreases, and the output power of the cell reaches a peak at a certain point.

## 2.4 Summary

In this chapter, the mechanism of the IIR-T-SOFCs has been briefly explained. The key points are that the rates of both internal reforming and electrochemical reactions are mutually related to the thermal/concentration fields in the cell, and that they are essentially non-uniform in the cell. In fact, this non-uniformity is exactly one of the critical issues in the development of the high-temperature fuel cells. This is because thermal crack failures of the cell, which is composed of several different materials as shown in Fig. 2.1, can be caused by excessively high temperatures and too-large thermal gradients in the cell.

Generally speaking, there are three fundamental problems to be solved in the development of the fuel cells: how to improve the power generation performance, how to prevent thermal crack failure, and how to reduce the production cost. Among them, the thermal crack issue is an especially suitable one to be tackled with the numerical analysis because a lot of detailed data on the thermal field of the cell can be obtained. Those data are quite useful for considering the possibility of the thermal cracks, and are hard to be obtained from general experimental analysis. The thermal field in the IIR-T-SOFCs is largely determined by the balance of the following three phenomena: heat generation by the electrochemical process, heat absorption by the internal reforming process, and heat removal by the air flow. Therefore, in the numerical analysis, we have to calculate both the thermo-fluid and electric current fields as accurate as possible to obtain the reasonable data on the thermal field. For the gas flow fields, at least two-dimensional (axial and radial direction) analysis would be required to consider the heat and mass transfer appropriately. Meanwhile, the electric current should be calculated also in the circumferential direction because the current flows basically in that direction as shown in Fig. 2.3. What to assume and how to integrate those two calculations are the key points of the numerical analysis, that will be described in the next chapter.

# Chapter 3

# Numerical Modelling

This chapter presents details of the numerical model for a cell of IIR-T-SOFCs. The computational code developed and used in the present study originates in that for the Siemens-type tubular SOFCs by Li et al. [17][18]. This primary code had been extended into the code for multicomponent gas systems by Komori [19], and further development was carried out in this study to conduct the numerical analysis for the cell of IIR-T-SOFCs. In particular, the porous media flow, internal reforming and radiation models were newly adopted and the electrochemical model was greatly improved in this study. For the sake of convenience, description of the model is presented here in such an order that the gas flow fields are discussed first and then the other factors are mentioned subsequently. Additionally, an overall picture of the model is presented at the end of the chapter.

## 3.1 Calculation of Gas Flow Field

The gas flow fields, which include momentum, heat and mass transfer, are resolved in this study by using the Finite Volume Method (FVM) based on the solution algorithm suggested by Patankar [20]. Although it is not included in "gas" flow, heat conduction in "solid" is also described here because the same solution can be used to solve it.

### 3.1.1 Computational Domain and Assumptions

A longitudinal sectional view of the tubular cell is shown in Fig. 3.1 with the dimensions and chemical equations to be considered in this study. The calculation is performed with a two-dimensional cylindrical coordinate system, and the computational domain is indicated by the broken line plotted in the figure. The cell tube and feed tube are solid while the inside the feed tube is filled with a porous medium. To simplify the problem, it is assumed that an adiabatic cylindrical wall is placed outside the cell tube, so that the air flows through an annular space confined by the wall and the cell tube. It is also assumed that the cell tube end is flat, not spherical. The dimensions of the cell indicated in Fig. 3.1 are fixed in this study except for special calculation cases mentioned later.

The fuel is composed of hydrogen, steam, CO, $CO_2$ and methane, and the air is composed of oxygen and nitrogen in this study. Both the fuel and air are assumed to be incompressible and Newtonian fluids, and the gas flows are assumed to be laminar, steady and symmetric with respect to the cell axis (the Reynolds number is less than 200 in the present study). The effect of gravity is excluded.

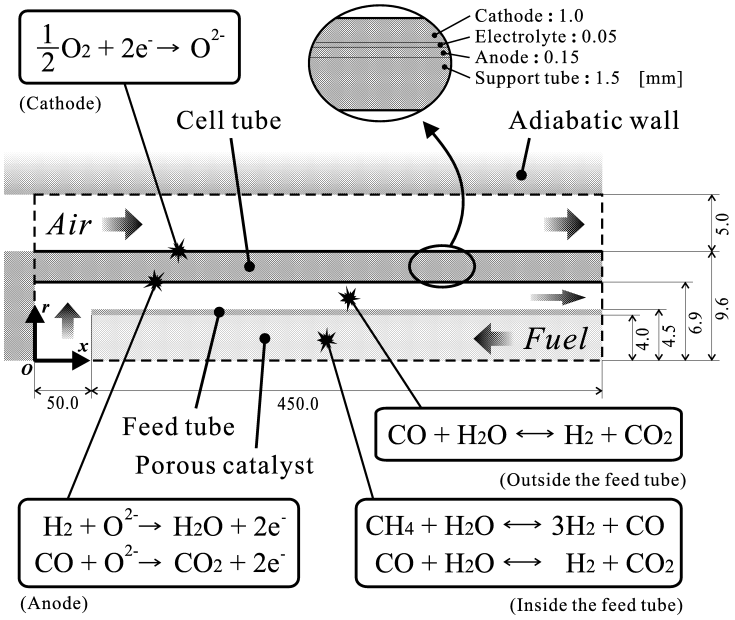


Figure 3.1: A longitudinal section of the cell and chemical reactions considered in this study.

### 3.1.2 Governing Equations

The governing equations for momentum/heat/mass transfer to be solved are different among the three kinds of areas: gas, solid and porous areas. For the gas area, those are the continuity, Navier-Stokes, energy and mass transfer equations described as follows:

≪ Continuity Equation ≫

$$\frac{\partial(\rho U_x)}{\partial x} + \frac{1}{r}\frac{\partial(r\rho U_r)}{\partial r} = 0 \tag{3-1}$$

≪ Navier-Stokes Equations ≫

$$\rho U_x \frac{\partial U_x}{\partial x} + \rho U_r \frac{\partial U_x}{\partial r} = -\frac{\partial P}{\partial x} + \frac{\partial}{\partial x}\left(\mu \frac{\partial U_x}{\partial x}\right) + \frac{1}{r}\frac{\partial}{\partial r}\left(r\mu \frac{\partial U_x}{\partial r}\right) \tag{3-2}$$

$$\rho U_x \frac{\partial U_r}{\partial x} + \rho U_r \frac{\partial U_r}{\partial r} = -\frac{\partial P}{\partial r} + \frac{\partial}{\partial x}\left(\mu \frac{\partial U_r}{\partial x}\right) + \frac{1}{r}\frac{\partial}{\partial r}\left(r\mu \frac{\partial U_r}{\partial r}\right) - \frac{\mu U_r}{r^2} \tag{3-3}$$

≪ Energy Equation ≫

$$\rho C_p U_x \frac{\partial T}{\partial x} + \rho C_p U_r \frac{\partial T}{\partial r} = \frac{\partial}{\partial x}\left(\lambda \frac{\partial T}{\partial x}\right) + \frac{1}{r}\frac{\partial}{\partial r}\left(r\lambda \frac{\partial T}{\partial r}\right) + Q \tag{3-4}$$

≪ Mass Transfer Equation ≫

$$\rho U_x \frac{\partial Y_j}{\partial x} + \rho U_r \frac{\partial Y_j}{\partial r} = \frac{\partial}{\partial x}\left(\rho D_{jm} \frac{\partial Y_j}{\partial x}\right) + \frac{1}{r}\frac{\partial}{\partial r}\left(r\rho D_{jm} \frac{\partial Y_j}{\partial r}\right) + S_j \tag{3-5}$$

In the above equations, $U_x$ and $U_r$ are the $x$- and $r$-components of the velocity, and $Y_j$ is the mass fraction of chemical species $j$. $D_{jm}$ is the mass diffusivity of species $j$ in the multicomponent gases. All of the gas properties are treated as variables dependent on local temperature and mass fraction of each chemical species, details of which will be described in Section 3.1.4.

Table 3.1: Thermal conductivity of the solids.

| | $\lambda_s$ [W/mK] |
|---|---|
| Anode (Ni-YSZ) | 6.23 |
| Cathode (LSM) | 11.0 |
| Electrolyte (YSZ) | 2.7 |
| Support tube (CSZ) | 1.1 |
| Feed tube (CSZ) | 1.1 |

Table 3.2: Parameters of the porous medium.

| | |
|---|---|
| $\epsilon$ [$-$] | 0.9 |
| $K$ [m$^2$] | $1.0 \times 10^{-7}$ |
| $f$ [$-$] | 0.088 |
| $\lambda_s$ [W/mK] | 10.0 |
| $\lambda_{\rm eff}$ [W/mK] | $\epsilon\lambda + (1-\epsilon)\lambda_s$ |
| $D_{{\rm eff}jm}$ [m$^2$/s] | $(1-\sqrt{1-\epsilon})D_{jm}$ |

$Q$ and $S_j$ in eqns (3-4) and (3-5) denote the source terms, which will also be discussed later. The effects of the internal reforming and electrochemical reactions on the thermal and concentration fields are considered through those source terms. The effect of radiative heat transfer is also included there. However, viscous dissipation in heat transfer and thermal and pressure diffusions in mass transfer are neglected in this study.

For the solid area, the governing equation to be solved is the heat conduction equation:

≪ Heat Conduction Equation (for Solid Area) ≫

$$0 = \frac{\partial}{\partial x}\left(\lambda_s \frac{\partial T}{\partial x}\right) + \frac{1}{r}\frac{\partial}{\partial r}\left(r\lambda_s \frac{\partial T}{\partial r}\right) + Q \tag{3-6}$$

where $\lambda_s$ is the thermal conductivity of the solid. The practical data of $\lambda_s$ of each material used in the present study are shown in table 3.1.

As for the porous area, the method of volume-averaging is applied to derive the governing equations because the microstructure of porous media is generally too complicated to be considered directly in the computations. In this method, the physical values are locally-averaged at a representative elementary volume (REV), which is sufficiently larger than the scale of the fine structure of the porous medium and is sufficiently smaller than the scale of the porous medium itself [21]. Consequently, the following transport equations of the averaged physical values can be derived:

≪ Continuity Equation (for Porous Area) ≫

$$\frac{\partial(\rho U_x)}{\partial x} + \frac{1}{r}\frac{\partial(r\rho U_r)}{\partial r} = 0 \tag{3-7}$$

≪ Momentum Equations (for Porous Area) ≫

$$\begin{aligned}\frac{1}{\epsilon^2}\left\{\rho U_x \frac{\partial U_x}{\partial x} + \rho U_r \frac{\partial U_x}{\partial r}\right\} &= -\frac{\partial P}{\partial x} + \frac{1}{\epsilon}\left\{\frac{\partial}{\partial x}\left(\mu\frac{\partial U_x}{\partial x}\right) + \frac{1}{r}\frac{\partial}{\partial r}\left(r\mu\frac{\partial U_x}{\partial r}\right)\right\} \\ &\quad -\frac{\mu}{K}U_x - \frac{\rho f}{\sqrt{K}}U_x\sqrt{U_x^2+U_r^2}\end{aligned} \tag{3-8}$$

$$\begin{aligned}\frac{1}{\epsilon^2}\left\{\rho U_x \frac{\partial U_r}{\partial x} + \rho U_r \frac{\partial U_r}{\partial r}\right\} &= -\frac{\partial P}{\partial r} + \frac{1}{\epsilon}\left\{\frac{\partial}{\partial x}\left(\mu\frac{\partial U_r}{\partial x}\right) + \frac{1}{r}\frac{\partial}{\partial r}\left(r\mu\frac{\partial U_r}{\partial r}\right) - \frac{\mu U_r}{r^2}\right\} \\ &\quad -\frac{\mu}{K}U_r - \frac{\rho f}{\sqrt{K}}U_r\sqrt{U_x^2+U_r^2}\end{aligned} \tag{3-9}$$

≪ Energy Equation (for Porous Area) ≫

$$\rho C_p U_x \frac{\partial T}{\partial x} + \rho C_p U_r \frac{\partial T}{\partial r} = \frac{\partial}{\partial x}\left(\lambda_{\text{eff}} \frac{\partial T}{\partial x}\right) + \frac{1}{r}\frac{\partial}{\partial r}\left(r \lambda_{\text{eff}} \frac{\partial T}{\partial r}\right) + Q \tag{3-10}$$

≪ Mass Transfer Equation (for Porous Area) ≫

$$\rho U_x \frac{\partial Y_j}{\partial x} + \rho U_r \frac{\partial Y_j}{\partial r} = \frac{\partial}{\partial x}\left(\rho D_{\text{eff}jm} \frac{\partial Y_j}{\partial x}\right) + \frac{1}{r}\frac{\partial}{\partial r}\left(r \rho D_{\text{eff}jm} \frac{\partial Y_j}{\partial r}\right) + S_j \tag{3-11}$$

where $\rho$, $\mu$, $P$, $C_p$ and $Y_j$ represent the local "intrinsic" phase average value of the gas (average over the gas volume, rather than over the total volume) while $U_x$ and $U_r$ denote the local phase average velocity of the gas. $T$ is the local average temperature of both the gas and solid (local thermal equilibrium between the two phases is assumed here). $\epsilon$ and $K$ are the porosity and permeability of the porous medium, respectively. $f$ is the inertia coefficient depending on the Reynolds number and the microstructure of the porous medium [22]. $\lambda_{\text{eff}}$ and $D_{\text{eff}jm}$ are the effective thermal conductivity and the effective mass diffusivity of species $j$, respectively. The practical data of those parameters used in the present study are shown in table 3.2. The material of the porous medium is assumed to be nickel-alumina.

### 3.1.3 Boundary Conditions

The above three pairs of governing equations are properly conjugated on the inner boundaries between the three kinds of areas: gas, solid and porous. Hence only the no-flux condition for the velocity and concentration fields is given on the gas-solid and porous-solid interfaces (except for the electrode surfaces), and no other artificial conditions are given on the inner boundaries (e.g. constant heat transfer coefficient is not given). For the electrode surfaces, mass generation or consumption caused by the electrochemical reaction is considered as a boundary condition, details of which are discussed in Section 3.4.

The outer boundary conditions are summarized in Table 3.3. As a basis of comparison between several different calculation cases, fuel mean velocity at the inlet is always set to such a value that an average current density is capped at 5000A/m$^2$ (e.g. 0.923m/s when the inlet temperature is 800°C). In contrast, air mean velocity at the inlet is basically set at 2.0m/s except for special cases. The inlet temperatures and molar fractions of the gases are different among the calculation cases, which are mentioned in Chapter 4. The closed end temperature of the cell tube is set equal to that of the air inlet.

Table 3.3: Boundary conditions for the gas flow field.

| | Velocity | Temperature | Molar fraction | Total pressure |
|---|---|---|---|---|
| Fuel inlet | Poiseuille flow | Uniform | Uniform | 110000 [Pa] |
| Air inlet | Plug flow | Uniform | Uniform | 110000 [Pa] |
| Outlets | Neumann | Neumann | Neumann | Neumann |
| Closed end | Non-slip | Uniform | No-gradient | No-gradient |
| Adiabatic wall | Non-slip | Adiabatic | No-gradient | No-gradient |
| Central axis | Axisymmetric | Axisymmetric | Axisymmetric | Axisymmetric |

### 3.1.4 Gas Properties

In the cell of IIR-T-SOFCs, the multicomponent gas properties, $\rho$, $C_p$, $\mu$, $\lambda$, and the mass diffusivity, $D_{jm}$, noticeably change depending on both the gas temperature and composition, the effects of which should be considered in the numerical model accordingly. The methods for estimating those properties are described below. Note that all the units of the physical values used in the following equations are summarized in the symbol table at the end of the thesis.

***Density***

Density of multicomponent gas mixtures, $\rho$, is calculated with the ideal gas equation:

$$\rho = \frac{P\overline{M}}{R_0 T} \tag{3-12}$$

where $R_0$ denotes the universal gas constant. $\overline{M}$ is the molar averaged molecular weight defined as follows:

$$\overline{M} = \sum_j X_j M_j \tag{3-13}$$

$X_j$ and $M_j$ represent the molar fraction and molecular weight of species $j$, respectively.

***Specific Heat at Constant Pressure***

Specific heat of multicomponent gas mixtures, $C_p$, is easily calculated by taking a mass average of the specific heat of each chemical species:

$$C_p = \sum_j Y_j C_{pj} \tag{3-14}$$

$C_{pj}$ represents the specific heat of species $j$, which can be estimated with an approximating polynomial function of temperature derived from a handbook of gas properties [23].

***Viscosity***

Viscosity of the gas mixtures, $\mu$, is estimated by the following semi-empirical formula [24] with the viscosity of each pure species:

$$\mu = \sum_j \left( \frac{X_j \mu_j}{\sum_k X_k \Phi_{jk}} \right) \tag{3-15}$$

In the above equation, $\mu_j$ denotes the viscosity of a single gas of species $j$, which can also be estimated with a polynomial function of temperature derived from the property handbook [23]. $\Phi_{jk}$ is the dimensionless interaction parameter, which is obtained by the method of Bromley and Wilke [25]:

$$\Phi_{jk} = \frac{1}{\sqrt{8}} \left( 1 + \frac{M_j}{M_k} \right)^{-\frac{1}{2}} \left[ 1 + \left( \frac{\mu_j}{\mu_k} \right)^{\frac{1}{2}} \left( \frac{M_k}{M_j} \right)^{\frac{1}{4}} \right]^2 \tag{3-16}$$

This approximation is well enough at (or below) atmospheric pressure. Under high pressure conditions, a correction term suggested by Dean and Stiel [26] is added to the above:

$$\mu = \mu_0 + 5.08 \times 10^{-8} \frac{P_{\mathrm{cr}}^{2/3} (\overline{M} \times 10^3)^{1/2}}{T_{\mathrm{cr}}^{1/6}} \left[ \exp\left(1.439 \rho_{\mathrm{re}}\right) - \exp\left(-1.11 \rho_{\mathrm{re}}^{1.858}\right) \right] \tag{3-17}$$

where $\mu_0$ represents the viscosity of the gas mixture obtained by eqns (3-15) and (3-16). $P_{\rm cr}$ and $T_{\rm cr}$ denote the molar averaged critical pressure and temperature of the gas mixture, which are given as $P_{\rm cr} = \Sigma X_j P_{{\rm cr}j}$ and $T_{\rm cr} = \Sigma X_j T_{{\rm cr}j}$ , respectively. $\rho_{\rm re}$ is the reduced density defined as $\rho_{\rm re} = \rho/\rho_{\rm cr}$, where $\rho_{\rm cr}$ is the molar averaged critical density of the gas mixture given as $\rho_{\rm cr} = \Sigma X_j \rho_{{\rm cr}j}$ .

***Thermal conductivity***

Thermal conductivity of the gas mixtures, $\lambda$, can be estimated in a similar way to viscosity: using the following semi-empirical formula [24] with the thermal conductivity of each pure species derives that of the gas mixtures:

$$\lambda \;=\; \sum_j \left( \frac{X_j \lambda_j}{\sum_k X_k \Psi_{jk}} \right) \tag{3-18}$$

Here $\lambda_j$ is the thermal conductivity of species $j$, which can also be estimated with a polynomial function of temperature derived from the property handbook [23]. $\Psi_{jk}$ is the dimensionless interaction parameter, which is obtained by the method of Lindsay and Bromley [27]:

$$\Psi_{jk} \;=\; \frac{1}{4} \left\{ 1 + \left[ \frac{\mu_j}{\mu_k} \left( \frac{M_k}{M_j} \right)^{3/4} \frac{T + \Theta_j}{T + \Theta_k} \right]^{1/2} \right\}^2 \left[ \frac{T + \Theta_{jk}}{T + \Theta_j} \right] \tag{3-19}$$

$$\Theta_j \;=\; 1.5 T_{{\rm b}j} \quad , \quad \Theta_{jk} \;=\; C \sqrt{\Theta_j \Theta_k} \tag{3-20}$$

$T_{{\rm b}j}$ denotes the boiling temperature of each pure species. $C$ is unity except when either or both components $j$ and $k$ are very polar, in which $C = 0.73$ is recommended. This approximation is well enough at (or below) atmospheric pressure. At high pressures, a correction term suggested by Stiel and Thodos [28] is added to the above:

$$\lambda \;=\; \lambda_0 \;+\; \alpha \times 10^{-8} \, \frac{P_{\rm cr}^{2/3}}{T_{\rm cr}^{1/6} (\overline{M} \times 10^3)^{1/2}} \, Z_{\rm cr}^{-5} \left[ \exp\left( \beta \rho_{\rm re} \right) + \gamma \right] \tag{3-21}$$

$$\begin{aligned}
\rho_{\rm re} \;<\; 0.5 \quad &: \quad \alpha = 2.702 \quad , \quad \beta = 0.535 \quad , \quad \gamma = -1.000 \\
0.5 \;<\; \rho_{\rm re} \;<\; 2.0 \quad &: \quad \alpha = 2.528 \quad , \quad \beta = 0.670 \quad , \quad \gamma = -1.069 \\
2.0 \;<\; \rho_{\rm re} \;<\; 2.8 \quad &: \quad \alpha = 0.574 \quad , \quad \beta = 1.155 \quad , \quad \gamma = 2.016
\end{aligned}$$

where $\lambda_0$ represents the thermal conductivity of the gas mixture obtained by eqns (3-18) to (3-20). $Z_{\rm cr}$ is the critical compressibility factor defined as $Z_{\rm cr} = P_{\rm cr} \overline{M} / \rho_{\rm cr} R_0 T_{\rm cr}$ .

***Diffusivity***

Diffusivity of species $j$ in the multicomponent gas mixture, $D_{jm}$, can be estimated using the following equation recommended by Wilke [29]:

$$D_{jm} \;=\; \frac{1 - X_j}{\sum_{k \neq j} \left( X_k / D_{jk} \right)} \tag{3-22}$$

$D_{jk}$ is the binary diffusivity of the gas mixture composed of species $j$ and $k$. Although there are several ways to predict those binary diffusivities, the Fuller-Schettler-Giddings' equation [30] is adopted in this study:

$$D_{jk} = \frac{0.01013\,T^{1.75}\left(\dfrac{1}{M_j\times 10^3}+\dfrac{1}{M_k\times 10^3}\right)^{1/2}}{P\left[(\Sigma v_j\times 10^6)^{1/3}+(\Sigma v_k\times 10^6)^{1/3}\right]^2} \tag{3-23}$$

where $\Sigma v_j$ represents the diffusion volume of the molecules of species $j$, which can be found in a chemical handbook [31].

### 3.1.5 Discretization Method

In order to solve the governing equations numerically, some sort of discretization process is indispensable. Among a variety of discretization schemes available, the Finite Volume Method (FVM) with the staggered grid system [20] is adopted in the present study. In the staggered grid system, two types of grid arrangements are provided: grids for the velocity components (velocity grids) and grids for the other scalars such as pressure, temperature and concentrations (normal grids). The velocity grids are shifted from the normal grids as illustrated in Fig. 3.2 to obtain the stable solution of the velocity and pressure fields. The discretization process on this grid system is described here.

Except for the continuity equation described by eqns (3-1) and (3-7), all the governing equations described in Section 3.1.2 can be expressed in the following general form:

≪ General Transport Equation ≫

$$\hat{\rho}U_x\frac{\partial\phi}{\partial x}+\hat{\rho}U_r\frac{\partial\phi}{\partial r} = \frac{\partial}{\partial x}\left(\Gamma\frac{\partial\phi}{\partial x}\right)+\frac{1}{r}\frac{\partial}{\partial r}\left(r\Gamma\frac{\partial\phi}{\partial r}\right)+\hat{S} \tag{3-24}$$

in which $\phi$ represents the variable of interest. $\hat{\rho}$ and $\Gamma$ are the coefficients of the convection term and the diffusion term, respectively. $\hat{S}$ denotes the source term. Details of these factors are summarized in table 3.4. Integrated over each control volume for the normal grids, painted grey in Fig. 3.2, the general transport equation (3-26) can be discretized as follows:

$$\begin{aligned}&\left\{\left(\hat{\rho}U_x\phi\right)_e-\left(\hat{\rho}U_x\phi\right)_w\right\}r_P\Delta r_P+\left\{\left(r\hat{\rho}U_r\phi\right)_n-\left(r\hat{\rho}U_r\phi\right)_s\right\}\Delta x_P \\ &= \left\{\left(\Gamma\frac{\partial\phi}{\partial x}\right)_e-\left(\Gamma\frac{\partial\phi}{\partial x}\right)_w\right\}r_P\Delta r_P+\left\{\left(r\Gamma\frac{\partial\phi}{\partial r}\right)_n-\left(r\Gamma\frac{\partial\phi}{\partial r}\right)_s\right\}\Delta x_P+\hat{S}\,r_P\Delta r_P\Delta x_P\end{aligned} \tag{3-25}$$

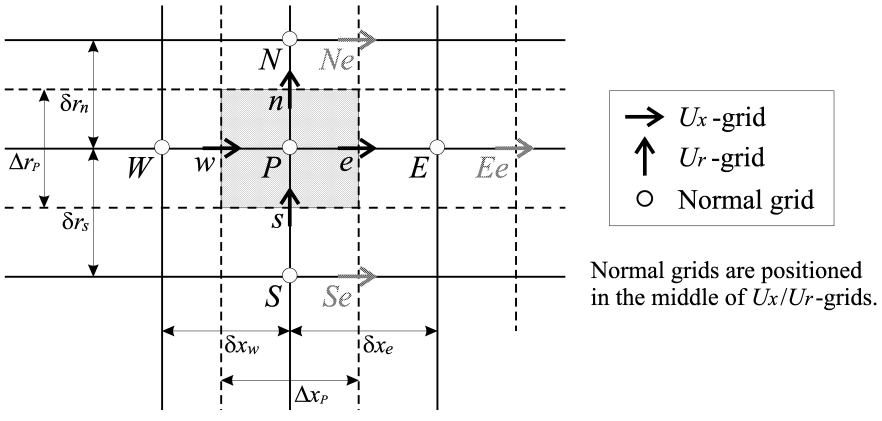


Figure 3.2: Staggered grid for the Finite Volume Method.

Table 3.4: Variables and coefficients of each governing equation.

| | $\phi$ | $\hat{\rho}$ | $\Gamma$ | $\hat{S}$ |
|---|---|---|---|---|
| Eqn (3-2) | $U_x$ | $\rho$ | $\mu$ | $-\frac{\partial P}{\partial x}$ |
| (3-3) | $U_r$ | $\rho$ | $\mu$ | $-\frac{\partial P}{\partial x} - \frac{\mu U_r}{r^2}$ |
| (3-4) | $T$ | $\rho C_p$ | $\lambda$ | $Q$ |
| (3-5) | $Y_j$ | $\rho$ | $\rho D_{jm}$ | $S_j$ |
| (3-6) | $T$ | 0 | $\lambda_s$ | $Q$ |
| (3-8) | $U_x$ | $\frac{\rho}{\epsilon^2}$ | $\frac{\mu}{\epsilon}$ | $-\frac{\partial P}{\partial x} - \frac{\mu}{K}U_x - \frac{\rho f}{\sqrt{K}}U_x\sqrt{U_x^2+U_r^2}$ |
| (3-9) | $U_r$ | $\frac{\rho}{\epsilon^2}$ | $\frac{\mu}{\epsilon}$ | $-\frac{\partial P}{\partial r} - \frac{\mu U_r}{\epsilon r^2} - \frac{\mu}{K}U_r - \frac{\rho f}{\sqrt{K}}U_r\sqrt{U_x^2+U_r^2}$ |
| (3-10) | $T$ | $\rho C_p$ | $\lambda_{\text{eff}}$ | $Q$ |
| (3-11) | $Y_j$ | $\rho$ | $\rho D_{\text{eff}jm}$ | $S_j$ |

where the subscripts $e$, $w$, $n$ and $s$ indicate the interface position of the control volume focused on, and $P$ the grid point. Note that how to take a control volume is different from the above when the velocity is considered as variable $\phi$ (due to the staggered grid system).

In order to interpolate the fluxes of convection and diffusion on the interfaces expressed by $e$, $w$, $n$ and $s$, the Power-Law scheme suggested by Patankar [20] is adopted here. As a result, the fluxes on the interfaces can be represented by the values on the grid points:

$$\left(\hat{\rho}U_x\phi - \Gamma\frac{\partial\phi}{\partial x}\right)_e r_P\Delta r_P \;=\; a_E\left(\phi_P - \phi_E\right) \tag{3-26}$$

$$\begin{aligned}
\text{Pe}_e \;<\; -10 \quad &: \quad \frac{a_E}{\mathcal{D}_e} \;=\; -\,\text{Pe}_e\, r_P\Delta r_P \\
-10 \;\le\; \text{Pe}_e \;<\; 0 \quad &: \quad \frac{a_E}{\mathcal{D}_e} \;=\; \left[(1+0.1\text{Pe}_e)^5 - \text{Pe}_e\right] r_P\Delta r_P \\
0 \;\le\; \text{Pe}_e \;\le\; 10 \quad &: \quad \frac{a_E}{\mathcal{D}_e} \;=\; (1-0.1\text{Pe}_e)^5\, r_P\Delta r_P \\
\text{Pe}_e \;>\; 10 \quad &: \quad \frac{a_E}{\mathcal{D}_e} \;=\; 0
\end{aligned}$$

Pe is the Peclet number, which indicates the ratio of the convection conductance, $\mathcal{F}$, to the diffusion conductance, $\mathcal{D}$, as follows:

$$\text{Pe}_e \;=\; \frac{\mathcal{F}_e}{\mathcal{D}_e} \quad , \quad \mathcal{F}_e \;=\; \left(\hat{\rho}U_x\right)_e \quad , \quad \mathcal{D}_e \;=\; \left(\frac{\Gamma}{\delta x}\right)_e \tag{3-27}$$

Here $\Gamma_e$ is calculated by the distance-weighted harmonic mean of $\Gamma_P$ and $\Gamma_E$, while $(\hat{\rho}U_x)_e$ is calculated by the distance-weighted arithmetic mean of $(\hat{\rho}U_x)_P$ and $(\hat{\rho}U_x)_E$ .

The interpolation process described by eqns (3-26) and (3-27) is an example for the interface $e$, and the similar process can be adopted on the other interfaces, $w$, $n$ and $s$. Consequently, eqn (3-26) can be rewritten into the following algebraic equation:

$$a_P\phi_P = a_E\phi_E + a_W\phi_W + a_N\phi_N + a_S\phi_S + b \tag{3-28}$$

where

$$a_P = a_E + a_W + a_N + a_S \tag{3-29}$$

$$b = \hat{S}\, r_P \Delta r_P \Delta x_P \tag{3-30}$$

The above discretized equations of velocity, temperature and concentration have to be solved simultaneously due to the temperature- and concentration-dependent gas properties (and also the source terms). However, the velocity field cannot be resolved unless the pressure field is revealed because the pressure gradient is included in the momentum equations. In order to solve both the velocity and pressure fields concurrently, the SIMPLE algorithm put forward by Patankar et al. [20] is adopted in this study.

### 3.1.6 Solution Algorithm

In the SIMPLE algorithm, the discretized equation for the pressure field is derived from the combination of the momentum and continuity equations, that is briefly described below.

According to the discretization process described above, the momentum equations can be discretized as follows:

$$a_e^{U_x} U_{x,e} = a_{ee}^{U_x} U_{x,ee} + a_w^{U_x} U_{x,w} + a_{Ne}^{U_x} U_{x,Ne} + a_{Se}^{U_x} U_{x,Se} + b^{U_x} + (P_P - P_E)\, r_P \Delta r_P \tag{3-31}$$

where

$$a_e^{U_x} = a_{ee}^{U_x} + a_w^{U_x} + a_{Ne}^{U_x} + a_{Se}^{U_x} \tag{3-32}$$

$$b^{U_x} = \left(\hat{S} + \frac{\partial P}{\partial x}\right) r_P \Delta r_P\, \delta x_e \tag{3-33}$$

This is an example for $U_{x,e}$, and the similar equations can be obtained for $U_{x,w}$, $U_{r,n}$ and $U_{r,s}$. Note that the pressure gradient, $-\frac{\partial P}{\partial x}$, is subtracted from $\hat{S}$ in the term $b^{U_x}$, and the last term of eqn (3-31) is added as a substitute.

The discretized equations for the velocity, however, cannot be resolved unless the correct pressure field is given. That is, an "imperfect" velocity field $U_x^*$ (and $U_r^*$ not exemplified here), which does not satisfy the continuity equation, is obtained based on a "guessed" pressure field $P^*$ by the solution of

$$a_e^{U_x} U_{x,e}^* = a_{ee}^{U_x} U_{x,ee}^* + a_w^{U_x} U_{x,w}^* + a_{Ne}^{U_x} U_{x,Ne}^* + a_{Se}^{U_x} U_{x,Se}^* + b^{U_x} + (P_P^* - P_E^*)\, r_P \Delta r_P \tag{3-34}$$

Here the velocity correction $U_x'$ and the pressure correction $P'$ are introduced as $U_x' = U_x - U_x^*$ and $P' = P - P^*$ (in which $U_x$ and $P$ represents the correct velocity and pressure, respectively). Subtracting eqn (3-34) from eqn (3-31), we can obtain the relation between $U_x'$ and $P'$ as

$$a_e^{U_x} U_{x,e}' = a_{ee}^{U_x} U_{x,ee}' + a_w^{U_x} U_{x,w}' + a_{Ne}^{U_x} U_{x,Ne}' + a_{Se}^{U_x} U_{x,Se}' + (P_P' - P_E')\, r_P \Delta r_P \tag{3-35}$$

In the above equation, the neighbor terms of $e$ can be dropped so as to obtain the following (verification of this action can be found in [20]):

$$U'_{x,e} = d_e^{U_x}\left(P'_P - P'_E\right) \tag{3-36}$$

where

$$d_e^{U_x} = \frac{r_P \Delta r_P}{a_e^{U_x}} \tag{3-37}$$

As a result, the correct velocity $U_{x,e}$ can be written as

$$U_{x,e} = U^*_{x,e} + d_e^{U_x}\left(P'_P - P'_E\right) \tag{3-38}$$

This equation shows how the correct velocity is calculated based on the imperfect velocity and the pressure correction. $U_{x,w}$, $U_{r,n}$ and $U_{r,s}$ can also be described in a similar way.

Next, the continuity equation is discretized to derive the equation for the pressure correction. Integrated over each control volume for the normal grids, the continuity equations (3-1) and (3-7) can be discretized as follows:

$$\left\{\left(\hat{\rho}U_x\right)_e - \left(\hat{\rho}U_x\right)_w\right\} r_P \Delta r_P + \left\{\left(r\hat{\rho}U_r\right)_n - \left(r\hat{\rho}U_r\right)_s\right\} \Delta x_P = 0 \tag{3-39}$$

Substituting the equations represented by eqn (3-38) for $U_{x,e}$, $U_{x,w}$, $U_{r,n}$ and $U_{r,s}$ in the above equation, we obtain, after rearrangement, the following discretized equation for $P'$:

$$a_P^{P'} P'_P = a_E^{P'} P'_E + a_W^{P'} P'_W + a_N^{P'} P'_N + a_S^{P'} P'_S + b^{P'} \tag{3-40}$$

where

$$a_E^{P'} = \hat{\rho}_e\, d_e^{U_x} r_P \Delta r_P \tag{3-41}$$

$$a_W^{P'} = \hat{\rho}_w\, d_w^{U_x} r_P \Delta r_P \tag{3-42}$$

$$a_N^{P'} = \hat{\rho}_n\, d_n^{U_r} r_n \Delta x_P \tag{3-43}$$

$$a_S^{P'} = \hat{\rho}_s\, d_s^{U_r} r_s \Delta x_P \tag{3-44}$$

$$a_P^{P'} = a_E^{P'} + a_W^{P'} + a_N^{P'} + a_S^{P'} \tag{3-45}$$

$$b^{P'} = \left\{\left(\hat{\rho}U^*_x\right)_w - \left(\hat{\rho}U^*_x\right)_e\right\} r_P \Delta r_P + \left\{\left(r\hat{\rho}U^*_r\right)_s - \left(r\hat{\rho}U^*_r\right)_n\right\} \Delta x_P \tag{3-46}$$

From the solution of the above equations, we obtain the pressure correction $P'$. Consequently, the velocity and pressure fields can be solved concurrently through the iteration process summarized as follows:

1. Give the initial (guessed) pressure field $P^*$.
2. Give the initial temperature and mass fraction fields to obtain the initial gas properties and source terms.
3. Solve a series of algebraic equations for $U_x^*$ and $U_r^*$ such as eqn (3-34).
4. Solve a series of algebraic equations for $P'$ such as eqn (3-40).
5. Calculate $P$ by adding $P'$ to $P^*$, and then consider the obtained $P$ as a new $P^*$.
6. Calculate $U_x$ and $U_r$ from $U_x^*$, $U_r^*$ and $P'$ by using the velocity-correction formulas such as eqn (3-38).
7. Solve a series of algebraic equations for temperature and mass fraction such as eqn (3-28) to calculate the gas properties and source terms again.
8. Return to step 3 (and repeat the procedure until a converged solution is obtained).

In addition to the iteration process mentioned above, each series of the algebraic equations itself also needs some sort of iterative method to be solved (because direct methods for two- or three-dimensional problems are generally very complicated). In other words, two kinds of iteration process are required: one is for calculating the coefficients of the discretized equations (as described above by the step 1 to 8), which results from the nonlinearity of the problem; the other is for solving the discretized equations, which results from the multidimensionality of the problem. In the present study, the Alternating Direction Implicit (ADI) method coupled with the Tri-Diagonal Matrix Algorithm (TDMA) [32] is adopted to solve the above discretized equations.

## 3.2 Radiation Model

From here the numerical models for the other factors of the cell, which are related to the above thermo-fluid computation through the source terms of the governing equations, are described. At the beginning, the effect of radiative heat transfer is focused on in this section.

In this study, the radiative heat transfer between the inner surface of the cell tube and the outer surface of the feed tube is considered. This plays an important role in transferring the heat generated by the electrochemical reactions from the cell tube to the feed tube. For simplicity, the two surfaces are assumed to be gray bodies with the emissivity (or the total hemispherical emittance) $e_1 = e_2 = 0.5$ , and the fuel gas mixture completely transparent.

Owing to the extremely large aspect ratio of the cell, the temperature gradient of both two surfaces is sufficiently small in the axial ($x$) direction on the basis of the distance between them. Based on this, the following assumptions are introduced in the calculation of the local radiant fluxes emitted by the two surfaces:

1. The radiative heat transfer between the two surfaces is considered only in the region of $0.05 \leq x \leq 0.5$ m, where the feed tube exists.
2. In this region, the temperatures of the two surfaces are considered to be uniform at the same temperature as their own in the intended axial position (e.g. for the local radiant fluxes emitted by a point $P_1$ on the cell tube surface and $P_2$ on the feed tube surface, in which $P_1$ and $P_2$ are at the same axial position, the cell tube temperature is considered to be uniform at $T_{P_1}$, and the feed tube temperature $T_{P_2}$).

In consequence, the following relations are obtained independently in each axial position:

$$J_{P_1} = e_1 \sigma T_{P_1}^4 + (1 - e_1)\left(J_{P_1} F_{11} + J_{P_2} F_{12}\right) \tag{3-47}$$

$$J_{P_2} = e_2 \sigma T_{P_2}^4 + (1 - e_2)\left(J_{P_1} F_{21} + J_{P_2} F_{22}\right) \tag{3-48}$$

where $J_{P_1}$ and $J_{P_2}$ are the radiosity, which means the sum of the radiant fluxes reflected and emitted from the two surfaces. The subscripts 1 and 2 indicate the cell tube side and the feed tube side, respectively. $F_{11}$, $F_{12}$, $F_{21}$ and $F_{22}$ are the configuration factors, and the values for infinite co-axial tubes are employed here. $\sigma$ is the Stefan-Boltzmann constant. Calculating the radiosity $J_{P_1}$ and $J_{P_2}$ by the above equations, we can obtain the net radiant fluxes emitted by the two points as

$$q_{\mathrm{rad}P_1} = J_{P_1} - \left(J_{P_1} F_{11} + J_{P_2} F_{12}\right) \tag{3-49}$$

$$q_{\mathrm{rad}P_2} = J_{P_2} - \left(J_{P_1} F_{21} + J_{P_2} F_{22}\right) \tag{3-50}$$

The above equations are given also independently in each axial position, and these radiant fluxes are included in the thermo-fluid computation as a part of the source term.

## 3.3 Internal Reforming Model

Next the effects of the internal reforming reactions are described. As shown in Fig. 3.1, the steam reforming reaction described by eqn (2-1) and the water-gas shift reaction described by eqn (2-2) are considered inside the feed tube. The shift reaction is considered also outside the feed tube. The reaction rates of the two reactions, $R_{\rm steam}$ and $R_{\rm shift}$, are locally calculated as follows:

$$R_{\rm steam} = 1.75 \times 10^6 \left(\frac{P_{\rm CH_4}}{101325}\right)^{1.2} W_{\rm cat} \exp\left(\frac{-57840}{R_0 T}\right) \tag{3-51}$$

$$R_{\rm shift} = k^+_{\rm shift} P_{\rm CO} P_{\rm H_2O} - k^-_{\rm shift} P_{\rm H_2} P_{\rm CO_2} \tag{3-52}$$

Eqn (3-51) is based on an empirical formula suggested by Odegard et al. [10]. $W_{\rm cat}$ is the mass density of the catalyst for the steam reforming, which differs among the calculation cases as mentioned in Chapter 4. Eqn (3-52) is also based on an empirical formula suggested by Lehnert et al. [33]. $k^+_{\rm shift}$ and $k^-_{\rm shift}$ denote the velocity constants of forward and backward water-gas shift reactions, respectively. These constants are so large that the shift reaction is always close to the equilibrium. In this study $k^-_{\rm shift} = 9.74 \times 10^{-7}$ is given and $k^+_{\rm shift}$ is calculated based on

$$K_{\rm shift} = \frac{k^+_{\rm shift}}{k^-_{\rm shift}} \tag{3-53}$$

where $K_{\rm shift}$ is the equilibrium constant of the shift reaction calculated based on the Gibbs free energy change, which is locally estimated with a polynomial function of temperature derived from a property handbook [34].

Based on the above reaction rates, the thermodynamic heat generations by the reforming reactions are calculated as

$$Q_{\rm steam} = -\Delta H_{\rm steam} R_{\rm steam} \tag{3-54}$$

$$Q_{\rm shift} = -\Delta H_{\rm shift} R_{\rm shift} \tag{3-55}$$

$\Delta H_{\rm steam}$ and $\Delta H_{\rm shift}$ are the enthalpy changes for each reaction, locally estimated with a polynomial function of temperature derived from the handbook [34]. The mass generations of each chemical species by each reaction, $S_{{\rm steam}j}$ and $S_{{\rm shift}j}$, are also calculated as shown in table 3.5.

Table 3.5: Mass generation rates of each species by the reforming reactions.

| | $H_2$ | $H_2O$ | CO | $CO_2$ | $CH_4$ |
|---|---|---|---|---|---|
| $S_{{\rm steam}j}$ | $3R_{\rm steam}M_{\rm H_2}$ | $-R_{\rm steam}M_{\rm H_2O}$ | $R_{\rm steam}M_{\rm CO}$ | 0 | $-R_{\rm steam}M_{\rm CH_4}$ |
| $S_{{\rm shift}j}$ | $R_{\rm shift}M_{\rm H_2}$ | $-R_{\rm shift}M_{\rm H_2O}$ | $-R_{\rm shift}M_{\rm CO}$ | $R_{\rm shift}M_{\rm CO_2}$ | 0 |

Here $M_j$ is the molecular weight of species $j$. These heat and mass generations are also included in the thermo-fluid computation as a part of the source terms.

## 3.4 Electrochemical Model

The last and probably the most important factor in the source terms of the thermo-fluid computation is the heat and mass generation associated with the electrochemical process. The way of calculating the heat/mass generation is described over the next two sections.

As mentioned in the preceding section and shown in Fig. 3.1, the electro-chemical reactions of hydrogen and CO, described by eqns (2-6) and (2-7), are considered in the present study. The electromotive forces, $E$, generated by these reactions are calculated locally (that is, in each axial position) based on the Nernst equation as follows:

$$E_{\mathrm{hyd\cdot oxy}} = E^0_{\mathrm{hyd\cdot oxy}} - \frac{R_0 T}{2F} \ln \left[ \frac{P_{\mathrm{H_2O}}}{P_{\mathrm{H_2}} \left( P_{\mathrm{O_2}} / 101325 \right)^{0.5}} \right] \tag{3-56}$$

$$E_{\mathrm{co\cdot oxy}} = E^0_{\mathrm{co\cdot oxy}} - \frac{R_0 T}{2F} \ln \left[ \frac{P_{\mathrm{CO_2}}}{P_{\mathrm{CO}} \left( P_{\mathrm{O_2}} / 101325 \right)^{0.5}} \right] \tag{3-57}$$

where

$$E^0_{\mathrm{hyd\cdot oxy}} = -\frac{\Delta G^0_{\mathrm{hyd\cdot oxy}}}{2F} \tag{3-58}$$

$$E^0_{\mathrm{co\cdot oxy}} = -\frac{\Delta G^0_{\mathrm{co\cdot oxy}}}{2F} \tag{3-59}$$

The subscripts "hyd $\cdot$ oxy" and "co $\cdot$ oxy" indicate the electrochemical reactions of eqns (2-6) and (2-7), respectively. $\Delta G^0_{\mathrm{hyd\cdot oxy}}$ and $\Delta G^0_{\mathrm{co\cdot oxy}}$ are the standard Gibbs free energy changes for each reaction, which are locally estimated with a polynomial function of temperature derived from the property handbook [34]. $F$ denotes the Faraday constant. Note that the local partial pressures on the two electrode surfaces are assigned to the above equations, which means that the concentration overpotentials in the fuel and air paths are implicitly included in the decrease in the electromotive force. For reference, the electromotive force $E_{\mathrm{hyd\cdot oxy}}$ and $E_{\mathrm{co\cdot oxy}}$ obtained under specific conditions are plotted in Fig. 3.3(a) and (b).

The electrochemical reactions expressed by eqns (2-6) and (2-7) can be divided into the electrode reactions, expressed by eqns (2-3), (2-4) and (2-5). It is necessary for the proper modelling to consider the activation overpotential, $\eta$, accompanied with each electrode reaction, which directly affects the consumption ratio between hydrogen and CO. In this study, those overpotentials are calculated with the empirical equations suggested by Achenbach [35] as

$$\eta_{\mathrm{hyd}} = i_{\mathrm{hyd\cdot oxy}} \left[ \frac{2F}{R_0 T} k_{\mathrm{hyd}} \left( \frac{P_{\mathrm{H_2}}}{P_{\mathrm{fuel}}} \right)^{0.25} \exp \left( -\frac{A_{\mathrm{a}}}{R_0 T} \right) \right]^{-1} \tag{3-60}$$

$$\eta_{\mathrm{co}} = i_{\mathrm{co\cdot oxy}} \left[ \frac{2F}{R_0 T} k_{\mathrm{co}} \left( \frac{P_{\mathrm{CO}}}{P_{\mathrm{fuel}}} \right)^{0.25} \exp \left( -\frac{A_{\mathrm{a}}}{R_0 T} \right) \right]^{-1} \tag{3-61}$$

$$\eta_{\mathrm{oxy}} = \left( i_{\mathrm{hyd\cdot oxy}} + i_{\mathrm{co\cdot oxy}} \right) \left[ \frac{4F}{R_0 T} k_{\mathrm{oxy}} \left( \frac{P_{\mathrm{O_2}}}{P_{\mathrm{air}}} \right)^{0.25} \exp \left( -\frac{A_{\mathrm{c}}}{R_0 T} \right) \right]^{-1} \tag{3-62}$$

where $i_{\mathrm{hyd\cdot oxy}}$ and $i_{\mathrm{co\cdot oxy}}$ are the current densities in the electrolyte arising from the reactions of eqns (2-6) and (2-7), respectively. Note that the electric current is assumed to flow only radially in the electrolyte, details of which will be described in Section 3.5. The coefficients $k_{\mathrm{hyd}}$, $k_{\mathrm{co}}$ and $k_{\mathrm{oxy}}$ are given as $k_{\mathrm{hyd}} = 2.13 \times 10^8$, $k_{\mathrm{co}} = 2.98 \times 10^8$ and $k_{\mathrm{oxy}} = 1.49 \times 10^{10}$ A/m$^2$.

$A_a$ and $A_c$ are the activation energy: $A_a = 1.1 \times 10^5$ and $A_c = 1.6 \times 10^5$ J/mol. For reference, $\eta_{hyd}$, $\eta_{co}$ and $\eta_{oxy}$ obtained under specific conditions are plotted in Fig. 3.3(c)

Ohmic resistivities of the electrolyte and electrodes of the cell are also calculated in each axial position. In the present study, empirical formulas suggested by Bessette [36] are adopted to consider the temperature dependency of them:

$$R_e = 2.94 \times 10^{-5} \exp\left(\frac{10350}{T}\right) \tag{3-63}$$

$$R_a = 2.98 \times 10^{-5} \exp\left(\frac{-1392}{T}\right) \tag{3-64}$$

$$R_c = 8.11 \times 10^{-5} \exp\left(\frac{600}{T}\right) \tag{3-65}$$

in which $R_e$ is the oxide ionic resistivity of the electrolyte. $R_a$ and $R_c$ are the electric resistivities of the anode and cathode, respectively. The resistivities obtained from the above equations are plotted in Fig. 3.3(d).

Here the following relations exist between the electromotive force, activation overpotential, ohmic resistivity of the electrolyte, current density in the electrolyte, and the electric potentials of the anode and cathode, $V_a$ and $V_c$ :

$$E_{hyd\cdot oxy} - (\eta_{hyd} + \eta_{oxy}) - i R_e h_e = V_c - V_a \tag{3-66}$$

$$E_{co\cdot oxy} - (\eta_{co} + \eta_{oxy}) - i R_e h_e = V_c - V_a \tag{3-67}$$

where

$$i = i_{hyd\cdot oxy} + i_{co\cdot oxy} \tag{3-68}$$

$h_e$ is the thickness of the electrolyte. From the above relations, the local current density can be obtained if the local potential difference $V_c - V_a$ is given, and vice versa. In this study, the cell terminal voltage is given as a boundary condition and both the current density and potential fields in the cell are calculated based on an equivalent electrical circuit model. $R_a$ and $R_c$ are included in that circuit model, details of which will be discussed in the next section.

Based on the local current densities obtained from the above electrochemical models, the thermodynamic heat generations by the electrochemical reactions are calculated as follows:

$$q_{hyd\cdot oxy} = \left(-\frac{\Delta H_{hyd\cdot oxy}}{2F} - \tilde{E}\right) i_{hyd\cdot oxy} \tag{3-69}$$

$$q_{co\cdot oxy} = \left(-\frac{\Delta H_{co\cdot oxy}}{2F} - \tilde{E}\right) i_{co\cdot oxy} \tag{3-70}$$

where

$$\tilde{E} = E_{hyd\cdot oxy} - (\eta_{hyd} + \eta_{oxy}) = E_{co\cdot oxy} - (\eta_{co} + \eta_{oxy}) \tag{3-71}$$

The mass generations of each chemical species by each reaction, $s_{hyd\cdot oxy j}$ and $s_{co\cdot oxy j}$, are also calculated as shown in table 3.6. Note that these heat and mass generations have non-uniform distributions in the circumferential direction because the current densities are non-uniform in that direction (as discussed in the next section). Hence these heat and mass generations are averaged in that direction to be included in the two-dimensional thermo-fluid computation.

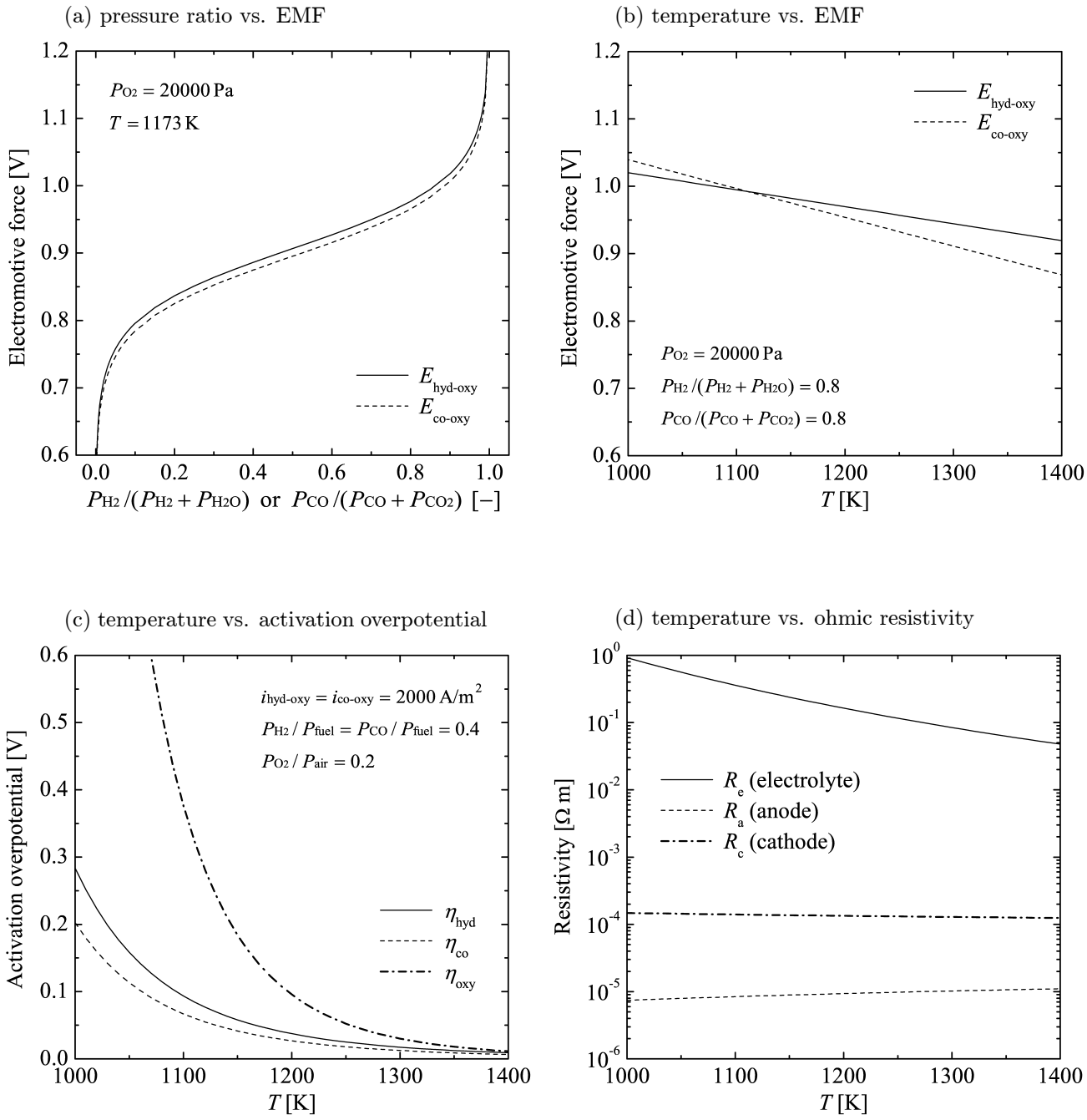


Figure 3.3: Characteristics of EMF, activation overpotential and ohmic resistivity.

Table 3.6: Mass generation rates of each species by the electrochemical reactions.

| | $H_2$ | $H_2O$ | CO | $CO_2$ | $O_2$ |
|---|---|---|---|---|---|
| $s_{\mathrm{hyd\cdot oxy}j}$ | $-\frac{i_{\mathrm{hyd\cdot oxy}}}{2F}M_{\mathrm{H_2}}$ | $\frac{i_{\mathrm{hyd\cdot oxy}}}{2F}M_{\mathrm{H_2O}}$ | 0 | 0 | $-\frac{i_{\mathrm{hyd\cdot oxy}}}{4F}M_{\mathrm{O_2}}$ |
| $s_{\mathrm{co\cdot oxy}j}$ | 0 | 0 | $-\frac{i_{\mathrm{co\cdot oxy}}}{2F}M_{\mathrm{CO}}$ | $\frac{i_{\mathrm{co\cdot oxy}}}{2F}M_{\mathrm{CO_2}}$ | $-\frac{i_{\mathrm{co\cdot oxy}}}{4F}M_{\mathrm{O_2}}$ |

The heat generations described by eqns (3-69) and (3-70) are considered as a source term of the energy equation in the electrolyte layer of the cell tube. However, The mass generations shown in table 3.6 cannot be directly treated as source terms of the mass transfer equations because they affects not only the concentration field but also the velocity field. In other words, the effects of the mass generations by the electrochemical reactions should be treated as inner boundary conditions for the velocity and concentration fields:

$$U_{r,\mathrm{a}} = -\frac{n_{\mathrm{a\,H_2}} + n_{\mathrm{a\,H_2O}} + n_{\mathrm{a\,CO}} + n_{\mathrm{a\,CO_2}}}{\rho} \tag{3-72}$$

$$U_{r,\mathrm{c}} = \frac{n_{\mathrm{c\,O_2}}}{\rho} \tag{3-73}$$

$$n_{\mathrm{a}j} = s_{\mathrm{hyd\cdot oxy}j} + s_{\mathrm{co\cdot oxy}j} = -\rho Y_j U_{r,\mathrm{a}} + \rho D_{jm}\frac{\partial Y_j}{\partial r} \tag{3-74}$$

$$n_{\mathrm{c}j} = s_{\mathrm{hyd\cdot oxy}j} + s_{\mathrm{co\cdot oxy}j} = \rho Y_j U_{r,\mathrm{c}} - \rho D_{jm}\frac{\partial Y_j}{\partial r} \tag{3-75}$$

where $U_{r,\mathrm{a}}$ and $U_{r,\mathrm{c}}$ are the velocities of the gas mixtures on the anode and cathode surfaces, and $n_{\mathrm{a}j}$ and $n_{cj}$ represent the mass fluxes of species $j$ from the anode and cathode surfaces to the gas areas, respectively.

## 3.5 Calculation of Equivalent Electrical Circuit

Here the solution of both the electric current and potential fields of the cell is described. In the present study, it is assumed that the electric current flows only in the circumferential ($\theta$) direction in the electrodes and only radially in the electrolyte. This is based on the two facts: one is that the aspect ratio of the cell is extremely large, and the other is that the ohmic resistivities of the electrodes are basically much smaller than that of the electrolyte as shown in eqns (3-63) to (3-65). This assumption permits the electric current and potential fields to be resolved on a fairly simple equivalent electrical circuit shown in Fig. 2.3. In addition, influences of the interconnects are excluded in this study, so that the potential difference between the anode at $\theta = 0^\circ$ and the cathode at $\theta = 180^\circ$ is referred to as the cell terminal voltage.

Figure 3.4 illustrates the grid system for the equivalent electrical circuit in the cell tube. According to the Kirchhoff's law, the following discretized equations can be derived for both the anode and cathode layers:

$$(i_u - i_d)\, h_{\mathrm{a}} - i_{PP'} \cdot r_{\mathrm{e}} \Delta\theta_P = 0 \tag{3-76}$$

$$(i_{u'} - i_{d'})\, h_{\mathrm{c}} + i_{PP'} \cdot r_{\mathrm{e}} \Delta\theta_P = 0 \tag{3-77}$$

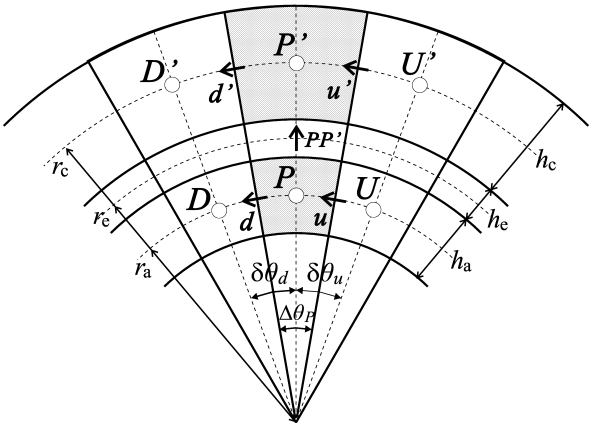


Figure 3.4: Grid for the equivalent electrical circuit.

where $i_u$, $i_d$, $i_{u'}$ and $i_{d'}$ are the current densities in the anode or cathode on the interfaces $u$, $d$, $u'$ and $d'$ of the control volume focused on, respectively. $i_{PP'}$ is the current density in the electrolyte between the intended grid points $P$ and $P'$, which corresponds to $i$ defined by eqn (3-68) in the previous section. $h_\mathrm{a}$ and $h_\mathrm{c}$ represent the thicknesses of the anode and cathode, and $r_\mathrm{e}$ is the distance from the cell axis to the middle of the electrolyte layer.

According to the Ohm's law, the current densities in the anode and cathode can be represented by the electric potentials on the grid points as

$$i_u = \frac{V_U - V_P}{R_\mathrm{a} r_\mathrm{a} \delta\theta_u} \tag{3-78}$$

$$i_d = \frac{V_P - V_D}{R_\mathrm{a} r_\mathrm{a} \delta\theta_d} \tag{3-79}$$

$$i_{u'} = \frac{V_{U'} - V_{P'}}{R_\mathrm{c} r_\mathrm{c} \delta\theta_u} \tag{3-80}$$

$$i_{d'} = \frac{V_{P'} - V_{D'}}{R_\mathrm{c} r_\mathrm{c} \delta\theta_d} \tag{3-81}$$

Meanwhile, the current density in the electrolyte can be represented by the local potential difference and $\tilde{E}$ defined by eqn (3-71) as

$$i_{PP'} = \frac{\tilde{E}_{PP'} - (V_{P'} - V_P)}{R_\mathrm{e} h_\mathrm{e}} \tag{3-82}$$

This corresponds to eqns (3-66) and (3-67) in the previous section. Using eqns (3-78) to (3-82), we can rewrite eqns (3-76) and (3-77) into the following algebraic equations:

$$a_P^V V_P = a_U^V V_U + a_D^V V_D + a_{PP'}^V V_{P'} - b \tag{3-83}$$

$$a_{P'}^V V_{P'} = a_{U'}^V V_{U'} + a_{D'}^V V_{D'} + a_{PP'}^V V_P + b \tag{3-84}$$

where

$$a_U^V = \frac{h_\mathrm{a}}{R_\mathrm{a} r_\mathrm{a} \delta\theta_u} \tag{3-85}$$

$$a_D^V = \frac{h_\mathrm{a}}{R_\mathrm{a} r_\mathrm{a} \delta\theta_d} \tag{3-86}$$

$$a^V_{U'} = \frac{h_c}{R_c r_c \delta\theta_u} \tag{3-87}$$

$$a^V_{D'} = \frac{h_c}{R_c r_c \delta\theta_d} \tag{3-88}$$

$$a^V_{PP'} = \frac{r_e \Delta\theta_P}{R_e h_e} \tag{3-89}$$

$$a^V_P = a^V_U + a^V_D + a^V_{PP'} \tag{3-90}$$

$$a^V_{P'} = a^V_{U'} + a^V_{D'} + a^V_{PP'} \tag{3-91}$$

$$b^V = \frac{r_e \Delta\theta_P}{R_e h_e} \tilde{E}_{PP'} \tag{3-92}$$

These equations can be solved by using TDMA with the cell terminal voltage given as a boundary condition. Consequently, the current density and electric potential fields are obtained, and the ohmic heat generations in the anode, cathode and electrolyte are calculated as

$$Q_{\mathrm{ohm}P} = \frac{i^2_u \delta\theta_u + i^2_d \delta\theta_d}{\delta\theta_u + \delta\theta_d} R_a \tag{3-93}$$

$$Q_{\mathrm{ohm}P'} = \frac{i^2_{u'} \delta\theta_u + i^2_{d'} \delta\theta_d}{\delta\theta_u + \delta\theta_d} R_c \tag{3-94}$$

$$Q_{\mathrm{ohm}PP'} = i^2_{PP'} R_e \tag{3-95}$$

These heat generations are non-uniform in the $\theta$-direction, so that they are averaged in that direction to be included in the 2-D thermo-fluid computation as a part of the source term.

## 3.6 Definitions for the Cell Performance Analysis

The purpose of the electrical computation describe above is to calculate not only the heat and mass generation rates but also the power generation performance of the cell. Hence the definition of terms relating to the cell performance is described in this section.

***Average Current Density***

Average current density of the cell, $i_{\mathrm{av}}$, is calculated based on the local current densities in the electrolyte and the area of the electrolyte layer as

$$i_{\mathrm{av}} = \frac{\sum_{x=0}^{L} \sum_{\theta=0}^{\pi} i_{PP'} \Delta\theta_P \Delta x_P}{\pi L} = \frac{I_{\mathrm{cell}}}{2\pi r_e L} \tag{3-96}$$

where $L$ is the length of the cell tube, 0.5m in the present study, and $I_{\mathrm{cell}}$ means the total electric current of the cell.

***Terminal Voltage***

The cell terminal voltage, $V_{\mathrm{cell}}$, means the potential difference between the anode at $\theta = 0°$ and the cathode at $\theta = 180°$ in this study:

$$V_{\mathrm{cell}} = V_{\mathrm{c}\,(\theta=180°)} - V_{\mathrm{a}\,(\theta=0°)} \tag{3-97}$$

***Average Electromotive Force***

Although two types of electromotive force, $E_{\mathrm{hyd\cdot oxy}}$ and $E_{\mathrm{co\cdot oxy}}$, are individually calculated as described in Section 3.4, there is little difference between the two because the shift reaction is very close to the equilibrium everywhere in the cell, that will be shown in Chapter 4. Here, for convenience of the performance analysis, cell-averaged electromotive force, $E_{\mathrm{av}}$, is defined as

$$E_{\mathrm{av}} = \frac{\sum_{x=0}^{L} E_{\mathrm{max},P}\Delta x_P}{L} \tag{3-98}$$

$$E_{\mathrm{hyd\cdot oxy},P} \geq E_{\mathrm{co\cdot oxy},P} : \quad E_{\mathrm{max},P} = E_{\mathrm{hyd\cdot oxy},P}$$
$$E_{\mathrm{hyd\cdot oxy},P} < E_{\mathrm{co\cdot oxy},P} : \quad E_{\mathrm{max},P} = E_{\mathrm{co\cdot oxy},P}$$

***Average Activation Overpotential***

For the same reason as the electromotive force, cell-averaged activation overpotential, $\eta_{\mathrm{av}}$, is defined as follows:

$$\eta_{\mathrm{av}} = \frac{\sum_{x=0}^{L}\sum_{\theta=0}^{\pi} \eta_{\mathrm{max},PP'}\Delta\theta_P\Delta x_P}{\pi L} \tag{3-99}$$

$$\eta_{\,\mathrm{hyd},PP'} \geq \eta_{\mathrm{co},PP'} : \quad \eta_{\mathrm{max},PP'} = \eta_{\,\mathrm{hyd},PP'} + \eta_{\mathrm{oxy},PP'}$$
$$\eta_{\,\mathrm{hyd},PP'} < \eta_{\mathrm{co},PP'} : \quad \eta_{\mathrm{max},PP'} = \eta_{\mathrm{co},PP'} + \eta_{\mathrm{oxy},PP'}$$

where $E_{\mathrm{av}}$ and $\eta_{\mathrm{av}}$ satisfy

$$E_{\mathrm{av}} - \eta_{\mathrm{av}} = \tilde{E}_{\mathrm{av}} = \frac{\sum_{x=0}^{L}\sum_{j=0}^{\pi} \tilde{E}_{PP'}\Delta\theta_P\Delta x_P}{\pi L} \tag{3-100}$$

***Average Ohmic Loss***

Cell-averaged ohmic loss in the electrolyte layer, $\zeta_{\mathrm{e\,av}}$, is calculated as

$$\zeta_{\mathrm{e\,av}} = \frac{\sum_{x=0}^{L}\sum_{\theta=0}^{\pi} (iR_{\mathrm{e}}h_{\mathrm{e}})_{PP'}\,\Delta\theta_P\Delta x_P}{\pi L} \tag{3-101}$$

while cell-averaged ohmic loss in the anode and cathode, $\zeta_{\mathrm{a\,av}}$ and $\zeta_{\mathrm{c\,av}}$, are defined as

$$\zeta_{\mathrm{a\,av}} = V_{\mathrm{a}\,(\theta=0^\circ)} - \frac{\sum_{x=0}^{L}\sum_{\theta=0}^{\pi} V_P\Delta\theta_P\Delta x_P}{\pi L} \tag{3-102}$$

$$\zeta_{\mathrm{c\,av}} = \frac{\sum_{x=0}^{L}\sum_{\theta=0}^{\pi} V_{P'}\Delta\theta_P\Delta x_P}{\pi L} - V_{\mathrm{c}\,(\theta=180^\circ)} \tag{3-103}$$

where $\zeta_{\mathrm{e\,av}}$, $\zeta_{\mathrm{a\,av}}$ and $\zeta_{\mathrm{c\,av}}$ satisfy the following relation:

$$\zeta_{\mathrm{e\,av}} + \zeta_{\mathrm{a\,av}} + \zeta_{\mathrm{c\,av}} = \tilde{E}_{\mathrm{av}} - V_{\mathrm{cell}} \tag{3-104}$$

***Output Power***

Output power of the cell, $\mathcal{P}$, is calculated based on the cell terminal voltage and the total electric current as follows:

$$\mathcal{P} = V_{\mathrm{cell}}I_{\mathrm{cell}} \tag{3-105}$$

***Fuel Utilization Factor***

Fuel Utilization Factor, $\mathcal{U}_{\text{fuel}}$, is calculated based on the molar flow rates of hydrogen, CO and methane at the inlet and outlet of the cell:

$$\mathcal{U}_{\text{fuel}} = \left[1 - \frac{(N_{\text{H}_2} + N_{\text{CO}} + 4N_{\text{CH}_4})_{\text{outlet}}}{(N_{\text{H}_2} + N_{\text{CO}} + 4N_{\text{CH}_4})_{\text{inlet}}}\right] \times 100 \tag{3-106}$$

where $N_j$ represent the molar flow rate of species $j$ through a cross section of the flow path, and the subscripts "inlet" and "outlet" indicate the inlet of the feed tube and outlet of the cell tube, respectively. Note that the value of $N_{\text{H}_2} + N_{\text{CO}} + 4N_{\text{CH}_4}$ is not changed by the steam reforming and shift reactions as shown by eqn (2-1) and (2-2). This means that $N_{\text{H}_2} + N_{\text{CO}} + 4N_{\text{CH}_4}$ is constant inside the feed tube, and that $\mathcal{U}_{\text{fuel}}$ can be calculated also based on the total electric current as

$$\mathcal{U}_{\text{fuel}} = \frac{I_{\text{cell}}}{2F\,(N_{\text{H}_2} + N_{\text{CO}} + 4N_{\text{CH}_4})_{\text{inlet}}} \times 100 \tag{3-107}$$

In this regard, however, the fuel mean velocity at the inlet of the feed tube is always set to such a value that the average current density is capped at $5000\text{A/m}^2$ as mentioned in Section 3.1.3. Therefore, in the present study, $\mathcal{U}_{\text{fuel}}$ can be obtained also as

$$\mathcal{U}_{\text{fuel}} = \frac{i_{\text{av}}}{5000} \times 100 \tag{3-108}$$

***Air Utilization Factor***

Air utilization factor, $\mathcal{U}_{\text{air}}$, is calculated in a similar way to the fuel utilization factor:

$$\mathcal{U}_{\text{air}} = \left(1 - \frac{N_{\text{O}_2\text{ outlet}}}{N_{\text{O}_2\text{ inlet}}}\right) \times 100 \tag{3-109}$$

where the subscripts "inlet" and "outlet" indicate the inlet and outlet of the air path, respectively, and $\mathcal{U}_{\text{air}}$ is calculated also based on the total electric current as

$$\mathcal{U}_{\text{air}} = \frac{I_{\text{cell}}}{4FN_{\text{O}_2\text{ inlet}}} \times 100 \tag{3-110}$$

***Energy Conversion Efficiency***

Energy conversion efficiency of the cell, $\mathcal{E}$, is defined as

$$\mathcal{E} = \frac{\mathcal{P}}{H_{\text{H}_2}\Delta N_{\text{H}_2} + H_{\text{CO}}\Delta N_{\text{CO}} + H_{\text{CH}_4}\Delta N_{\text{CH}_4}} \times 100 \tag{3-111}$$

where $H_j$ is the lower heating value (LHV) of species $j$, and $\Delta N_j$ is the change in the molar flow rate of species $j$ between the outlet of the feed tube and the outlet of the cell tube. Hence $\mathcal{E}$ means the efficiency of the electrochemical process itself, and $N_{j\text{ inlet}}$ should be used instead of $\Delta N_j$ in the above equation if the thermal efficiency of the entire cell is required.

***Reforming Rate***

Reforming rate of methane, $\mathcal{R}$, (not the reforming "reaction" rate $R_{\text{steam}}$ or $R_{\text{shift}}$) is defined as follows. The subscript "feedout" indicates the outlet of the feed tube.

$$\mathcal{R} = \left(1 - \frac{N_{\text{CH}_4\text{ feedout}}}{N_{\text{CH}_4\text{ inlet}}}\right) \times 100 \tag{3-112}$$

## 3.7 Summary

In closing of this chapter, an overall picture of the model is presented in Fig. 3.5. One of the main parts of this numerical model is the multicomponent thermo-fluid computation conducted with a two-dimensional cylindrical coordinate system. Based on the obtained temperature and concentration fields, the electromotive force and resistivities are locally calculated to be involved in the quasi-three-dimensional computation of the electric potential/current fields, which is the other main part of this model. From the results for the electric current fields, the heat and mass generations associated with the electrochemical process are calculated to be averaged in the circumferential direction of the cell, and be fed back to the thermo-fluid computation. In addition to this, the multicomponent gas properties, reforming reaction rate and radiant flux are also interrelated with the thermo-fluid fields. Therefore, all of the above calculations are iterated simultaneously to obtain the whole results including the data on the power generation performance of the cell, such as the average current density, output power and efficiency.

Finally, the validity of this numerical analytical model is referred to. The validity of the results from the present IIR-T-SOFC model is admittedly not supported by experimental data or the like because the IIR-T-SOFCs focused on in this study is currently just an idea. In this model, however, each fundamental factor involved in the cell is properly treated on a theoretical or an experimental basis, and those individual factors are combined in a rational way. This should be enough to support the "utility" of the model as a tool for predicting the operating state of the cell on the planning stage.

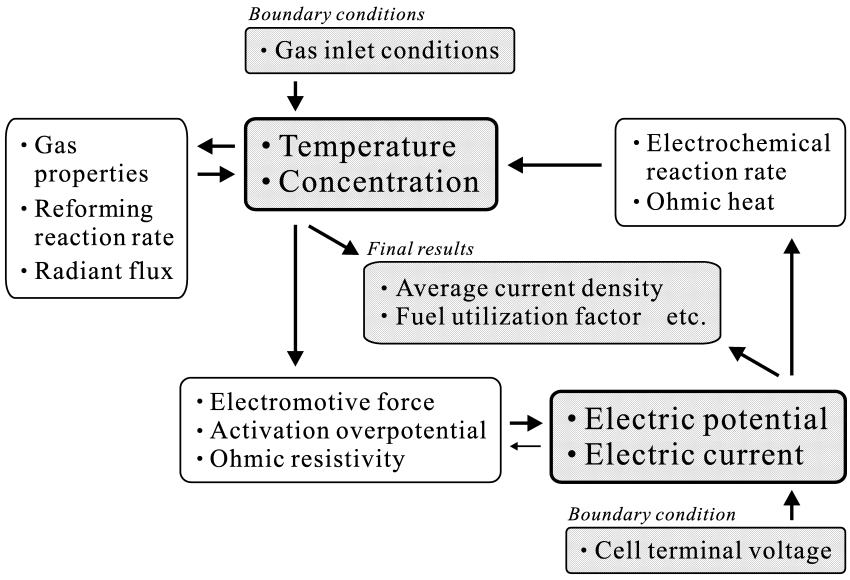


Figure 3.5: Overall picture of the IIR-T-SOFC model.

# Chapter 4

# Numerical Analysis

This chapter presents the calculation results and discussion on the operating state of the cell of IIR-T-SOFCs obtained by using the numerical model described in the preceding chapter. The results include details of the thermal/concentration fields, electric potential/current fields and power generation characteristics of the cell. The effects of several controllable factors on the cell thermal field, such as gas inlet temperature, air flow rate and distribution of the reforming catalyst, are also numerically investigated.

## 4.1 Computational Parameters

Computational parameters for all the calculation cases examined in this study are summarized in Tables 4.1 to 4.4. Among them, the "Base case" is for studying the fundamental characteristics of the operating state of the cell, which will be discussed in Section 4.2. In addition, the Base case serves as a standard for comparison with the other 10 cases, in which several parameters expected to influence the characteristics of the cell are changed.

Table 4.1: Computational parameters for all the calculated cases.

| Case | Temperature (fuel/air inlets) [°C] | Mean velocity (fuel inlet) [m/s] | Mean velocity (air inlet) [m/s] | Gas composition | Catalyst distribution | Electrode thickness |
|---|---|---|---|---|---|---|
| Base | 800 | 0.923 | 2.0 | Normal | Normal | Normal |
| T-750 | 750 | 0.880 | 2.0 | Normal | Normal | Normal |
| T-850 | 850 | 0.966 | 2.0 | Normal | Normal | Normal |
| AF-10 | 800 | 0.923 | 1.0 | Normal | Normal | Normal |
| AF-40 | 800 | 0.923 | 4.0 | Normal | Normal | Normal |
| SM-11 | 800 | 0.692 | 2.0 | SM-11 | Normal | Normal |
| SM-41 | 800 | 1.385 | 2.0 | SM-41 | Normal | Normal |
| CD-1 | 800 | 0.923 | 2.0 | Normal | CD-1 | Normal |
| CD-2 | 800 | 0.923 | 2.0 | Normal | CD-2 | Normal |
| E-0075 | 800 | 0.923 | 2.0 | Normal | Normal | E-0075 |
| E-0300 | 800 | 0.923 | 2.0 | Normal | Normal | E-0300 |

Table 4.2: Gas composition at the inlets of fuel and air ($X_j$ : molar fraction).

| | $X_{H_2}$ [−] (fuel inlet) | $X_{H_2O}$ [−] (fuel inlet) | $X_{CO}$ [−] (fuel inlet) | $X_{CO_2}$ [−] (fuel inlet) | $X_{CH_4}$ [−] (fuel inlet) | $X_{O_2}$ [−] (air inlet) | $X_{N_2}$ [−] (air inlet) |
|---|---|---|---|---|---|---|---|
| Normal | 0.200 | 0.500 | 0.020 | 0.030 | 0.250 | 0.209 | 0.791 |
| SM-11 | 0.2667 | 0.3333 | 0.0267 | 0.040 | 0.3333 | 0.209 | 0.791 |
| SM-41 | 0.1333 | 0.6667 | 0.0133 | 0.020 | 0.1667 | 0.209 | 0.791 |

Table 4.3: Reforming catalyst distribution.

| | $W_{cat}(x)$ [g/cm$^3$] $(0.05 \leq x \leq 0.5)$ |
|---|---|
| Normal | 2.0 |
| CD-1 | 0.2 |
| CD-2 | $0.4 \times \dfrac{0.5 - x}{0.45}$ |

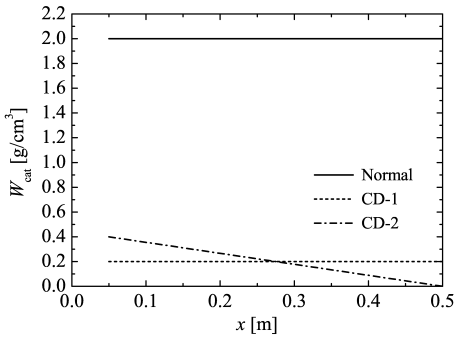


Figure 4.1: Catalyst distribution.

Table 4.4: Thickness of the electrodes, electrolyte and support tube.

| | Cathode [mm] | Electrolyte [mm] | Anode [mm] | Support tube [mm] |
|---|---|---|---|---|
| Normal | 1.0 | 0.050 | 0.150 | 1.500 |
| E-0075 | 1.0 | 0.050 | 0.075 | 1.575 |
| E-0300 | 1.0 | 0.050 | 0.300 | 1.350 |

In Case T-750 and T-850, the inlet temperature of both fuel and air is changed. The gas inlet temperature is one of the main factors governing the operating temperature and eventually the power generation performance of the cell, that will be discussed in Section 4.3. Case AF-10 and AF-40 are for examining the effects of air flow rate on the thermal field of the cell. The air flow rate also greatly affects the cell thermal field as will be described in Section 4.4.

Composition of the fuel gas mixture pumped into the cell may also be a key factor because it directly affects both the electrochemical and internal reforming reaction rates. Table 4.2 shows the gas composition conditions for Case SM-11, SM-41 and the other cases, details of which will be described in Section 4.5. Note that the fuel mean velocity at the inlet is always set in such a way that the upper limit of the average current density is 5000A/m$^2$, thus the fuel velocity in Case T-750, T-850, SM-11 and SM-41 is different from that in the Base case.

The reaction rate of the steam reforming is directly affected also by the mass density of the catalyst, $W_{cat}$, as expressed by eqn (3-51). Hence the thermal field of the cell could be successfully controlled by adjusting the amount and distribution of the reforming catalyst inside the feed tube. Table 4.3 and Fig. 4.1 show the catalyst distributions for Case CD-1, CD-2 and the other cases. The results will be discussed in Section 4.6.

Finally, the effects of the electrode thickness (practically, the anode and support tube thickness) will be investigated based on the results for Case E-0075 and E-0300. Table 4.4 presents the thickness of each layer composing the cell tube. Note that the total thickness of the anode and support tube is set constant in every case so that the area of the electrolyte layer and the dimension of the cell tube itself are not changed depending on those cases. The details will be described in Section 4.7.

In addition to the conditions summarized in Table 4.1 to 4.4, the cell terminal voltages of various levels are given in each case as a boundary condition for the electric current/potential fields in order to change the average current density of the cell. This means that a variety of external loads are implicitly given to change the output power of the cell. In the following sections, the results in which the average current density is about $4000\mathrm{A/m^2}$, and accordingly the fuel utilization factor is about 80% as is clear from eqn (3-108), will be particularly focused on. This is a standard operating condition of SOFCs developed and tested today.

## 4.2 Fundamental Characteristics of the Cell

This section discusses the fundamental characteristics of the operating state of the cell based on the calculation results for the Base case. In the Base case, the inlet temperature of fuel and air is set at 800°C as shown in Table 4.1. The air mean velocity at the inlet is 2.0m/s, which supplies sufficient amount of oxygen for the cathode reaction so that the cell performance should not be substantially reduced by the shortage of oxygen. The reforming catalyst is uniformly included in the porous medium embedded inside the feed tube, and its mass density is set at $2.0\,\mathrm{g/cm^3}$ for the methane fuel to be almost completely reformed even when the average current density $i_{\mathrm{av}}$ is 0 $\mathrm{A/m^2}$ (which means that the electrical circuit is open).

Table 4.5 shows the cell performance results for the Base case under five representative operating conditions. In this section, these five conditions will be focused on first to discuss the essential effect of the average current density. Then the case of $i_{\mathrm{av}} = 3926$ will be taken up in order to study a standard thermal/concentration and electric potential/current fields of the cell in detail. Finally, the power generation characteristics of the cell will be described.

Table 4.5: Cell performance results for the Base case.

| Case | | Base case | | | | |
|---|---|---|---|---|---|---|
| Average current density, $\mathsf{i}_{\mathrm{av}}$ | $[\mathrm{A/m^2}]$ | 0 | 980 | 1958 | 2942 | 3926 |
| Terminal voltage, $\mathsf{V}_{\mathrm{cell}}$ | [V] | – | 0.755 | 0.665 | 0.608 | 0.55 |
| Output power, $\mathcal{P}$ | [W] | 0 | 19.9 | 35.1 | 48.2 | 58.2 |
| Energy conversion efficiency, $\mathcal{E}$ | [%] | – | 55.7 | 49.7 | 45.8 | 41.6 |
| Fuel utilization factor, $\mathcal{U}_{\mathrm{fuel}}$ | [%] | 0 | 19.6 | 39.2 | 58.8 | 78.5 |
| Air utilization factor, $\mathcal{U}_{\mathrm{air}}$ | [%] | 0 | 3.5 | 7.0 | 10.5 | 14.0 |
| Reforming rate, $\mathcal{R}$ | [%] | 98.5 | 99.7 | 100.0 | 100.0 | 100.0 |
| Maximum temperature of the electrolyte | [°C] | 800.0 | 832.6 | 894.6 | 967.3 | 1047.0 |
| Average temperature of the electrolyte | [°C] | 752.7 | 798.2 | 850.0 | 901.2 | 957.6 |

### 4.2.1 Thermal and Concentration Fields

First of all, the velocity vectors of the gas mixtures in and around the cell tube for the cases of $i_{\mathrm{av}} = 0$ and 3926 are shown in Fig. 4.2 (a) and (b), respectively. Note that these figures are not in scale: the radial ($r$) direction is described ten times longer than the axial ($x$) direction. From this figure, it can be seen that the overall gas flow characteristics for the two cases are quite similar. That is, the fuel gas mixture accelerates inside the feed tube due to an increase in the number of the total moles caused by the steam reforming. Then the flow changes its direction mainly near the outlet of the feed tube, so that some of the fuel stagnates at the bottom of the cell tube. The reason why the air accelerates only in the case of $i_{\mathrm{av}} = 3926$ is simply that it expands as its temperature rises.

The thermal field of the cell, however, considerably changes depending on the average current density of the cell. Figure 4.3 shows the cell temperature contours obtained under the conditions of five different average current densities. Note that the darker tone corresponds to the higher temperatures. In the case of $i_{\mathrm{av}} = 0$, which has been exceptionally calculated by giving $i = 0$ to every grid point rather than solving the equivalent electrical circuit, the cell temperature decreases below 700°C near the fuel inlet. This is because of the endothermic effect of the steam reforming. When the electric current flows in the cell, the temperature increases due to the thermodynamic and ohmic heats generated by the electrochemical process. As the average current density becomes larger, the overall cell temperature becomes higher and the temperature gradients also become larger. This can be confirmed also in Fig. 4.4 which presents the local temperature of the electrolyte layer and the feed tube.

The above thing is an essential effect of the average current density on the temperature field of the cell. Although the cases for the average current densities of about 4000A/m$^2$ will

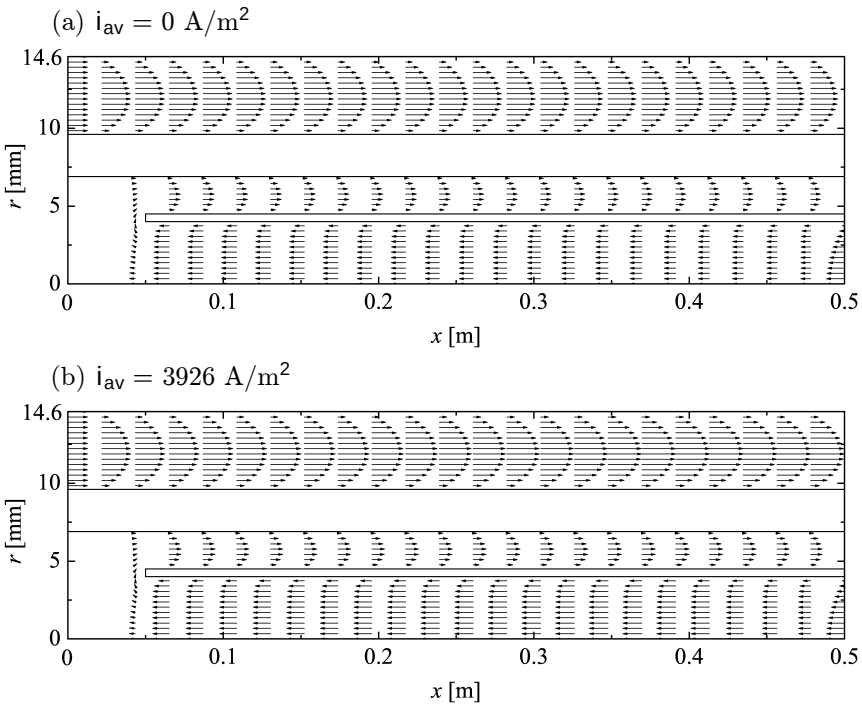


Figure 4.2: Velocity vector plots for the Base case.

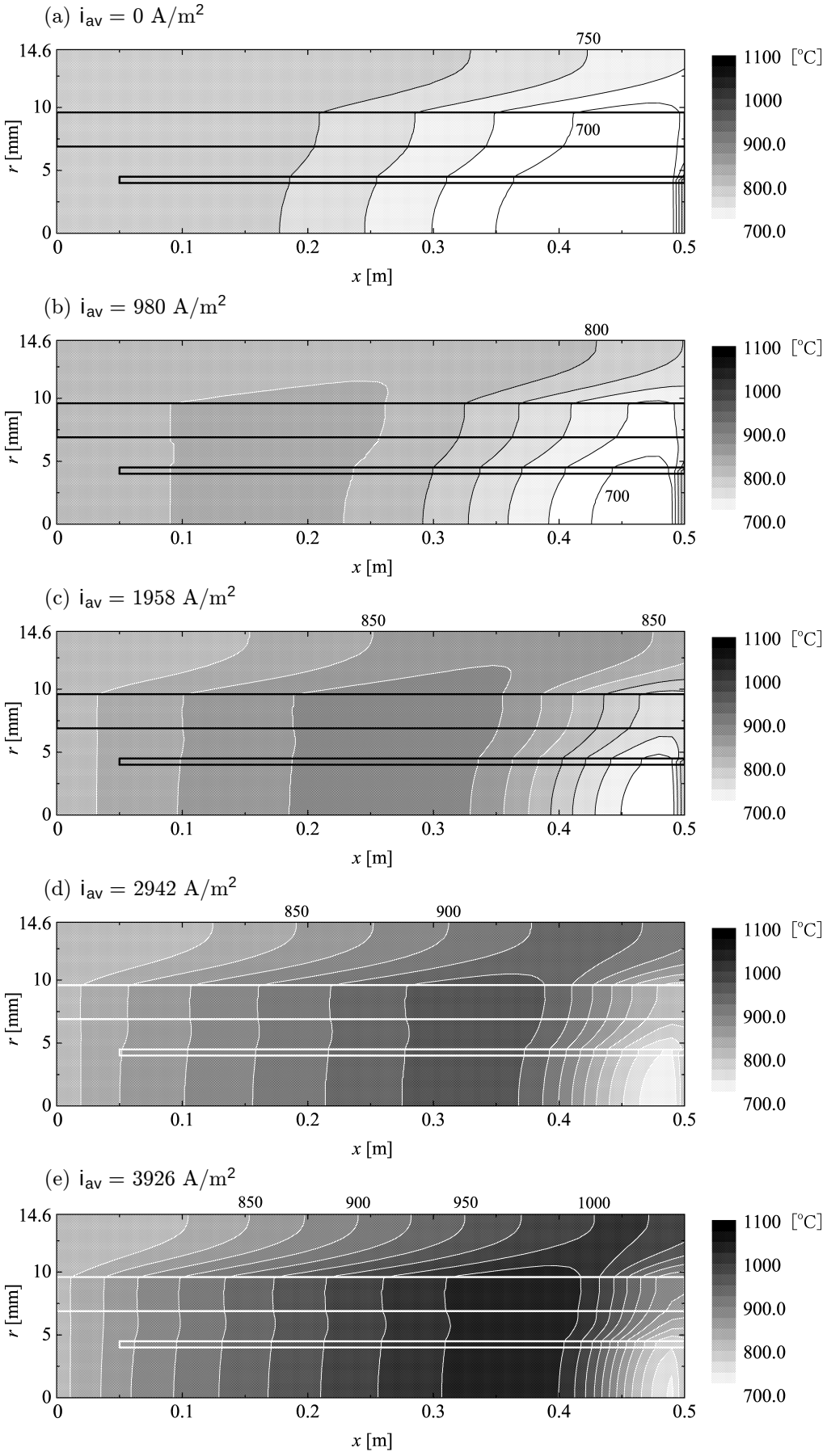


Figure 4.3: Temperature contours for the Base case.

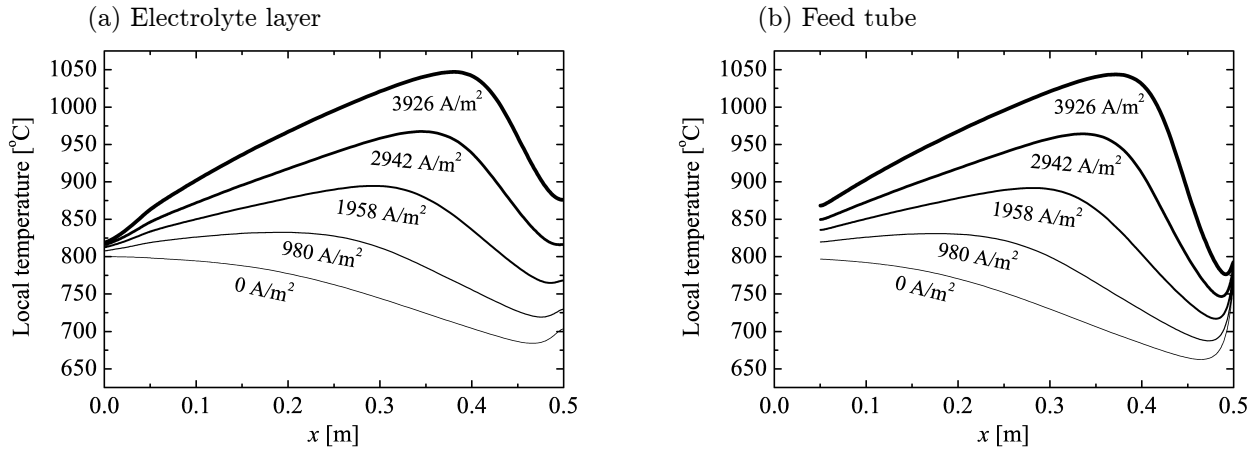


Figure 4.4: Temperature gradients for the Base case.

be extensively described in the later sections, this effect is common to all the calculation cases shown in Table 4.1. In general, such a high temperature and large temperature gradients as shown in Fig. 4.3 (e) should be avoided because they can cause thermal crack failures of the cell (actually 1050°C is said to be an upper limit for the cell tube temperature). Hence it is quite useful for the actual development/operation of fuel cells to predict the cell thermal field in detail as presented above. Furthermore, it is very meaningful to examine how to reduce both the maximum temperature and temperature gradient of the cell tube with keeping the cell output level as high as possible. This is the topic we focus in the later sections.

As clearly shown in Fig. 4.3, the cell thermal field is greatly affected by the internal reforming and electrochemical reactions (and also the air flow rate as will be discussed in Section 4.4). Therefore, the concentration field in the cell is focused on next in order to figure out the characteristics of those chemical changes. Figure 4.5 shows the molar fraction contours of each chemical species for the case of $i_{\mathrm{av}} = 3926$. Note that the color tone level differs among each chemical species. From this figure, it can be seen that most of the methane is reformed (with the production of hydrogen/CO and the consumption of steam) near the inlet of the feed tube. This is because the amount of the catalyst embedded there, which is optimized for the open-circuit state as mentioned before, is excessive for the operating cell. That is, the operating cell needs less catalyst for the reforming than the open-circuit cell owing to the higher temperatures. Figure 4.6 shows the molar flow rate of each chemical species for the case of $i_{\mathrm{av}} = 0$ and 3926. Comparing (a) with (c), we can see a big difference in the progress of the steam reforming between the open-circuit cell and the operating cell. The slight changes in the amounts of $CO_2$ inside the feed tube indicate the effect of the water-gas shift reaction.

Meanwhile, outside of the feed tube, hydrogen and CO are consumed while steam and $CO_2$ are produced as shown in Fig. 4.5 (a) to (d) and also Fig. 4.6 (d). These chemical changes are derived from both the electrochemical and water-gas shift reactions. In the case of $i_{\mathrm{av}} = 0$, only the effect of the shift reaction can be recognized with the slight changes outside the feed tube as shown in Fig. 4.6 (b). The reason for the considerable changes at the bottom of the cell tube shown in Fig. 4.5 (a) to (d) is that the fuel flow stagnates while the electrochemical reactions take place there. As for the air side, oxygen is consumed by the cathode reaction as seen in Fig. 4.5 (f). Compared to the fuel side, it can be seen that the ratio of the concentration gradient

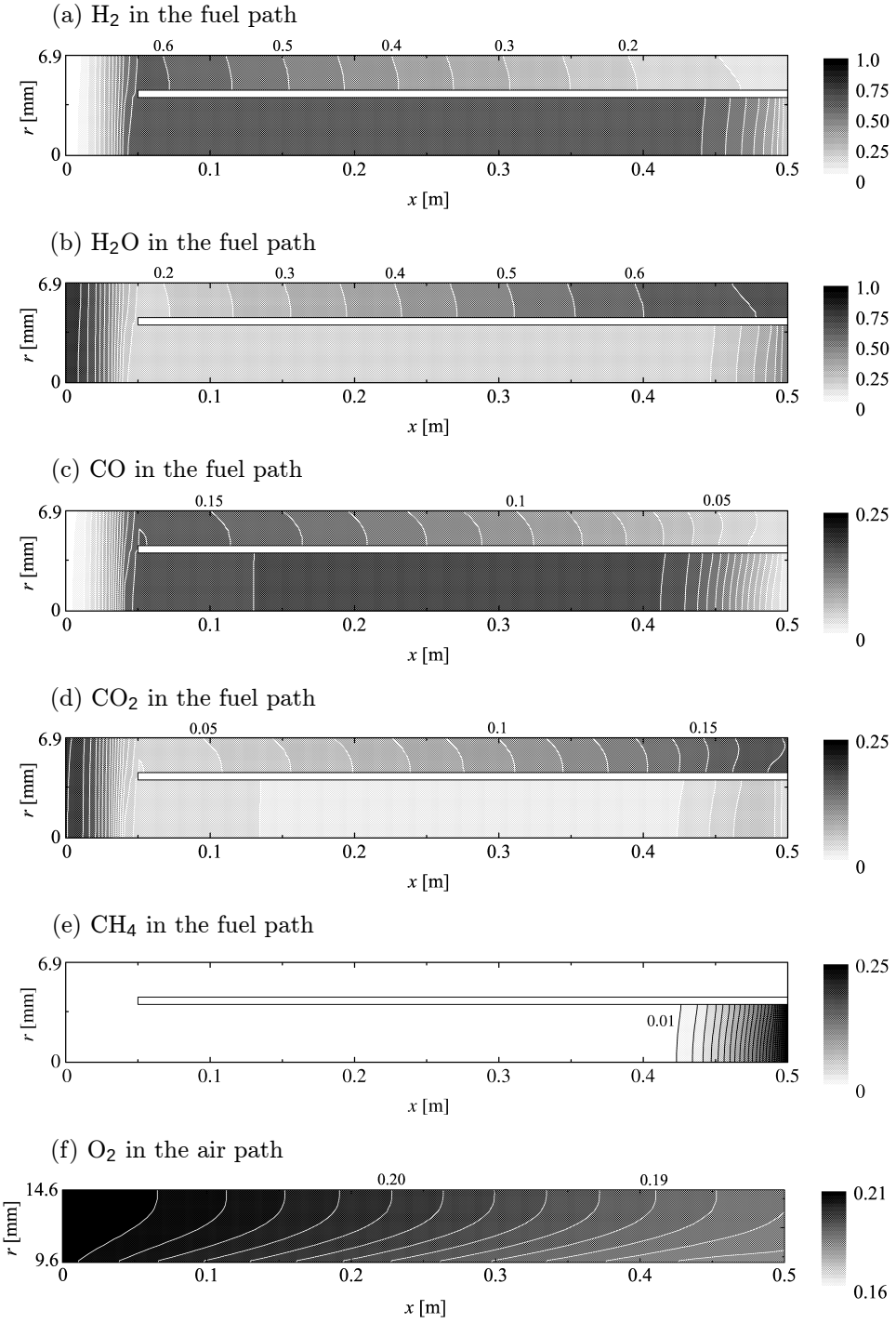


Figure 4.5: Molar fraction contours of each chemical species for the Base case ($i_{\mathrm{av}} = 3926$ A/m$^2$).

in the $x$-direction to that in the $x$-direction is considerably larger in the air side. This is due to the large velocity and small diffusivity of the air gas mixture. However, the magnitude of the concentration gradient is not so large because an enough amount of air for the electrochemical reactions is supplied.

In contrast to the steam reforming reaction, it is rather difficult to give an intuitive explanation on where the electrochemical reactions actively proceed. This is because the elec-

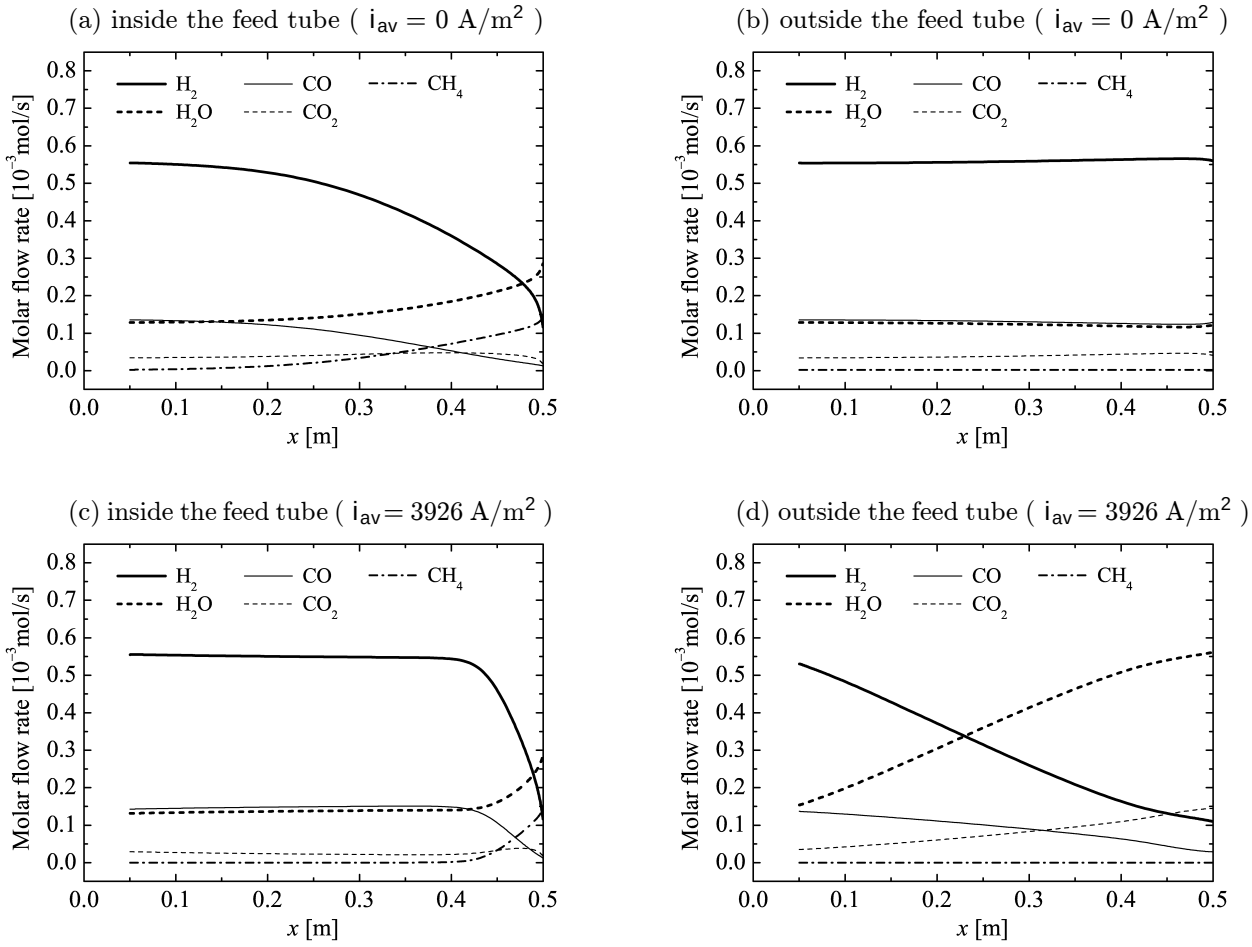


Figure 4.6: Molar flow late of each chemical species for the Base case.

trochemical reactions are strongly related to the electrical conditions of the cell. For a more comprehensive understanding of the characteristics of the electrochemical process and also the thermal field of the cell, the calculation results on the electric potential/current fields will be described next.

### 4.2.2 Electric Potential and Current Fields ($\theta$-averaged)

Figure 4.7 shows the current density distribution in the electrolyte layer for the Base case with the operating condition of $i_{\rm av} = 3926$. Note that the data plotted in this figure have been averaged in the $\theta$-direction. The original results including the $\theta$-way information will be presented in Section 4.7. From this figure, it can be observed that the distribution of the local electric current arising from the two electrochemical reactions, shown by eqns (2-6) and (2-7), are quite similar all over the cell despite the different consumption rate of hydrogen and CO (and also the production rate of steam and $CO_2$) shown in Fig. 4.6 (d). This means that the water-gas shift reaction proceeds in such a direction that hydrogen/$CO_2$ are consumed and CO/steam are produced outside the feed tube. It is also seen from Fig. 4.7 that the electrochemical reactions proceeds actively in the middle of the cell rather than near the inlet and outlet of the cell. To clarify the reason of this, the distributions of electromotive force (EMF), activation overpotential and ohmic loss are presented next.

Figure 4.8 shows the EMF distributions for the same case. From this figure, it can be seen that the EMF generated by the two electrochemical reactions are also quite similar all over the cell due to the effect of the shift reaction. It is also seen that the EMF has a clear peak near the outlet of the feed tube because the molar fractions of hydrogen and CO also have peaks there as shown in Fig. 4.5. The EMF basically becomes lower toward both the end and outlet of the cell tube as hydrogen/CO are consumed and steam/$CO_2$ are produced by the electrochemical reactions. However, it becomes a little higher near the outlet of the cell tube owing to the lower temperatures stemming from the steam reforming.

Judging from the EMF distribution, it seems that the current density should also have a peak near the outlet of the feed tube, but it does not. The primary reason of this is in the strong temperature dependency of the activation overpotential. Figure 4.9 shows the activation overpotential distributions for the same case. Note that the data plotted in this figure also have been averaged in the $\theta$-direction. In this figure, it can be seen that the activation overpotentials accompanied with the anode reactions of hydrogen and CO, expressed by eqns (2-3) and (2-4), are also quite similar all over the cell. In addition, it can be observed that the activation

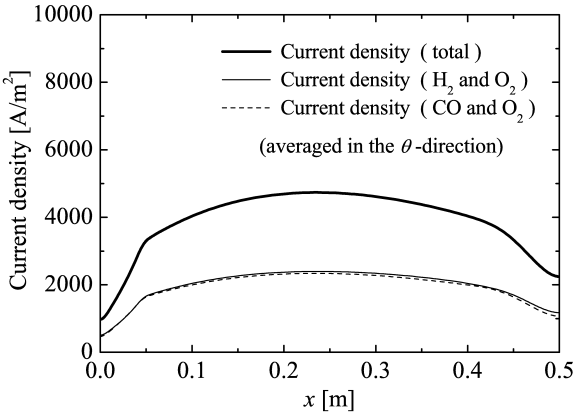


Figure 4.7: Current density distribution in the electrolyte (Base case, $i_{\mathrm{av}}$= 3926 A/m$^2$).

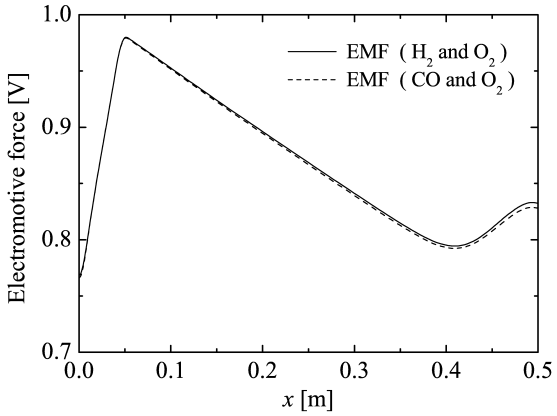


Figure 4.8: EMF distribution for the Base case ($i_{\mathrm{av}}$ = 3926 A/m$^2$).

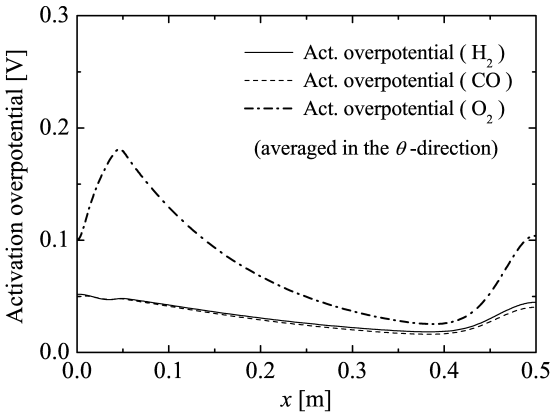


Figure 4.9: Activation overpotential distribution for the Base case ($i_{\mathrm{av}}$ = 3926 A/m$^2$).

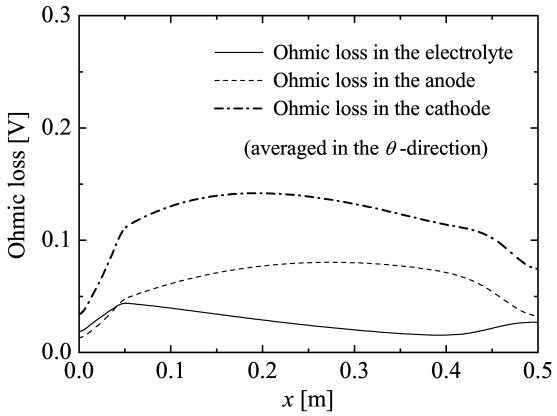


Figure 4.10: Ohmic loss distribution for the Base case ($i_{\mathrm{av}}$ = 3926 A/m$^2$).

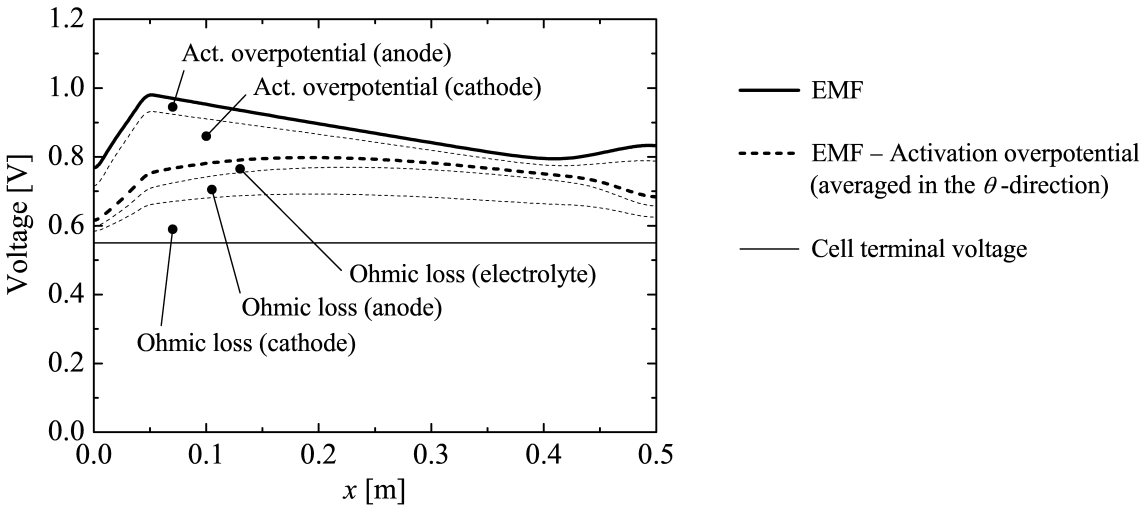


Figure 4.11: Distribution pattern of all the factors causing the voltage drop of the cell (Base case, $i_{\mathrm{av}} = 3926$ A/m$^2$).

overpotentials (especially for the air side) are significantly reduced around $x = 0.3$ to 0.4, where the peak of the cell temperature exists as shown in Fig. 4.4. This is the main reason why the larger current densities are generated in the middle of the cell despite the lower EMF compared to near the outlet of the feed tube. To put it another way, the current density distribution depends on the cell thermal field as well as, or more than, on the concentration field of each chemical species. At the same time, however, it is also true that the cell temperature becomes higher where the larger current is generated. Therefore, the key point is that a kind of enhancing interaction exists between rise in temperature and increase in electric current density, which generally encourages the non-uniformity of the cell thermal field.

In addition to the activation overpotentials, the ohmic losses in the anode, cathode and electrolyte layers should also be described here for a more precise understanding. Figure 4.10 shows the $\theta$-averaged ohmic loss distributions for the three layers. Note that the losses in the anode and cathode layers are generated by the $\theta$-way current flows while the loss in the electrolyte layer is by the $r$-way current flow. From this figure, it can be seen that the ohmic loss in the two electrodes are larger than that in the electrolyte. This is because the circumferential lengths of the electrodes are much larger than the thickness of the electrolyte. The difference in the ohmic loss for the two electrodes arises from that in the ohmic resistivity and also in the thickness of them, which are closely related to the $\theta$-way distribution of the current density as will be discussed in Section 4.7. The important thing at this point is that the ($x$-way) distribution features of the ohmic losses in the anode and cathode are similar to that of the current density shown in Fig. 4.7. This is because the ohmic resistivities of the two electrodes are not so changed depending on temperature. On the other hand, the feature of the ohmic loss distribution in the electrolyte is similar to that of the activation overpotential because its ohmic resistivity noticeably becomes smaller as the temperature rises. Hence it can be said that the temperature dependency of the resistivity of the electrolyte also contributes to the enhancing interaction described above, though the effect of this is less than that of the activation overpotential.

As a summary of the above, all the distributions of the losses/overpotentials causing the voltage drop of the cell are collectively shown in Fig. 4.11 with the EMF distribution and the cell terminal voltage. In this figure, the range between the lines indicates the magnitude of each loss/overpotential. From this figure, we can see clearly how the proportion of each loss/overpotential spatially varies in the cell, which governs the current density distribution and eventually the cell thermal field of the cell as mentioned above. By the way, if the data plotted in Fig. 4.11 are averaged not only in the $\theta$-direction but also in the $x$-direction, several cell-averaged values for the cell performance analysis, defined in Section 3.6, are obtained.

### 4.2.3 Power Generation Characteristics

As a final topic on the fundamental results for the Base case, the power generation characteristics of the cell are examined. The results for more than ten different operating conditions including the five shown in Table 4.5 are presented here. Figure 4.12 shows the pattern of changes in the cell-averaged EMF, activation overpotential, ohmic loss and the cell terminal voltage against the cell-averaged current density. Note that this figure shows what is called "I-V curves" of the cell under the constant gas inlet conditions (as shown in Table 3.3 and 4.1), rather than under constant operating temperature nor constant fuel utilization factor. From this figure, it can be seen that the strong temperature dependency of both the activation overpotential and ohmic loss in the electrolyte greatly affects not only the temperature distribution patterns mentioned before but also the power generation characteristics of the cell. That is, the activation overpotential and the ohmic loss in the electrolyte do not increase proportionally to the average current density due to rise in the cell operating temperature, and accordingly the cell terminal voltage does not decrease proportionally to the average current density. In addition to this, it can be seen from Fig. 4.12 that the ohmic loss in the two electrodes becomes a principal factor causing the voltage drop as the average current density becomes larger.

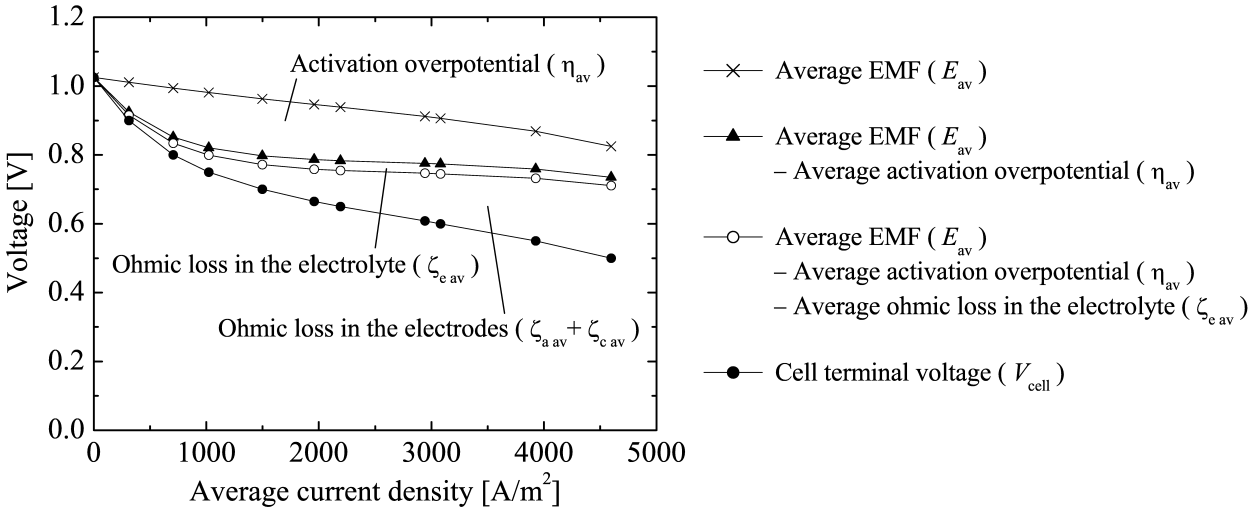


Figure 4.12: Cell terminal voltage and losses/overpotentials vs. average current density under the constant gas inlet conditions rather than under the constant cell operating temperature (Base case).

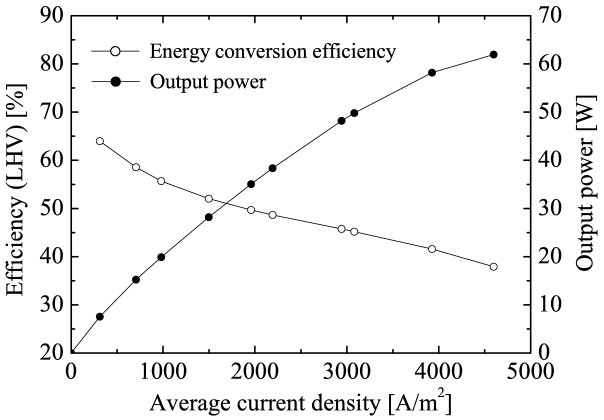


Figure 4.13: Efficiency and output power vs. average current density (Base case).

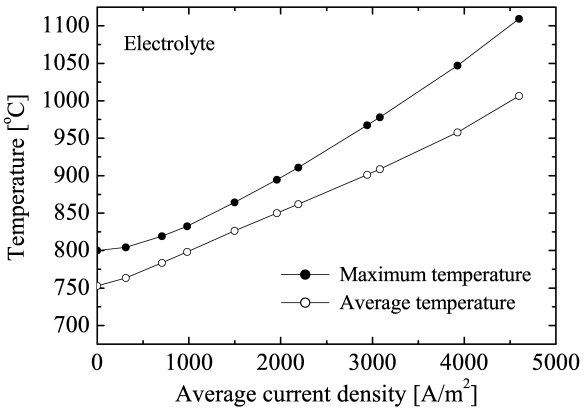


Figure 4.14: Electrolyte temperature vs. average current density (Base case).

Figure 4.13 shows the pattern of changes in the LHV-based energy conversion efficiency, $\mathcal{E}$, and the cell output power, $\mathcal{P}$, against the average current density. From this figure, it can be confirmed that the energy conversion efficiency decreases in a similar way to the cell terminal voltage shown in Fig. 4.12 with increase in the average current density. On the other hand, the cell output power increases as the average current density increases, though the rate of increase in the output power falls due to decrease in the cell terminal voltage. Finally, the pattern of changes in the maximum and average temperatures in the electrolyte layer against the average current density is shown in Fig. 4.14. From this figure, it can be confirmed that the maximum and average temperatures become higher as the average current density becomes larger, and the gap between the two temperatures also becomes larger.

Considering the temperature dependency of both the activation overpotential and ohmic loss in the electrolyte, it can be expected that the power generation performance of the cell should be degraded with decrease in the average temperature of the cell tube. Meanwhile, it is preferable that the maximum temperature and also the temperature gradients of the cell be reduced in order to avoid the risk of thermal crack failures as mentioned before. Therefore, how to reduce the gap between the two curves shown in Fig. 4.14 (in other words, how to bring the cell temperature field close to uniform) is important for the development/operation of the cell. This is a key point in the parametric studies given in the following sections.

## 4.3 Effect of Gas Inlet Temperature

This section discusses the effects of gas inlet temperatures on the thermal field and power generation performance of the cell based on the calculation results for Case T-750 and T-850. In these cases, the inlet temperatures of both fuel and air are set at 750°C and 850°C, respectively. The other conditions are same as those for the Base case except for the fuel inlet velocity, which is adjusted to keep the upper limit of the average current density 5000A/m$^2$, and the cell terminal voltage (see Table 4.1).

First of all, the cell performance results for Case T-750 and T-850 obtained under the standard operating conditions ($i_{\rm av} \simeq 4000$) are shown in Table 4.6. Compared to the results for the Base case of $i_{\rm av} = 3926$ in Table 4.5, it can be seen that the cell terminal voltage, which provides an indication of the cell performance under the same average current density, is clearly changed under the influence of the gas inlet temperature. In connection with this, both the maximum and average temperatures of the electrolyte are also changed. However, the gap between the maximum and average temperatures seems to become a little smaller as the gas inlet temperature becomes higher. The reasons for the above are examined below.

Table 4.6: Cell performance results for Case T-750 and T-850.

| Case | | T-750 | T-850 |
|---|---|---|---|
| Average current density, $\mathsf{i}_{\rm av}$ | [A/m$^2$] | 3922 | 3922 |
| Terminal voltage, $\mathsf{V}_{\rm cell}$ | [V] | 0.485 | 0.58 |
| Output power, $\mathcal{P}$ | [W] | 51.2 | 61.3 |
| Energy conversion efficiency, $\mathcal{E}$ | [%] | 36.7 | 43.9 |
| Fuel utilization factor, $\mathcal{U}_{\rm fuel}$ | [%] | 78.4 | 78.4 |
| Air utilization factor, $\mathcal{U}_{\rm air}$ | [%] | 13.3 | 14.6 |
| Reforming rate, $\mathcal{R}$ | [%] | 100.0 | 100.0 |
| Maximum temperature of the electrolyte | [°C] | 1013.1 | 1093.0 |
| Average temperature of the electrolyte | [°C] | 906.1 | 1011.7 |

Figure 4.15 shows the temperature contours for Case T-750 and T-850. From this figure, it can be seen that the overall characteristics of the thermal field for the two cases are not so different: the cell temperature has a peak around $x = 0.3$ to 0.4 while it significantly decreases near the inlet of the feed tube. However, the temperature gradient pattern seems to be a little different. Figure 4.16 shows a comparison of the electrolyte temperature between Case T-750, T-850 and the Base case. From this figure, it can be seen that the local temperature differences between the three cases are larger around $x = 0.1$ rather than around the peak of the temperature. This is not due to the differences in the progress of the steam reforming because they are quite small as shown in Fig. 4.17. It is true that the progress of the steam reforming becomes slightly faster/slower due to the higher/lower temperature, but the fact remains that the methane is fully reformed near the inlet of the feed tube in all the three cases.

The main reason for the differences in the temperature gradient patterns for the three cases are those in the progress of the electrochemical reactions. Figure 4.18 shows a comparison of the current density distribution in the electrolyte between the three cases. From this figure, it

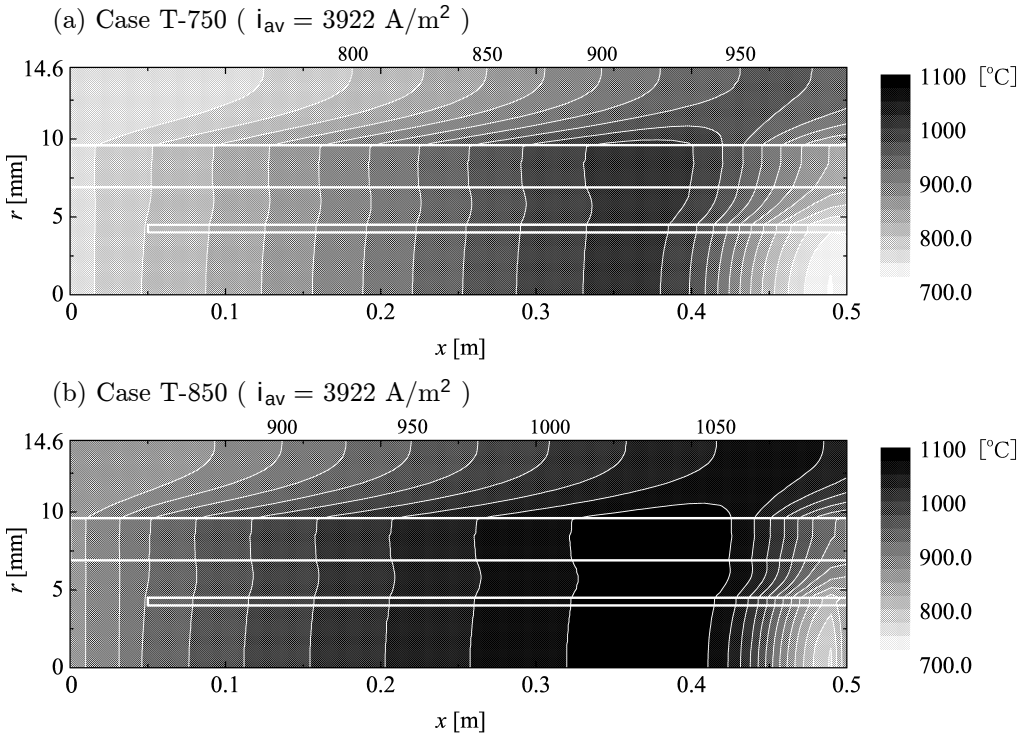


Figure 4.15: Temperature contours for Case T-750 and T-850.

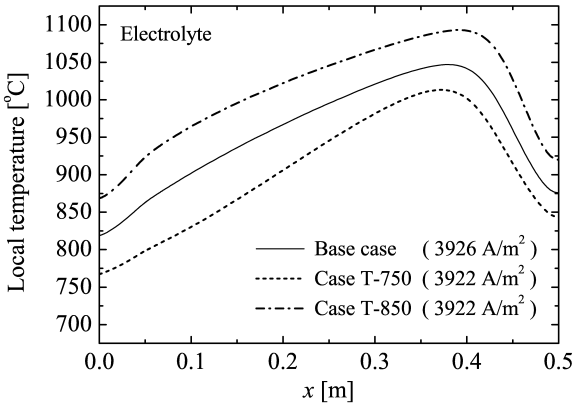


Figure 4.16: Temperature gradients for Case T-750, T-850 and the Base case.

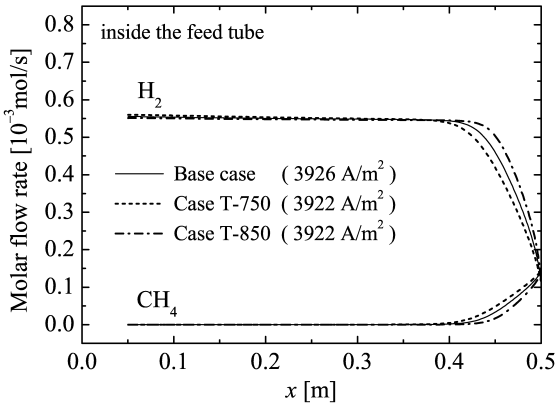


Figure 4.17: Molar flow rate of hydrogen and methane for Case T-750, T-850 and the Base case.

can be observed that the peak of the current density moves toward the outlet of the cell tube, which means that the peak of the heat generation also moves, as the gas inlet temperature decreases. The reason of this is indicated by Fig. 4.19 showing the distribution pattern of the losses/overpotentials for Case T-750 and T-850. In Case T-750, the effect of activation overpotential is severe especially near the outlet of the feed tube due to the low temperatures. Meanwhile, in Case T-850, the activation overpotential is not so large even near the outlet of the feed tube, therefore the larger current flows there owing to the higher EMF. Additionally, it is also seen from Fig. 4.19 that the difference in the extent of the activation overpotential directly affects the magnitude of the cell terminal voltage.

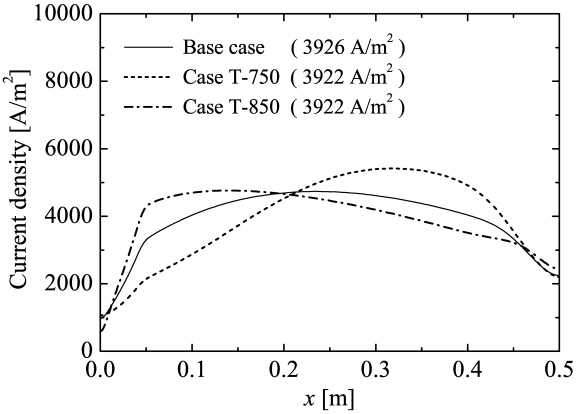


Figure 4.18: Current density distribution in the electrolyte for Case T-750, T-850 and the Base case.

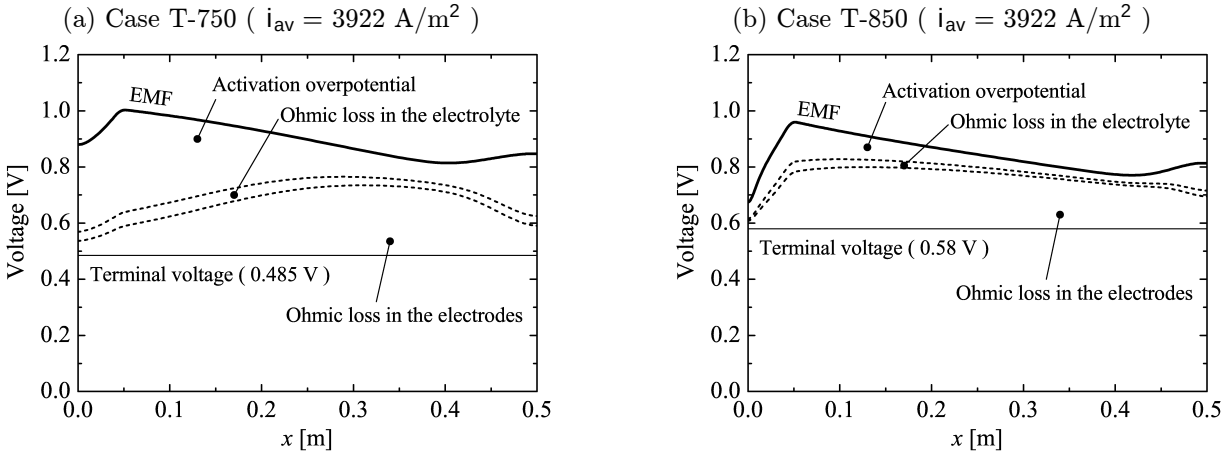


Figure 4.19: Distribution pattern of all the factors causing the voltage drop of the cell (Case T-750 and T-850).

Here the power generation performance for Case T-750 and T-850 is examined in a little more detail by showing the results for several different average current densities. Figure 4.20 shows the pattern of changes in the cell terminal voltage against the average current density for Case T-750, T-850 and the Base case. From this figure, it can be seen that the gas inlet temperature affects the cell performance especially for the low-output conditions. This is mainly due to the temperature dependency of the activation overpotential: it tends to increase exponentially as the cell temperature falls, particularly below 800°C.

Finally, the pattern of changes in the maximum and average temperature in the electrolyte against the average current density for the three cases is shown in Fig. 4.21. From this figure, it can be found that the maximum temperature difference between the Base case and Case T-750 becomes a little smaller as the average current density increases, while the average temperature increases almost proportionally to the average current density similarly in the three cases. This implies that the non-uniformity of the cell thermal field tends to be expanded with increase in the average current density especially in the cases of lower gas inlet temperatures.

As described above, the gas inlet temperature affects the thermal field and power generation characteristics of the cell in various forms. Generally speaking, however, the most fundamental

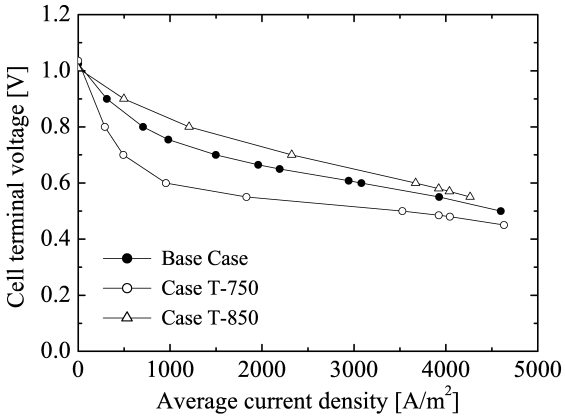


Figure 4.20: Cell terminal voltage vs. average current density for Case T-750, T-850 and the Base case.

(a) Maximum temperature

(b) Average temperature

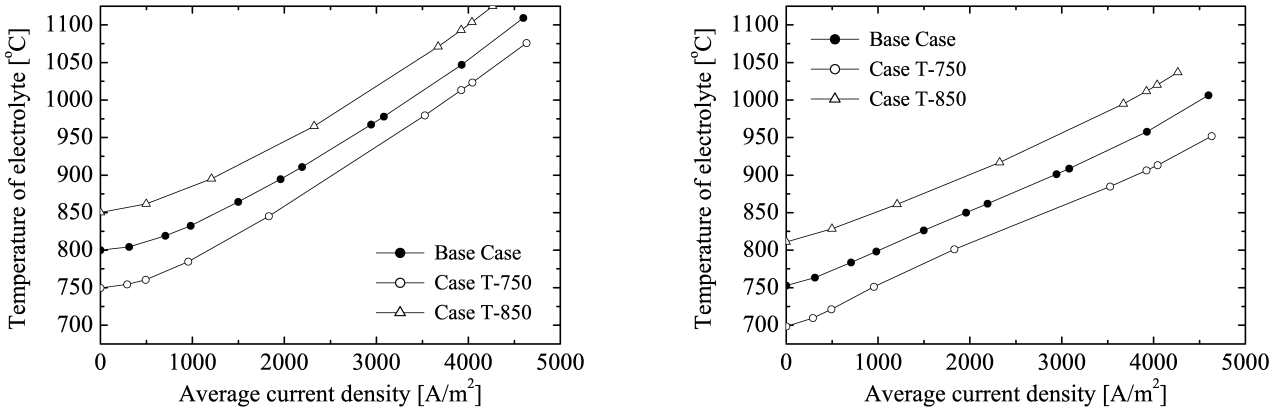


Figure 4.21: Electrolyte temperature vs. average current density for Case T-750, T-850 and the Base case.

effect of the gas inlet temperature is still to change the overall cell temperature. That is, we can reduce the maximum temperature of the cell by reducing the gas inlet temperatures, but cannot reduce the temperature gradient of the cell. Furthermore, the cell performance is necessarily degraded due to decrease in the average temperature of the cell.

## 4.4 Effect of Air Flow Rate

In this section, the effect of air flow rate on the thermal field of the cell is discussed based on the calculation results for Case AF-10 and AF-40. In these cases, the air mean velocity at the inlet is set at 1.0 and 4.0 m/s (which correspond to 22.8 and 91.2 L/min in terms of volumetric flow rate), respectively. The other conditions are same as those for the Base case except for the cell terminal voltage (see Table 4.1).

In the cell of IIR-T-SOFCs focused on in this study, the air flow rate is one of the most important factors affecting the operating temperature of the cell. This is due to the large heat capacity flow rate of the air. For example, in the Base case of $i_{\mathrm{av}} = 3926$, the heat capacity flow rate of the air at the inlet is about 0.3 W/K while that of the fuel is about 0.04 W/K. In the same case, for comparison, the thermodynamic/ohmic heat generation rate for the entire cell by the electrochemical reaction is about 90 W while the heat absorption rate for the entire cell by the steam reforming reaction is about 30 W. From these data, it can be easily expected that the air flow rate should significantly affect the temperature field of the cell. This is the reason why the air flow rate is taken up in this section.

Table 4.7 shows the cell performance results for Case AF-10 and AF-40 obtained under the standard operating conditions. Compared to the previous cases, it is confirmed that the electrolyte temperature is greatly affected by the air flow rate. In Case AF-10, the maximum temperature rises to over 1200°C, which is definitely over the limit for the cell tube. On the other hand, in Case AF-40, the average temperature is reduced to the same level as Case T-750, and more noteworthy is the maximum temperature reduced further than Case T-750. This means that the non-uniformity of the cell temperature is fairly reduced.

Table 4.7: Cell performance results for Case AF-10 and AF-40.

| Case | | AF-10 | AF-40 |
|---|---|---|---|
| Average current density, $\mathsf{i}_{\mathrm{av}}$ | [A/m$^2$] | 3969 | 3920 |
| Terminal voltage, $\mathsf{V}_{\mathrm{cell}}$ | [V] | 0.565 | 0.5 |
| Output power, $\mathcal{P}$ | [W] | 60.4 | 52.8 |
| Energy conversion efficiency, $\mathcal{E}$ | [%] | 42.9 | 37.8 |
| Fuel utilization factor, $\mathcal{U}_{\mathrm{fuel}}$ | [%] | 79.4 | 78.4 |
| Air utilization factor, $\mathcal{U}_{\mathrm{air}}$ | [%] | 28.3 | 7.0 |
| Reforming rate, $\mathcal{R}$ | [%] | 100.0 | 100.0 |
| Maximum temperature of the electrolyte | [°C] | 1215.9 | 968.0 |
| Average temperature of the electrolyte | [°C] | 1075.8 | 909.5 |

Figure 4.22 shows the temperature contours for Case AF-10 and AF-40. Note that the color tone level is exceptionally a little different in Case AF-10 due to the too-high temperatures. The following Fig. 4.23 shows a comparison of the electrolyte temperature between Case AF-10, AF-40 and the Base case. From these figures, it can be seen that the cell temperature, especially the maximum one, is drastically changed depending on the air flow rate, and accordingly the temperature gradients are also changed. In general terms, the air flow rate basically affects "how close" the overall cell temperature is to the air inlet temperature. This is in contrast to

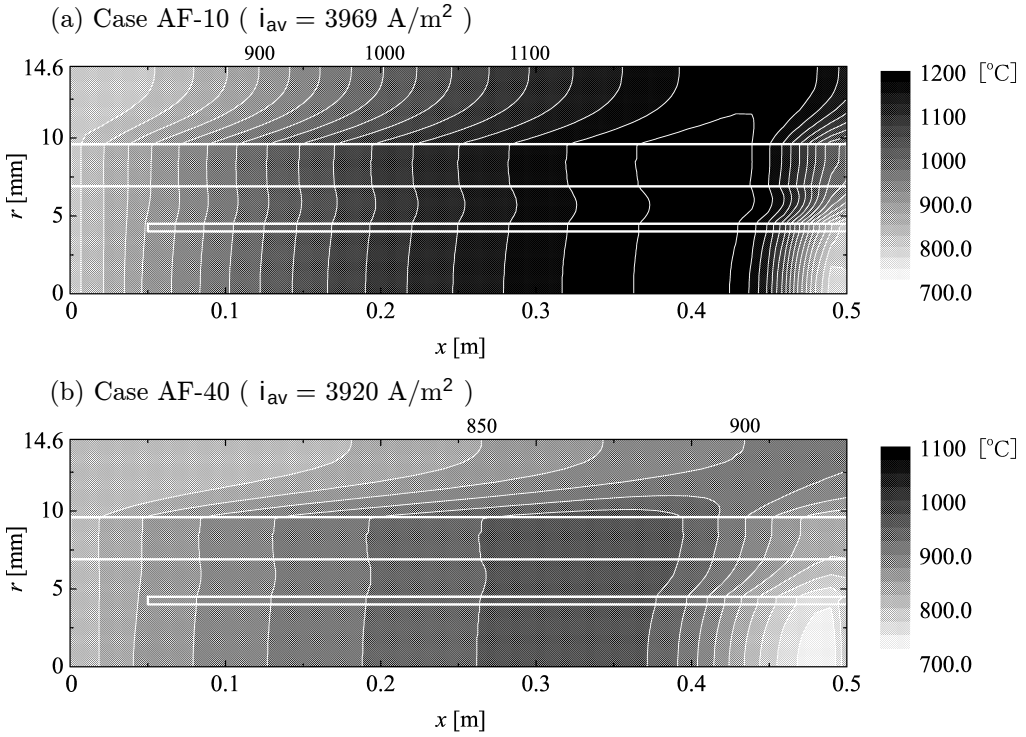


Figure 4.22: Temperature contours for Case AF-10 and AF-40.

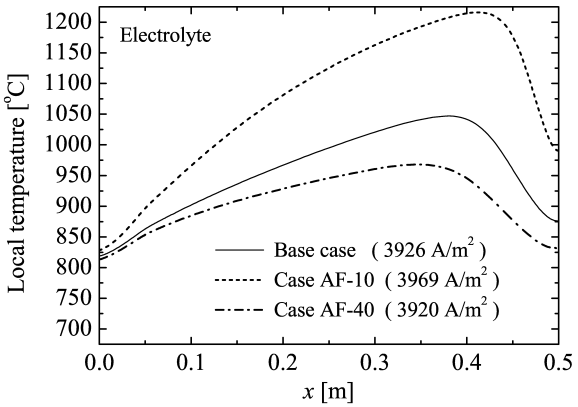


Figure 4.23: Temperature gradients for Case AF-10, AF-40 and the Base case.

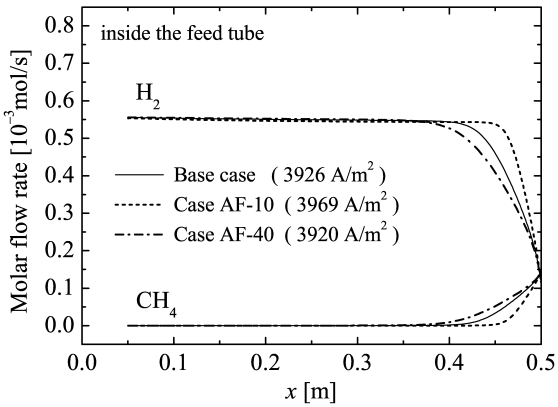


Figure 4.24: Molar flow rate of hydrogen and methane for Case AF-10, AF-40 and the Base case.

the gas inlet temperature affecting "how high" the overall cell temperature is. By the way, the progress of the steam reforming is still not so changed as shown in Fig. 4.24.

Figure 4.25 presents the distribution pattern of losses/overpotentials causing the voltage drop of the cell for Case AF-10 and AF-40. Note that the distribution pattern of the ohmic loss in the electrodes for each case is similar to that of the current density shown in Fig. 4.26 owing to the weak temperature dependency of the resistivities of the electrodes. In Case AF-10, the activation overpotential becomes quite small around $x = 0.3$ to 0.4, but concurrently the EMF remarkably decreases there due to the extremely high temperatures. Meanwhile, in Case AF-40, the activation overpotential is not so small even around $x = 0.3$ to 0.4. However,

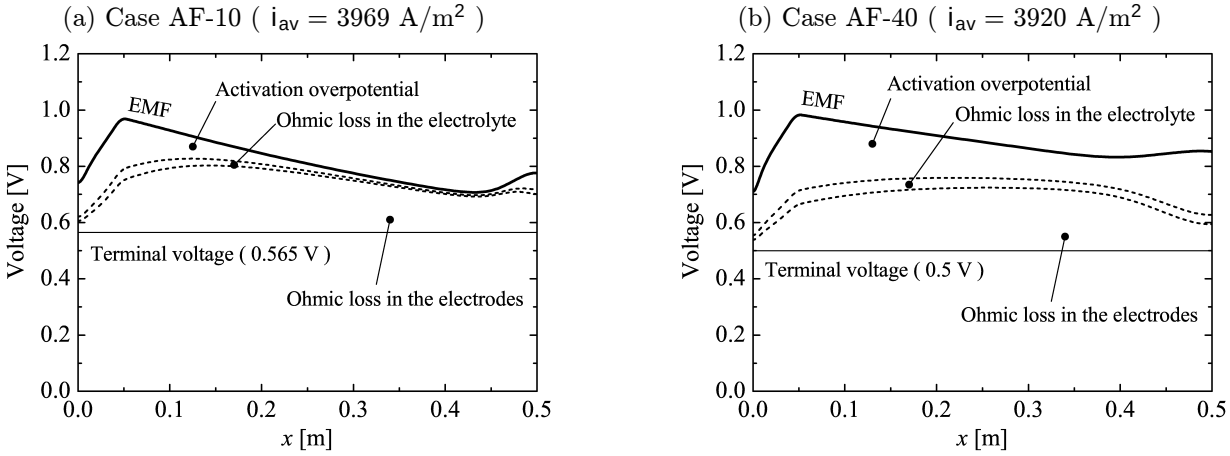


Figure 4.25: Distribution pattern of all the factors causing the voltage drop of the cell (Case AF-10 and AF-40).

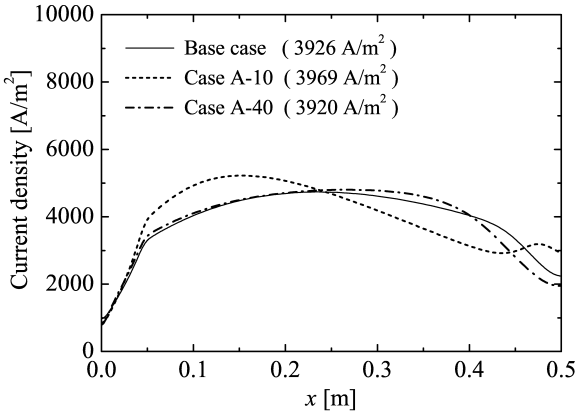


Figure 4.26: Current density distribution in the electrolyte for Case AF-10, AF-40 and the Base case.

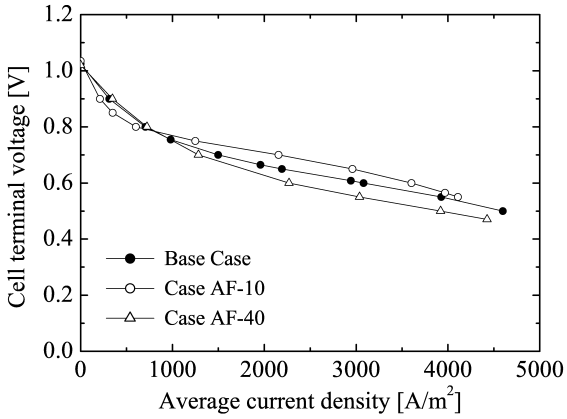


Figure 4.27: Cell terminal voltage vs. average current density for Case AF-10, AF-40 and the Base case.

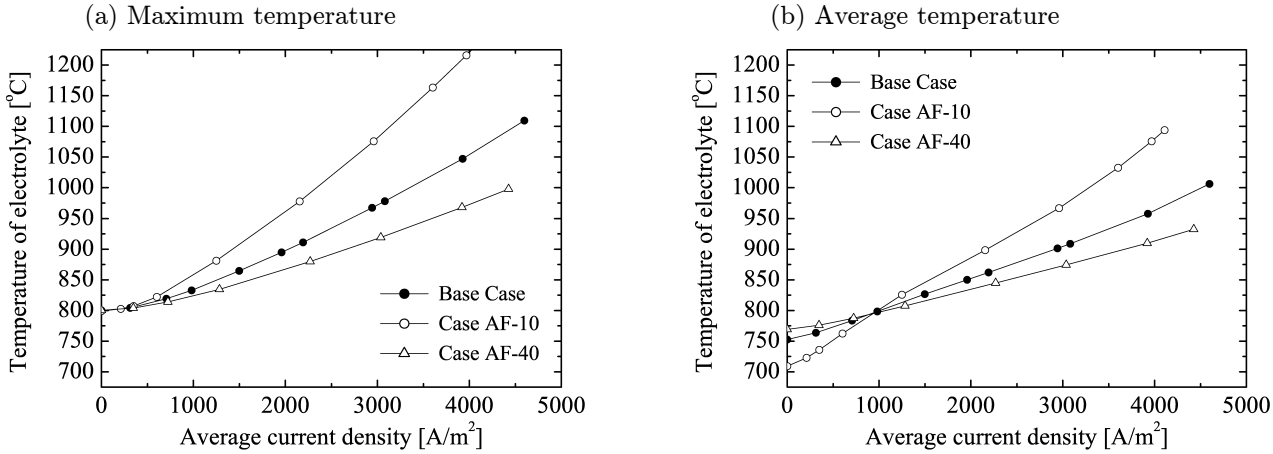


Figure 4.28: Electrolyte temperature vs. average current density for Case AF-10, AF-40 and the Base case.

compared to Case T-750 shown in Fig. 4.19, the activation overpotential is a little smaller near the outlet of the feed tube, therefore the cell terminal voltage is kept a little higher than that in Case T-750.

Figure 4.27 shows the pattern of changes in the cell terminal voltage against the average current density for Case AF-10, AF-40 and the Base case. The difference between Case AF-40 and the Base case can be explained with the temperature dependency of the activation overpotential in a similar way to the previous section. The large voltage drop in the very low-output region for Case AF-10 is also caused by the larger activation overpotentials due to the lower temperatures as is shown in Fig. 4.28, while the steeper voltage drop in the high-output region is caused by the drastic fall in the EMF due to the extremely high temperatures.

Paying attention to Fig. 4.28, it is observed that the air flow rate clearly affects the rate of increase in the electrolyte temperature, especially in the maximum one, associated with increase in the average current density. It is also observed that the curves of the average temperature vs. average current density for the three cases cross each other at about 800°C, the air inlet temperature. This also indicates the fact that the air flow rate basically affects "how close" the overall cell temperature is to the air inlet temperature.

To sum up the matter, we can reduce both the maximum temperature and temperature gradients of the operating cell by increasing the air flow rate. On the contrary, shortages of the air supplied to the cell can cause a disastrous rise in temperature as shown above. The air flow rate is a quite effective factor in controlling the thermal field of the cell. In this connection, however, it should be noted that the range of air flow rate will be limited to some degree by the requirements from the topping/bottoming devices or the like in practical use. In addition, the higher pumping powers are required to supply the larger amounts of air to the cell.

## 4.5 Effect of Steam-Methane Ratio

In this section, the effect of steam-methane ratio in the fuel gas mixture supplied to the cell is discussed with the calculation results for Case SM-11 and SM-41. As mentioned in the preceding section, the heat capacity flow rate of the fuel gas mixture is basically much smaller than that of the air, therefore the heat removal effect by the fuel gas flow should be rather small even if the flow rate is changed to some extent. However, the composition of the fuel gas mixture supplied to the cell, especially the ratio of steam to methane, may considerably affect the cell thermal field through the effects on both the internal reforming and electrochemical processes. The main purpose of this section is to figure out the above thing.

In the present study, the flow rate of fuel gas mixture is decided in such a way that the upper limit of the average current density is $5000\mathrm{A/m^2}$ as a basis of comparison between the different calculation cases summarized in Table 4.1. To examine the effects of steam-methane ratio with keeping this basis, the inlet molar flow rate of only steam is changed here. To be specific, in Case SM-11, the inlet molar flow rate of steam is reduced to half of the Base case to change the inlet steam-methane ratio from "2 : 1" to "1 : 1". Meanwhile, in Case SM-41, the inlet molar flow rate of steam is set to double the Base case, and accordingly the inlet steam-methane ratio "4 : 1". Note that the fuel mean velocity at the inlet is 0.75 times the Base case in Case SM-11, and 1.5 times the Base case in Case SM-41.

Table 4.8 shows the cell performance results for Case SM-11 and SM-41 obtained under the standard operating conditions. Compared to the Base case of $i_{\mathrm{av}} = 3926$ shown in Table 4.5, it can be found that both the maximum and average temperatures of the electrolyte are little changed depending on the steam-methane ratio, contrary to the expectation mentioned above. However, the cell terminal voltage is affected by the steam-methane ratio. For a deeper understanding, the thermal and electrical fields for these two cases are described below.

Table 4.8: Cell performance results for Case SM-11 and SM-41.

| Case | | SM-11 | SM-41 |
|---|---|---|---|
| Average current density, $\mathsf{i}_{\mathrm{av}}$ | $[\mathrm{A/m^2}]$ | 3958 | 3953 |
| Terminal voltage, $\mathsf{V}_{\mathrm{cell}}$ | [V] | 0.57 | 0.52 |
| Output power, $\mathcal{P}$ | [W] | 60.8 | 55.4 |
| Energy conversion efficiency, $\mathcal{E}$ | [%] | 42.9 | 39.8 |
| Fuel utilization factor, $\mathcal{U}_{\mathrm{fuel}}$ | [%] | 79.2 | 79.1 |
| Air utilization factor, $\mathcal{U}_{\mathrm{air}}$ | [%] | 14.1 | 14.1 |
| Reforming rate, $\mathcal{R}$ | [%] | 100.0 | 100.0 |
| Maximum temperature of the electrolyte | [°C] | 1049.2 | 1046.4 |
| Average temperature of the electrolyte | [°C] | 960.2 | 960.8 |

From the detailed results shown in Fig. 4.29 and also in Fig. 4.30, it can be seen that the steam-methane ratio in the supplied fuel has little effect on not only the maximum temperature but also the entire thermal field of the cell. This is due to the fact that the steam-methane ratio does not affect the progress of neither the steam reforming nor the electrochemical reactions substantially. Figure 4.31 shows the molar flow rate of hydrogen and methane inside the feed

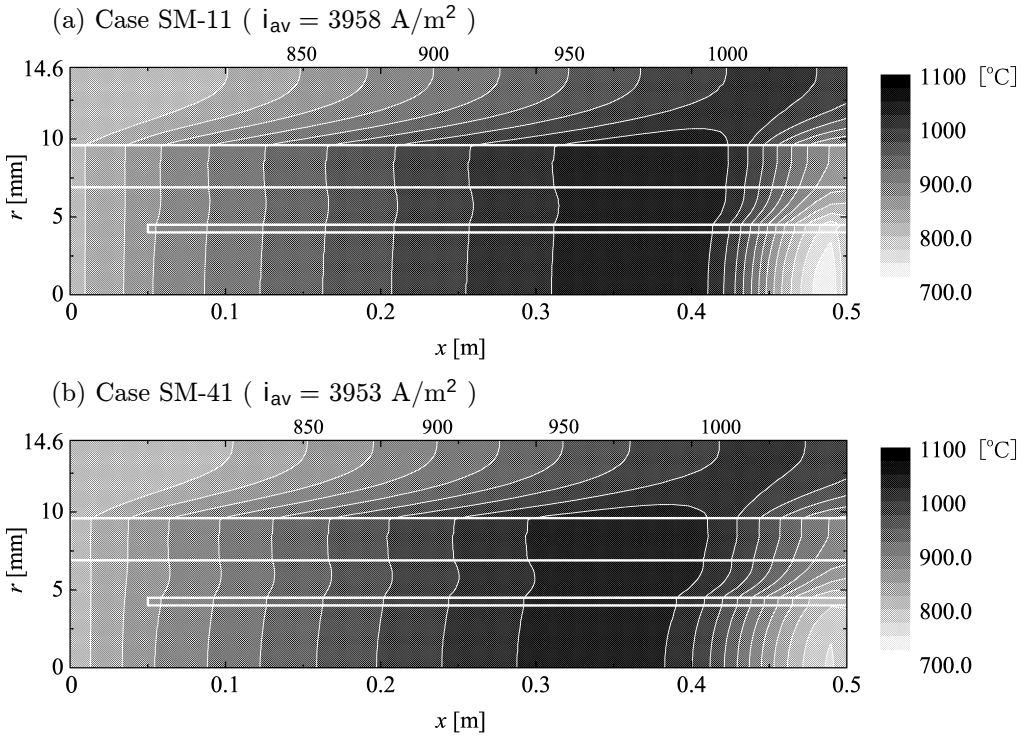


Figure 4.29: Temperature contours for Case AF-10 and AF-40.

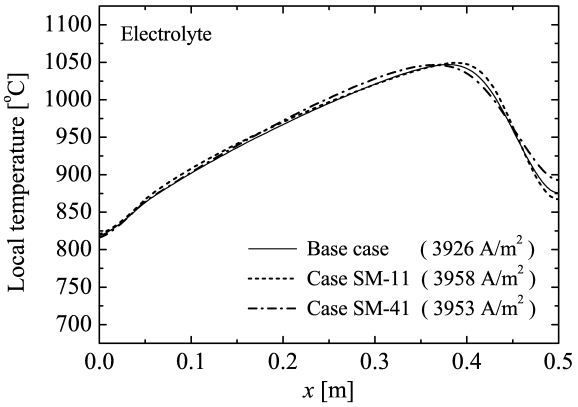


Figure 4.30: Temperature gradients for Case SM-11, SM-41 and the Base case.

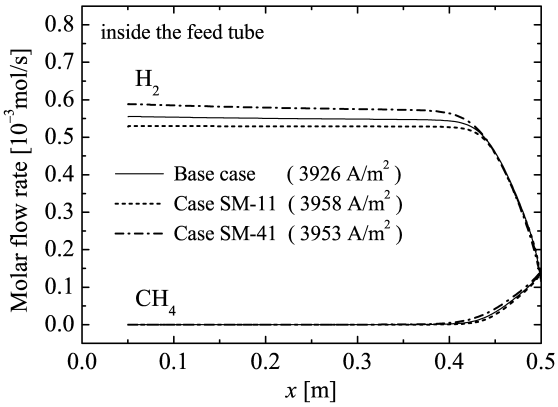


Figure 4.31: Molar flow rate of hydrogen and methane for Case SM-11, SM-41 and the Base case.

tube for the same cases. From this figure, it is confirmed that there is little difference in the progress of the steam reforming between the three cases. As indicated by eqn (3-51), the reaction rate of the steam reforming is moderated by lower partial pressures of methane and lower gas temperatures (and also smaller mass densities of the catalyst as will be discussed in the next section). Owing to the effect of the partial pressure of methane, the reaction rate is basically decreased with larger steam-methane ratios. However, considering only the effect of the gas temperature, the consequence is that the reaction rate should be increased with larger steam-methane ratios due to the larger amount of heat convected into the cell. This is one of the reasons why the reaction rate of the steam reforming is not so changed depending on the

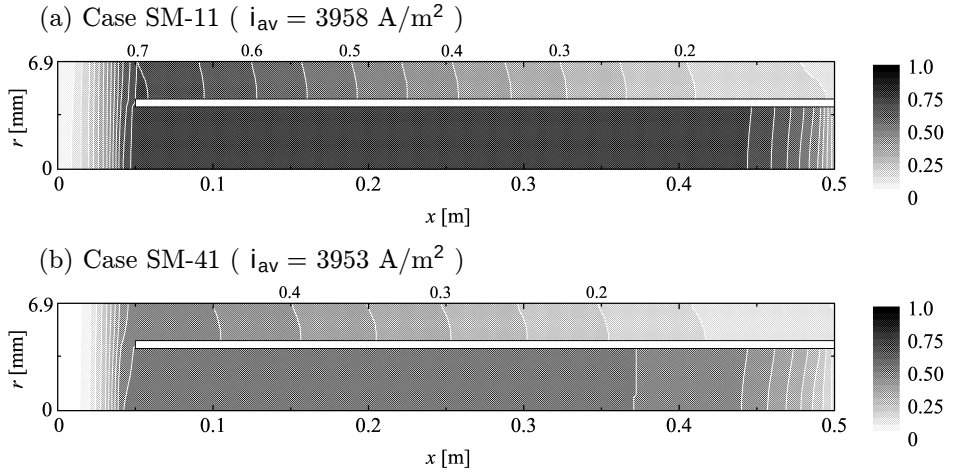


Figure 4.32: Molar fraction contours of hydrogen for Case SM-11 and SM-41.

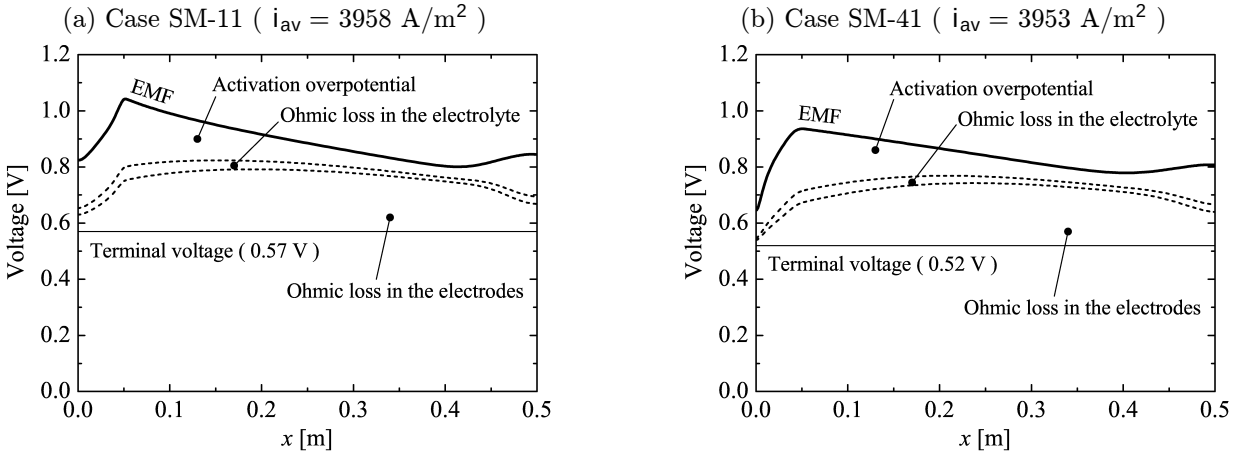


Figure 4.33: Distribution pattern of all the factors causing the voltage drop of the cell (Case SM-11 and SM-41).

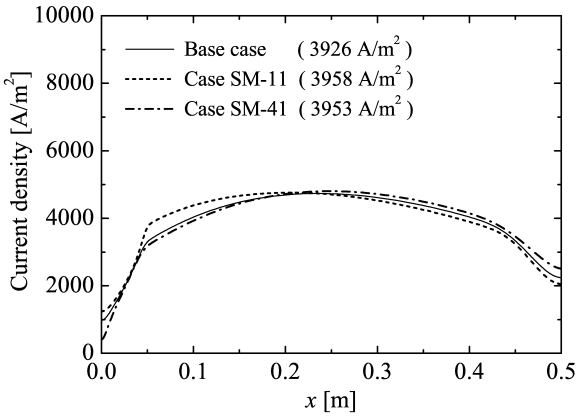


Figure 4.34: Current density distribution in the electrolyte for Case SM-11, SM-41 and the Base case.

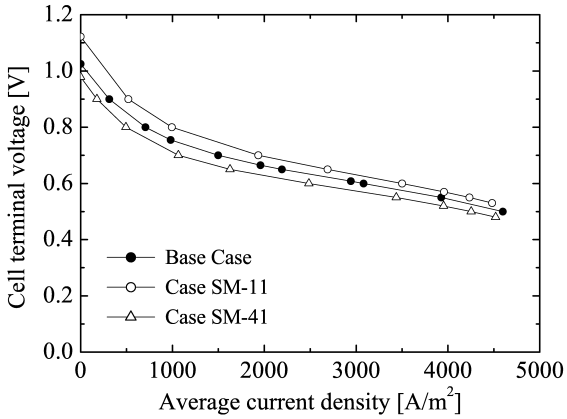


Figure 4.35: Cell terminal voltage vs. average current density for Case SM-11, SM-41 and the Base case.

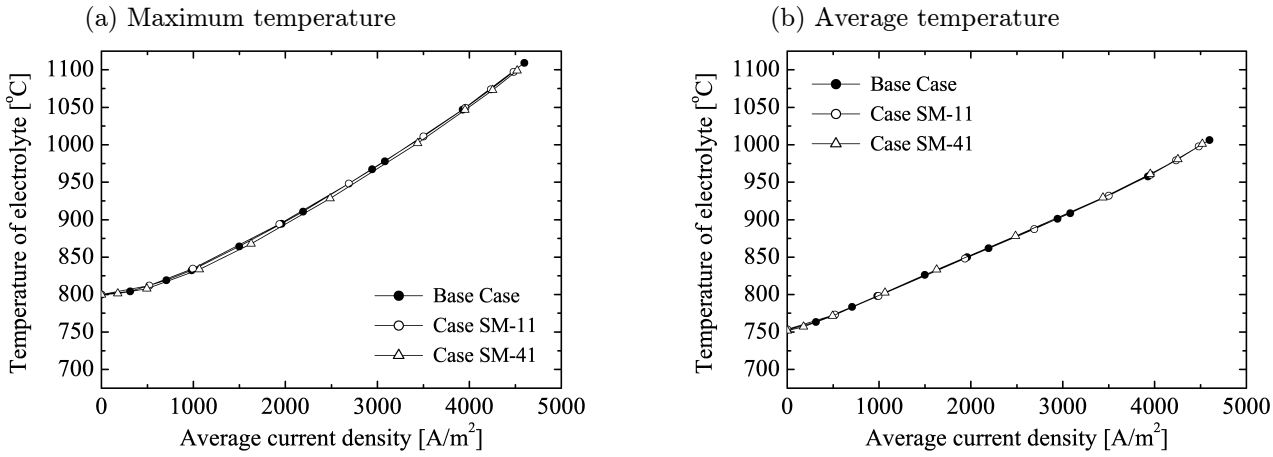


Figure 4.36: Electrolyte temperature vs. average current density for Case SM-11, SM-41 and the Base case.

steam-methane ratio. By the way, the slight differences in the molar flow rate of hydrogen are generated through the water-gas shift reaction. Note that the molar "fraction" of hydrogen is much larger in Case SM-11 than in Case SM-41 as shown in Fig. 4.32, though the molar flow rate of hydrogen is slightly larger in Case SM-41 than in Case SM-11.

As for the electrochemical process, Fig. 4.33 shows the distribution pattern of EMF and losses/overpotentials for Case SM-11 and SM-41. In this figure, it is observed that the magnitude of EMF differs between the two cases, especially near the outlet of the feed tube. This is due to the difference in the molar fraction of hydrogen shown in Fig. 4.32 (and also CO, $CO_2$ and steam not presented here). Under the influence of these different EMF distributions, the current density distribution also differs between the two cases as shown in Fig. 4.34, but not enough to change the characteristics of the temperature field of the cell. It follows that the distribution pattern of both the activation overpotential and ohmic loss is not so changed depending on the inlet steam-methane ratio, so that the cell terminal voltage simply decreases with EMF as the inlet steam-methane ratio increases.

Figure 4.35 shows the pattern of changes in the cell terminal voltage against the average current density for Case SM-11, SM-41 and the Base case. From this figure, it is confirmed that the power generation performance of the cell is enhanced by reducing the inlet steam-methane ratio in fuel. As mentioned above, the differences in the performance between the three cases directly result from those in the magnitude of EMF rather than the activation overpotential. Finally, the pattern of changes in the electrolyte temperature against the average current density for the three cases is shown in Figure 4.36. From this figure, it can be seen at a glance that the inlet steam-methane ratio in the fuel gas mixture has very little effect on the maximum and average temperatures of the cell.

As a conclusion, it has been revealed that the steam-methane ratio in the supplied fuel affects the power generation performance of the cell, but does not affect the temperature field of the cell substantially. This is quite a contrast to the effects of both the gas inlet temperature and air flow rate, which directly affect the thermal field of the cell and consequently the power generation performance of the cell as discussed in the previous sections.

## 4.6 Effect of Catalyst Distribution

In this section, the effects of the distribution pattern of the reforming catalyst, which is included in the porous medium embedded inside the feed tube, on the cell thermal field are discussed with the calculation results for Case CD-1 and CD-2. This is an interesting topic specific to the IIR-type fuel cells, and also one of the unique topics in the present study.

As referred to in the beginning of Section 4.4, in the Base case of $i_{\rm av} = 3926$, the amount of heat absorbed by the steam reforming for the entire cell per unit time is equivalent to about one-third of the amount of heat generated by the electrochemical reactions for the entire cell per unit time. This means that the internal reforming process has a decent impact on the characteristics of the overall cell thermal field. However, for all the standard operating cases of $i_{\rm av} \simeq 4000$ shown in the previous sections, the steam reforming has been completed near the inlet of the fuel, and accordingly the cell temperature has drastically fallen only there. This is mainly because the amount of the reforming catalyst has been optimized for the open-circuit cell rather than for the operating cell. Therefore, in Case CD-1, the amount of the catalyst is optimized for the operating conditions of $i_{\rm av} \simeq 4000$ : the amount of the catalyst is reduced to one-tenth of the Base case in order to reduce the reaction rate of the steam reforming and consequently to reduce the thermal gradients of the operating cell. Additionally, in Case CD-2, the distribution pattern of the catalyst is changed to the linear one rather than the uniform one as shown in Fig. 4.1. The intention of this will become apparent in the course of the following discussion.

Table 4.9 shows the cell performance results for Case CD-1 and CD-2 under the standard operating conditions. Compared to the results for the Base case, it is seen that the maximum temperature of the electrolyte is largely reduced while the average temperature is not so reduced by the adjustment of the amount/distribution of the reforming catalyst. This is also clearly seen by comparing Case CD-2 with A-40 shown in section 4.4: the maximum temperatures are almost the same while the average temperatures obviously differ between the two cases.

Table 4.9: Cell performance results for Case CD-1 and CD-2.

| Case | | CD-1 | CD-2 |
|---|---|---|---|
| Average current density, $\mathsf{i}_{\rm av}$ | [A/m$^2$] | 3911 | 3930 |
| Terminal voltage, $\mathsf{V}_{\rm cell}$ | [V] | 0.54 | 0.525 |
| Output power, $\mathcal{P}$ | [W] | 56.9 | 55.6 |
| Energy conversion efficiency, $\mathcal{E}$ | [%] | 41.0 | 39.9 |
| Fuel utilization factor, $\mathcal{U}_{\rm fuel}$ | [%] | 78.2 | 78.6 |
| Air utilization factor, $\mathcal{U}_{\rm air}$ | [%] | 13.9 | 14.0 |
| Reforming rate, $\mathcal{R}$ | [%] | 96.5 | 95.0 |
| Maximum temperature of the electrolyte | [°C] | 995.4 | 966.0 |
| Average temperature of the electrolyte | [°C] | 942.6 | 931.6 |

The effects of the smaller amount and the linear distribution of the catalyst on the thermal field of the cell are shown in Fig. 4.37. In this figure, it can be seen that the drastic decrease in temperature near the inlet of the fuel is inhibited by reducing the amount of the reforming

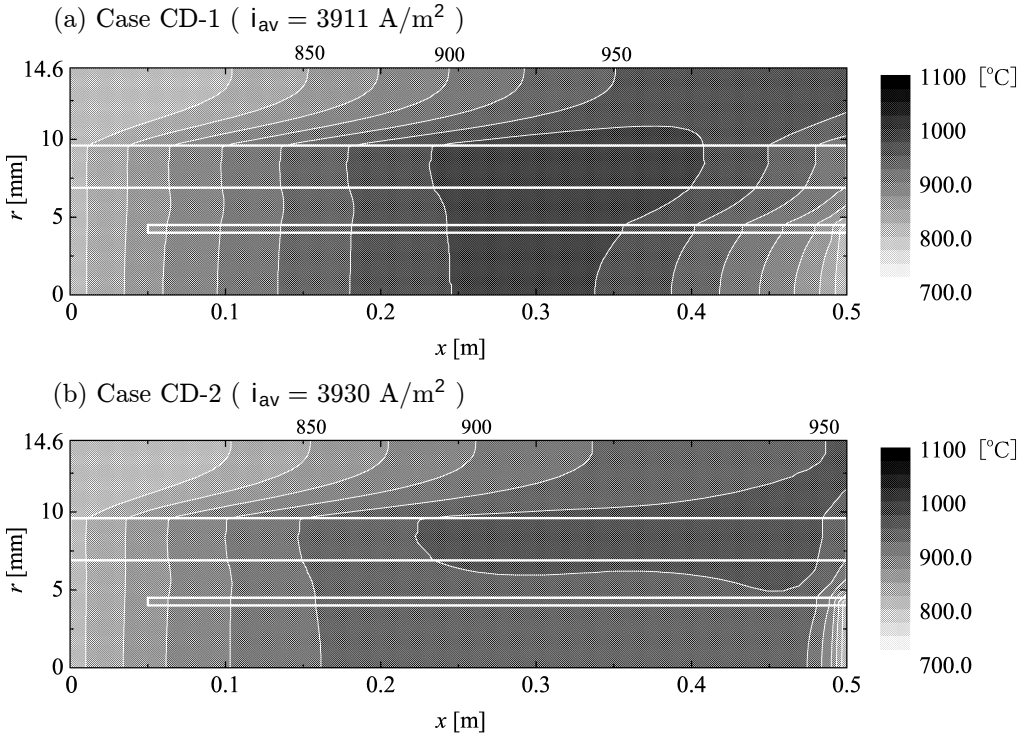


Figure 4.37: Temperature contours for Case CD-1 and CD-2.

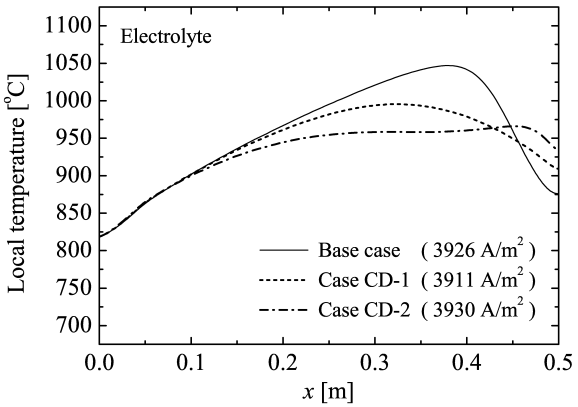


Figure 4.38: Temperature gradients for Case CD-1, CD-2 and the Base case.

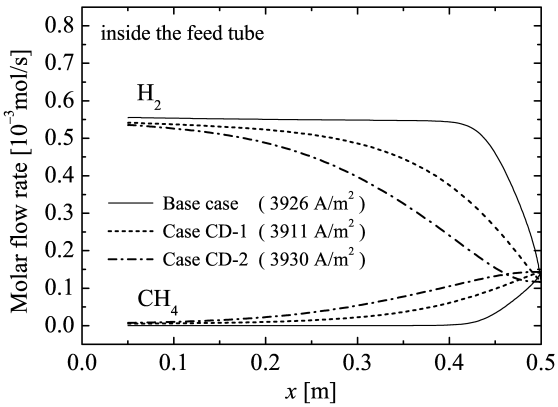


Figure 4.39: Molar flow rate of hydrogen and methane for Case CD-1, CD-2 and the Base case.

catalyst. In addition, it is seen that the linear distribution contributes to make the thermal field almost uniform in a larger region of the cell. These effects are also obvious in Fig. 4.38, which shows the temperature distribution in the electrolyte for the two cases and the Base case. In comparison with the Base case, the maximum temperature is reduced while the temperature near the inlet of the fuel increases in Case CD-1, and further in Case CD-2.

These positive changes in the characteristics of the thermal field of the cell are clearly explained in Fig. 4.39, which shows how the steam reforming proceeds inside the feed tube in the three cases. In Case CD-1, the steam reforming of methane proceeds at a lower rate than in the Base case due to the smaller amount of the catalyst, and is completed near the outlet of

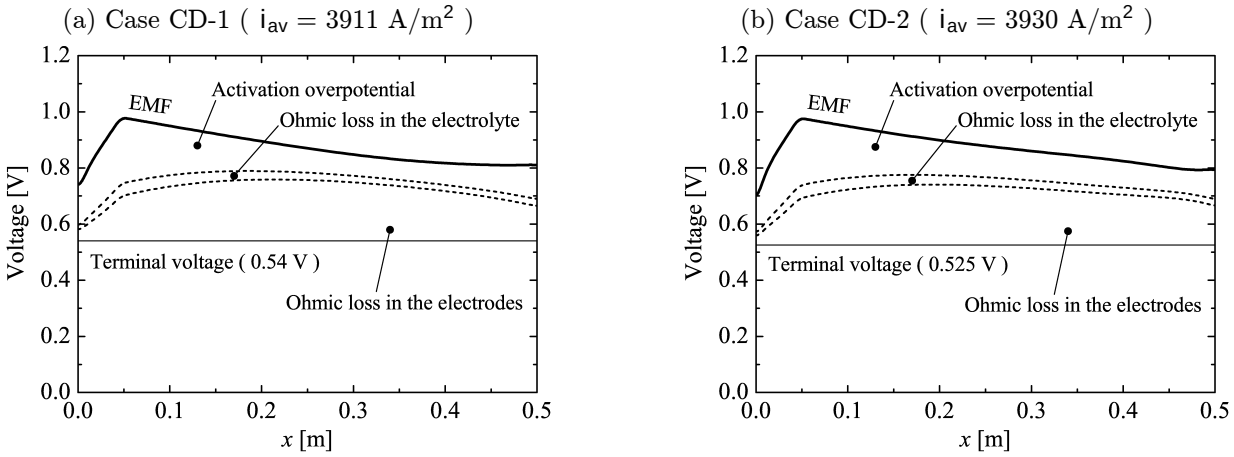


Figure 4.40: Distribution pattern of all the factors causing the voltage drop of the cell (Case CD-1 and CD-2).

the feed tube. This means that the amount of the catalyst in Case CD-1 is optimum for the operating state of $i_{\mathrm{av}} \simeq 4000$, or put it another way, the results for Case CD-1 show a kind of limit to the improvement of the thermal field by adjusting the amount of the catalyst with "uniform" distributions. If the amount of the catalyst is reduced further, the methane cannot be fully reformed inside the feed tube. Meanwhile, in Case CD-2, the steam reforming proceeds at a much lower rate than in Case CD-1 near the inlet, and is still completed near the outlet of the feed tube. This is the intention of the "linear" distribution of the catalyst, and actually results in the improvement of the cell thermal field as shown in Fig. 4.37 and 4.38.

The distinctive advantage of adjusting the amount and distribution pattern of the catalyst is that the maximum temperature and temperature gradients of the cell are reduced with little decrease in the power generation performance. Figure 4.40 shows the local EMF and losses/overpotentials for the two cases. Compared to the Base case shown in Fig. 4.11, it can be seen that the activation overpotentials in the two cases are a little larger around $x = 0.3$ to 0.4, but on the contrary, they are kept smaller near the outlet of the cell tube due to the higher temperatures. This results in the slight differences in the cell terminal voltage between the two cases and the Base case. Therefore, to adjust the amount and distribution pattern of the reforming catalyst is a very effective way to control the thermal field of the cell.

## 4.7 Effect of Electrode Resistivity and Thickness

This section examines the importance of the ohmic resistivity and thickness of the two electrode layers in the tubular cell. In the previous sections, all the calculated results concerning the electric potential/current fields were averaged in the circumferential ($\theta$) direction to be shown for the purpose of discussing the correlation with the cell thermal gradients in the axial ($x$) direction, and also with the power generation performance of the cell. As one of the results, it was revealed that the ohmic losses in the two electrodes were responsible for a considerable part of the voltage drop in the operating cell (e.g. see Fig. 4.11). This means that the ohmic resistivity and thickness of the electrodes have a great impact on the cell performance.

The electrode resistivity and thickness, however, affect not only the overall cell performance but also the electric potential/current distributions (and consequently the heat generation distributions) in the $\theta$-direction of the cell significantly. The "non-axisymmetry" of the thermal field of the cell cannot be investigated in this study due to the two-dimensional axisymmetric treatment in the thermo-fluid computation in the model. Nevertheless, it should be quite useful for understanding the distinctive feature of the tubular cell to examine how the electrode resistivity and thickness affect the electric potential/current fields in the $\theta$-direction of the cell. Hence, the non-axisymmetry of the electric potential/current fields will be examined first with the results for the Base case, and then the effects of the electrode resistivity and thickness are discussed with the results for Case E-0075 and E-0300, in which the anode thickness is different from the Base case.

### 4.7.1 Non-Axisymmetry of the Electric Current Field

Figure 4.41(a) shows the $r$-way current density field in the electrolyte layer for the Base case of $i_{\rm av} = 3926$ (the $\theta$-averaged data of which are shown in Fig. 4.7). Note that $\theta$=0° indicates the terminal side of the anode and $\theta$=180° the cathode as shown in Fig. 2.3. The half circumference of the electrolyte layer is about 27mm, so that the vertical scale of Fig. 4.41(a) corresponds to the length in the $\theta$-direction described ten times longer than that in the $x$-direction. From this figure, it can be seen that the current density field in the electrolyte layer, or the distribution pattern of the thermodynamic heat generations caused by the electrochemical reactions, is very non-uniform in the $\theta$-direction of the cell. It is also seen that the current density is particularly larger near the cathode terminal side of the cell. These non-axisymmetry of the current density in the electrolyte is deeply related to that of the electric potential and current fields in the two electrodes as shown in Fig. 4.41(b) to (g). Note that the contours shown in Fig. 4.41(b) to (d) indicate the $\theta$-way current per axial unit length of the cell, rather than the current density, for convenience of comparison between the two electrodes of different thicknesses.

To discuss the characteristics of those non-axisymmetry in more detail, the electric potential and current distributions in the $\theta$-direction in the cross section of $x = 0.3$ m are shown in Fig. 4.42. As shown in this figure, the $r$-way current density in the electrolyte layer is larger near the cathode terminal ($\theta$=180°) than near the anode terminal ($\theta$=0°), and at the same time, the $\theta$-way current flows more in the anode layer than in the cathode layer. Note that these current fields in the three layers are directly interrelated to each other through the Kirchhoff's first law (current conservation). The reason why the $\theta$-way current flows more in the anode than in the cathode, or why the current density in the electrolyte is larger near the cathode terminal, is

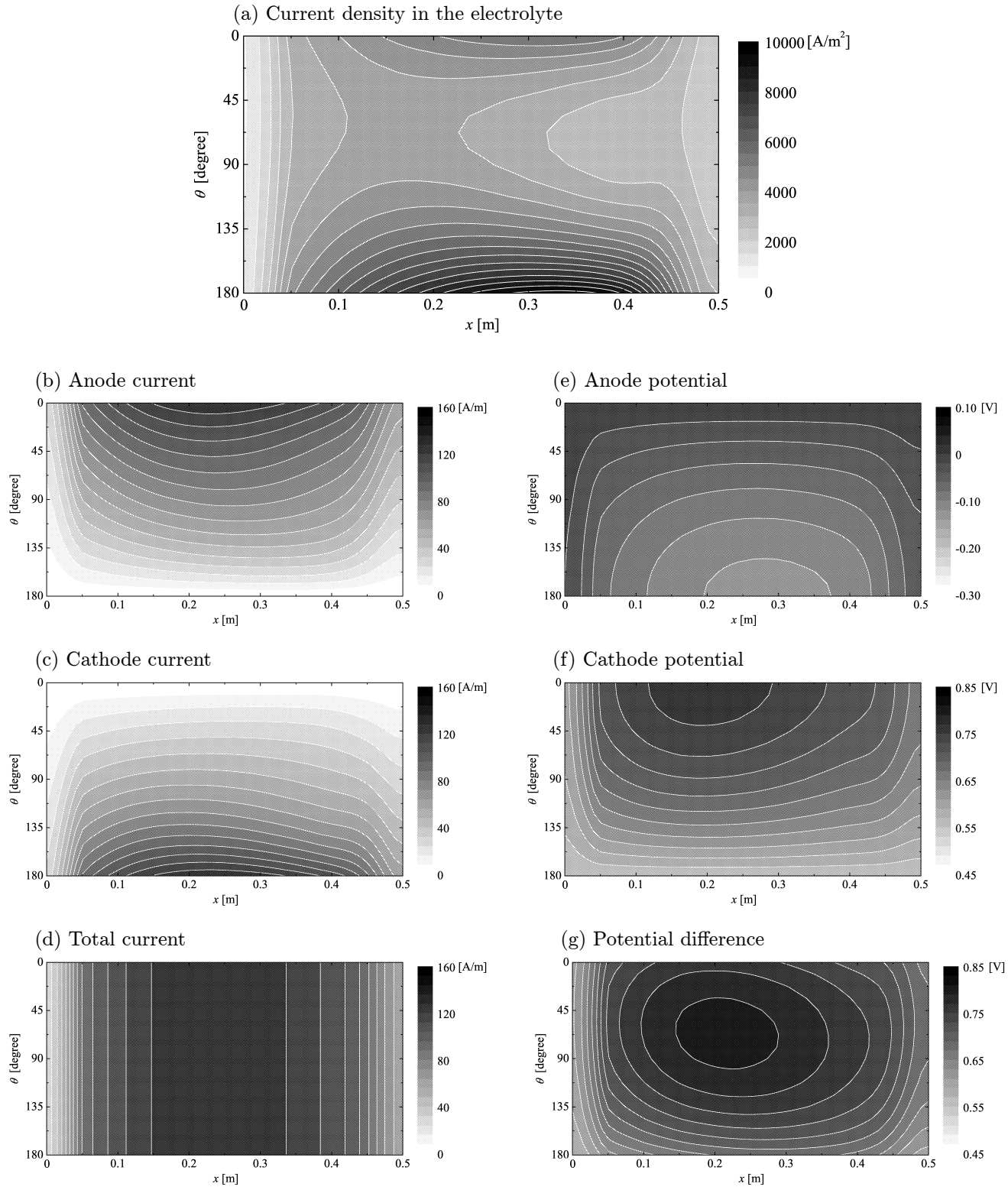


Figure 4.41: Electric potential/current fields for the Base case of $i_{\text{av}} = 3926$ A/m$^2$ : (a) $r$-way current density in the electrolyte, (b) $\theta$-way current per axial unit length in the anode, (c) $\theta$-way current per axial unit length in the cathode, (d) total $\theta$-way current per axial unit length in the two electrodes, (e) electric potential in the anode, (f) electric potential in the cathode, (g) potential difference between the two electrodes.

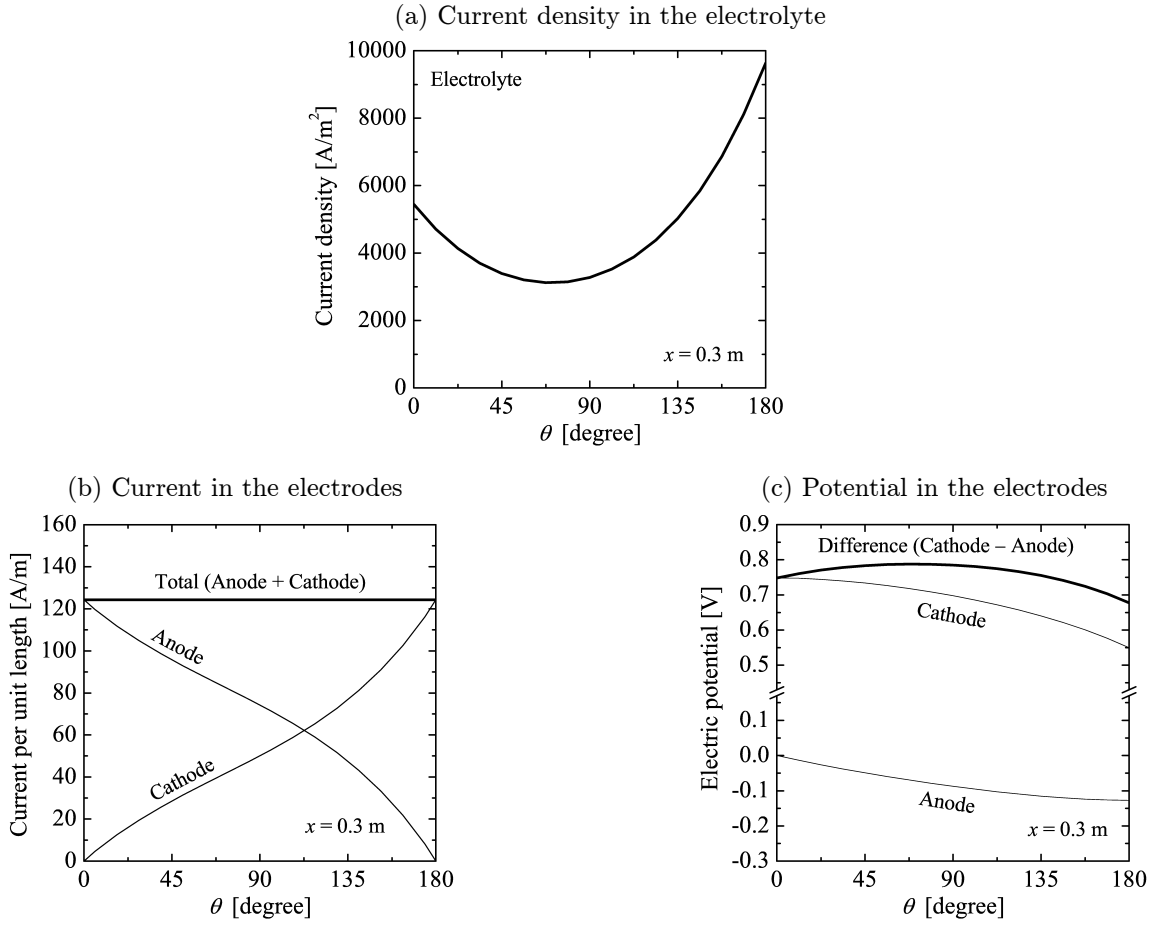


Figure 4.42: Electric potential/current distributions in the cross section of $x = 0.3$ m: (a) $r$-way current density in the electrolyte, (b) $\theta$-way currents per axial unit length in the two electrodes, (c) electric potentials in the two electrodes and the difference between them (Base case, $i_{\mathrm{av}} = 3926$ A/m$^2$).

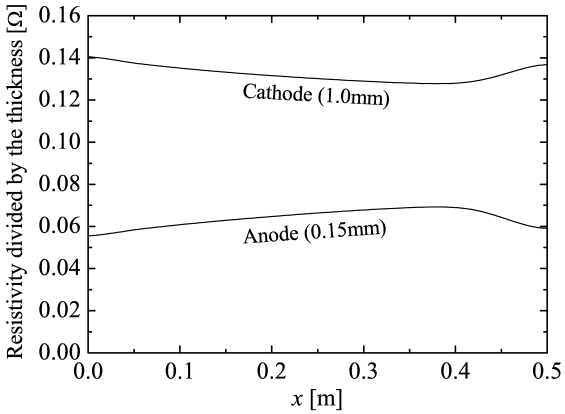


Figure 4.43: Distribution pattern of the ohmic resistivity of the electrodes divided by the thickness (Base case, $i_{\mathrm{av}} = 3926$ A/m$^2$).

that the ohmic resistance to the $\theta$-way current in the cathode is larger than that in the anode. Figure 4.43 shows the distribution pattern of the ohmic resistivity of the two electrodes divided by each thickness. From this figure, it is seen that the ohmic resistance to the $\theta$-way current in the cathode is about twice as large as that in the anode.

The effect of the difference in the ohmic resistance between the two electrodes is also seen in Fig. 4.42(c), which shows the electric potentials in the two electrodes and the difference between them. The ohmic loss in the cathode is larger than that in the anode due to the larger resistance. This was also shown in Fig. 4.10 in the $\theta$-averaged manner. But the more important thing found in Fig. 4.42(c) is that the potential difference between the two electrodes has a peak between the two terminals, $\theta$=0° and $\theta$=180°, due to the concave-upward distribution of the anode potential and the convex-upward distribution of the cathode potential shown in the figure. The reason of those potential distributions is that the $\theta$-way current decreases in the anode and increases in the cathode monotonously toward the cathode terminal, and this is also the fundamental reason why the current density in the electrolyte has a minimum value between the two terminals.

### 4.7.2 Effect of Electrode Thickness

For the practical development of the tubular cell, it is relatively easy to change the thickness of the electrodes compared to the ohmic resistivity of them. Hence it should be very useful to study the effect of the electrode thickness on the electric current field and also on the power generation performance of the cell. As shown in Table 4.4. in Case E-0075, the anode thickness is half of that in the Base case (0.075mm). Meanwhile, in Case E-0300, the anode thickness is twice that in the Base case (0.300mm). Note that the thickness of the support tube is also changed in the two cases so as not to change the area of the electrolyte layer and also the dimension of the cell tube itself.

Table 4.10 shows the cell performance results for the two cases obtained under the standard operating conditions of $i_{\rm av} \simeq 4000$. It is seen that the cell terminal voltage is substantially changed while the maximum and average temperatures of the electrolyte layer not so changed depending on the anode thickness. As shown in Fig. 4.44, the electrolyte temperature distributions for the two cases are similar to that for the Base case. Also the $\theta$-averaged current

Table 4.10: Cell performance results for Case E-0075 and E-0300.

| Case | | E-0075 | E-0300 |
|---|---|---|---|
| Average current density, $\mathsf{i}_{\rm av}$ | [A/m$^2$] | 3929 | 3964 |
| Terminal voltage, $\mathsf{V}_{\rm cell}$ | [V] | 0.49 | 0.58 |
| Output power, $\mathcal{P}$ | [W] | 51.9 | 61.9 |
| Energy conversion efficiency, $\mathcal{E}$ | [%] | 37.1 | 43.9 |
| Fuel utilization factor, $\mathcal{U}_{\rm fuel}$ | [%] | 78.6 | 79.3 |
| Air utilization factor, $\mathcal{U}_{\rm air}$ | [%] | 14.0 | 14.1 |
| Reforming rate, $\mathcal{R}$ | [%] | 100.0 | 100.0 |
| Maximum temperature of the electrolyte | [°C] | 1061.9 | 1044.1 |
| Average temperature of the electrolyte | [°C] | 971.1 | 952.9 |

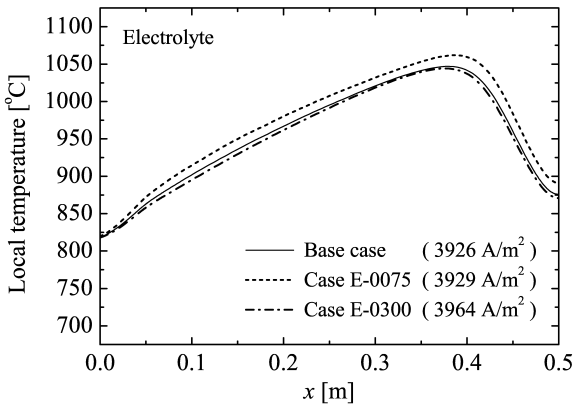


Figure 4.44: Temperature gradients for Case E-0075, E-0300 and the Base case.

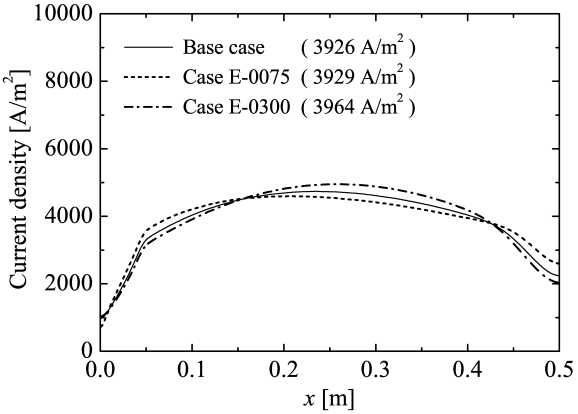


Figure 4.45: $\theta$-averaged current density distribution in the electrolyte layer for Case E-0075, E-0300 and the Base case.

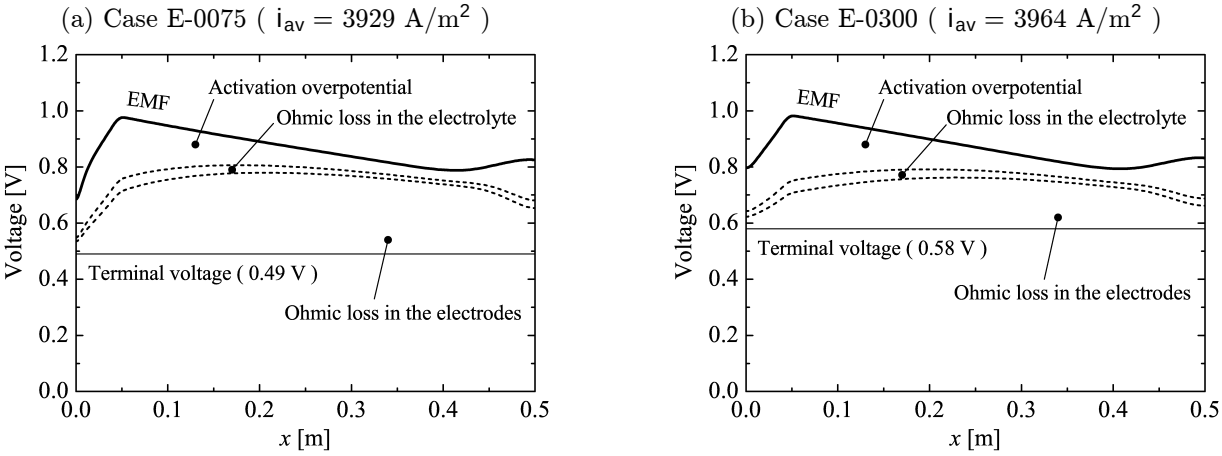


Figure 4.46: Distribution pattern of all the factors causing the voltage drop of the cell (Case E-0075 and E-0300).

density distribution in the electrolyte is not so affected by the differences in the anode thickness as shown in Fig. 4.45. The effect of the anode thickness visible in the $\theta$-averaged data is only the magnitude of the ohmic loss as shown in Fig. 4.46. In this figure, it is seen that the cell terminal voltage decreases as the anode becomes thinner due to the larger ohmic losses.

For the $\theta$-direction, however, the anode thickness greatly affects the characteristics of the current density field. Figure 4.47 shows the current density fields in the electrolyte for the two cases. The current density and potential distributions in the cross section of $x = 0.3$ m are shown in Fig. 4.48 and 4.49, respectively. In Case E-0075, the "anode-cathode asymmetry" is almost eliminated due to the same level of the ohmic resistances to the $\theta$-way currents in the two electrodes as shown in Fig. 4.50(a). But the remarkable "non-axisymmetry" in the electric potential/current fields still exist. On the other hand, in Case E-0300, the anode-cathode asymmetry is further extended due to the larger difference in the ohmic resistances in the two electrodes as shown in Fig. 4.50(b).

Although the non-axisymmetry of the thermal field of the cell cannot be investigated in the present study due to the axisymmetric thermo-fluid computation, it is a notable result that the

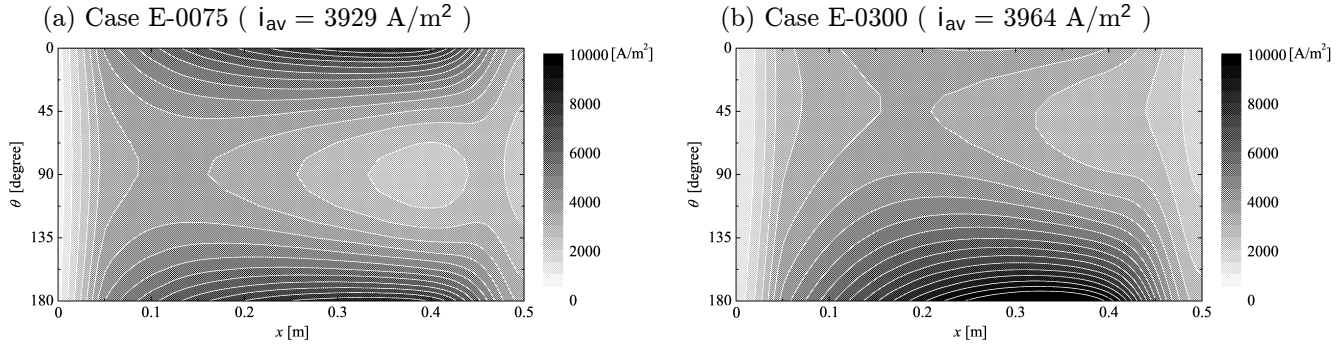


Figure 4.47: $r$-way current density fields in the electrolyte for Case E-0075 and E-0030.

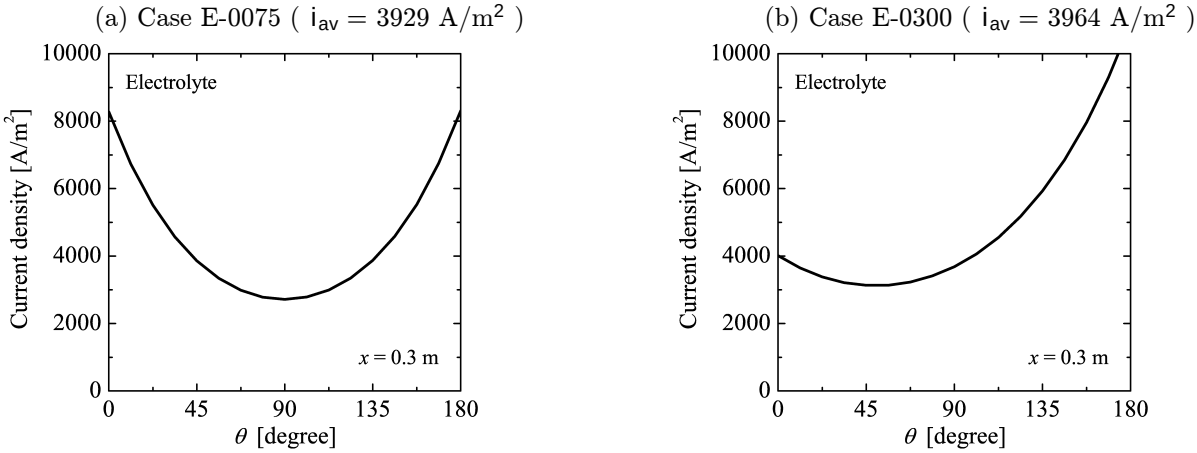


Figure 4.48: Current density distribution in the electrolyte in the cross section of $x = 0.3$ m for Case E-0075 and E-0030.

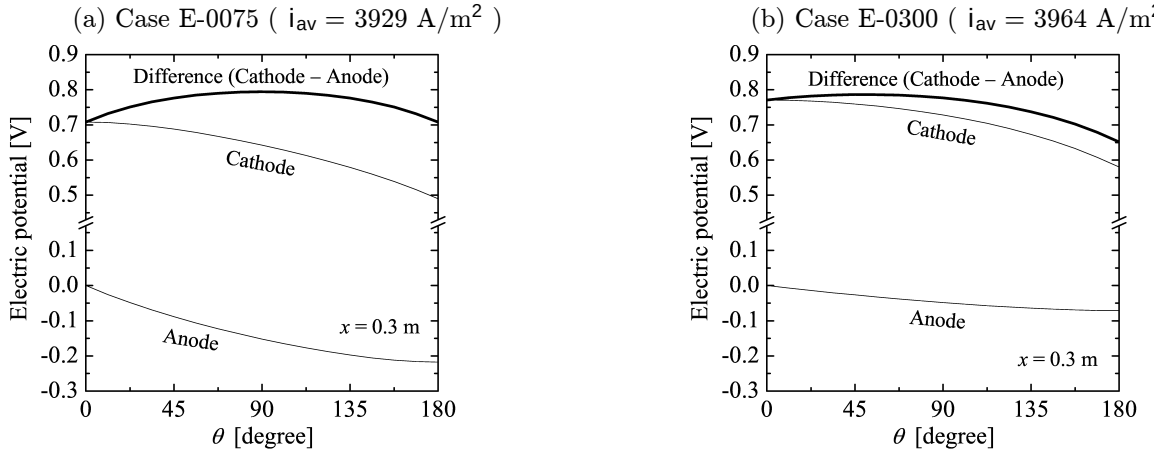


Figure 4.49: Electric potential distributions in the cross section of $x = 0.3$ m for Case E-0075 and E-0030.

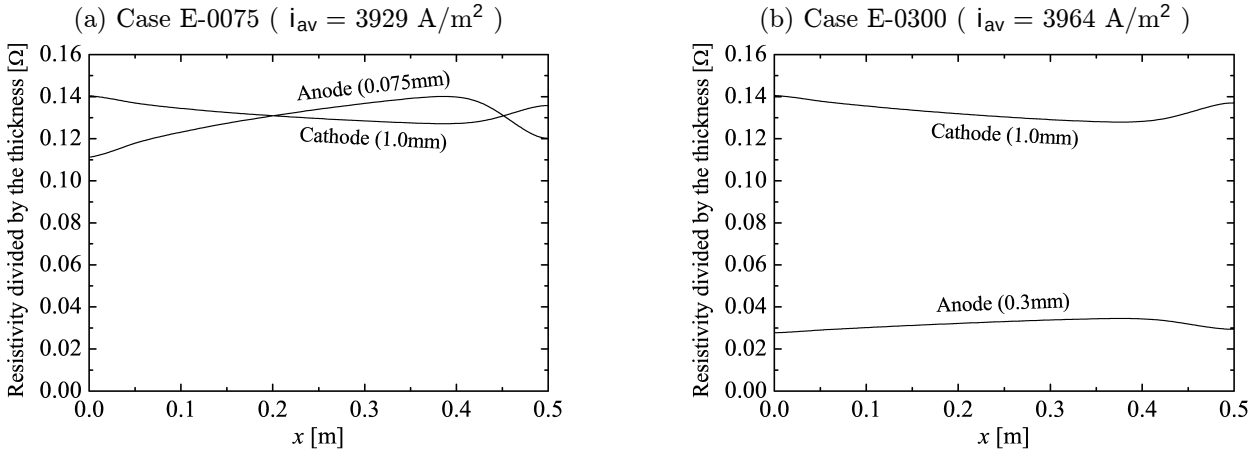


Figure 4.50: Distribution pattern of the ohmic resistivity of the electrodes divided by the thickness (Case E-0075 and E-0300).

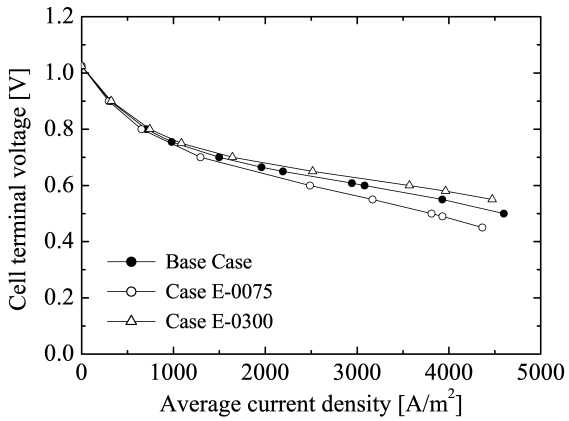


Figure 4.51: Cell terminal voltage vs. average current density for Case E-0075, E-0300 and the Base case.

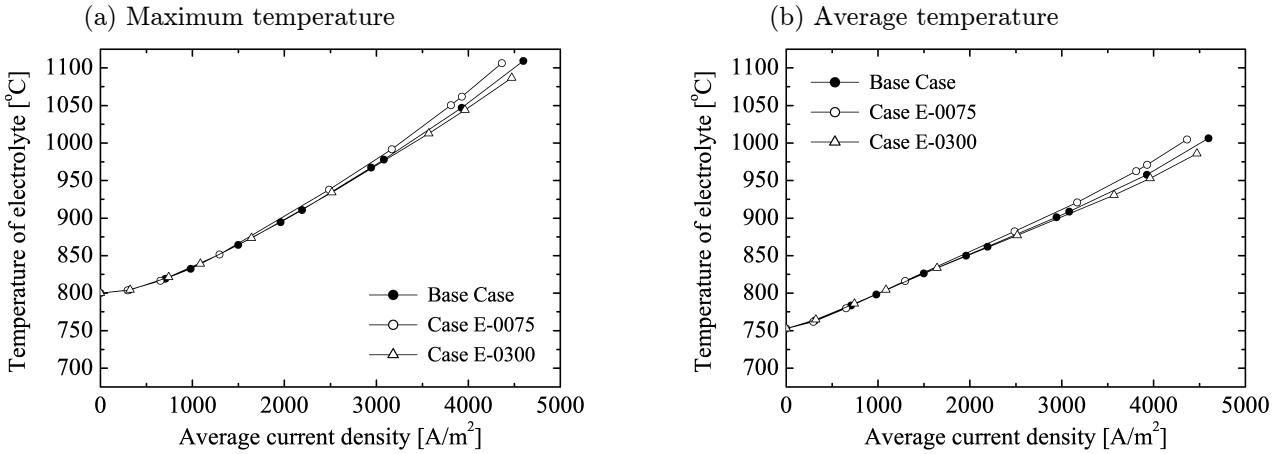


Figure 4.52: Electrolyte temperature vs. average current density for Case E-0075, E-0300 and the Base case.

electric current field essentially shows a significant non-axisymmetry despite the axisymmetric thermal/concentration fields in the cell. Considering the enhancing interaction between rise in temperature and increase in electric current found in the $x$-way characteristics in Section 4.2.2, the thermal field should also show a high non-axisymmetry in real tubular cells.

Finally, the patterns of changes in the cell terminal voltage and in the maximum/average electrolyte temperatures against the average current density are shown in Fig. 4.51 and 4.52, respectively. Owing to the weak temperature dependency of the ohmic resistivity of the anode, the differences in the cell terminal voltage among the three cases increase almost proportionally to the average current density. The differences in the electrolyte temperatures are not much, but also grow as the average current density increases due to the differences in the amount of ohmic heat generation in the anode.

# Chapter 5

# Conclusions

In the present study, a comprehensive analytical model of an IIR-T-SOFC has been developed with the objectives of (i) proposing an appropriate numerical analytical method applicable to a wide variety of fuel cells and (ii) examining the feasibility of this advanced type of fuel cell. The achievements and findings obtained in this study are summarized below:

## Achievements in the Numerical Modelling

- A quasi-three-dimensional equivalent electrical circuit model was developed to be properly combined with an existing two-dimensional multicomponent thermo-fluid model.
- Effects of the internal reforming of methane, porous media flow inside the feed tube, and radiative heat transfer between the cell/feed tubes were newly built into the model.
- The electrochemical model was greatly improved so that the electrochemical reactions of both hydrogen and carbon monoxide were properly treated in the model.

## Findings from the Numerical Analysis

- Larger air flow rates contribute to the uniformization of the cell thermal field while lower gas inlet temperatures reduce the overall cell temperature.
- Lower steam-methane ratios improve the power generation performance of the cell and do not affect the characteristics of the cell thermal field substantially.
- The optimized amount and distribution pattern of the reforming catalyst greatly reduce both the maximum temperature and temperature gradients of the cell with little decrease in the power generation performance of the cell. This is a distinctive advantage of IIR-T-SOFCs focused on in this study.
- The electric current field in the cell essentially shows a high non-axisymmetric pattern, the characteristics of which are affected by the ohmic resistivity and thickness of the two electrodes.

# Bibliography


[1] Suzuki, K., Iwai, H., Kim, J.H., Li, P.W., Teshima, K. (2002): Keynote paper: Solid Oxide Fuel Cell and Micro Gas Turbine Hybrid Cycle and related Fluid Flow and Heat Transfer, Proc. 12th International Heat Transfer Conference, August 18-23, Grenoble, France.

[2] Suzuki, K., Song, T.W., Iwai, H. (2002): Invited Paper: Micro Gas Turbine - Solid Oxide Fuel Cell Hybrid System for Distributed Energy Generation, Proc. Int. Symposium on Distributed Energy Systems in the 21st Century, September 24-25, Tokyo, Japan.

[3] Dicks, A.L. (1998): Advances in catalyst for internal reforming in high temperature fuel cells, Journal of Power Sources, Vol. 71, pp. 111-122.

[4] Ahmed, K., Foger, K. (2000): Kinetics of internal reforming of methane on Ni/YSZ-based anodes for solid oxide fuel cells, Catalysis Today, Vol. 63, pp. 479-487.

[5] Takeguchi, T., Kikuchi, R., Yano, T., Eguchi, K., Murata, K. (2003): Effect of precious metal addition to Ni-YSZ cermet on reforming of $CH_4$ and electrochemical activity as SOFC anode, Catalysis Today, Vol. 84, pp. 217-222.

[6] Park, H.K., Lee, Y.R., Kim, M.H., Chung, G.Y., Nam, S.W., Hong, S.A., Lim, T.H., Lim, H.C. (2002): Studies of the effects of the reformer in an internal-reforming molten carbonate fuel cell by mathematical modeling, Journal of Power Sources, Vol. 104, pp. 140-147.

[7] Aguiar, P., Chadwick, D., Kershenbaum, L. (2002): Modelling of an indirect internal reforming solid oxide fuel cell, Chemical Engineering Science, Vol. 57, pp. 1665-1677.

[8] Nishino, T., Komori, H., Iwai, H., Suzuki, K. (2003): Development of a Comprehensive Numerical Model for Analyzing a Tubular-Type Indirect Internal Reforming SOFC, Proc. 1st Int. Conf. on Fuel Cell Science, Engineering and Technology, eds. Shah, R.K. & Kandlikar, S.G., ASME, April 21-23, Rochester, NY, pp. 521-528.

[9] George, R.A. (2000): Status of tubular SOFC field unit demonstrations, Journal of Power Sources, Vol. 86, pp. 134-139.

[10] Nagata, S., Momma, A., Kato, T., Kasuga, Y. (2001): Numerical analysis of output characteristics of tubular SOFC with internal reformer, Journal of Power Sources, Vol. 101, pp. 60-71.

[11] Singhal, S.C. (2000): Advances in solid oxide fuel cell technology, Solid State Ionics, Vol. 135, pp. 305-313.

[12] Hatchwell, C., Sammes, N.M., Brown, I.W.M., Kendall, K. (1999): Current collectors for a novel tubular design of solid oxide fuel cell, Journal of Power Sources, Vol. 77, pp. 64-68.

[13] Mori, M., Sammes, N.M. (2002): Sintering and thermal expansion characterization of Al-doped and Co-doped lanthanum strontium chromites synthesized by the Pechini method, Solid State Ionics, Vol. 146, pp. 301-312.

[14] Xu, J., Froment, G.F. (1989): Methane Steam Reforming, Methanation and Water-Gas Shift: I. Intrinsic Kinetics, AIChE Journal, Vol. 35, No. 1, pp. 88-96.

[15] Xu, J., Froment, G.F. (1989): Methane Steam Reforming: II. Diffusional Limitations and Reactor Simulation, AIChE Journal, Vol. 35, No. 1, pp. 97-103.

[16] Larminie, J., Dicks, A. (2003): Fuel Cell Systems Explained 2nd Edition, John Wiley & Sons Ltd, Chichester, England.

[17] Li, P.W. (2001): Numerical Study of the Performance of Tubular Solid Oxide Fuel Cells -Effects of Geometric Parameters and Thermal Conditions, Meeting Report in Heat Transfer Laboratory, N01-66, Kyoto University, Japan.

[18] Suzuki, K., Li, P.W., Nishino, T., Komori, H. (2002): Internal Report in Heat Transfer Laboratory, HT2002-01-01, Kyoto University, Japan (in Japanese).

[19] Komori, H. (2002): Numerical Study Concerning the Effect of Fuel Gas Composition on the Electro-chemical and Thermal Characteristics of a Tubular-type SOFC, Master Thesis in Dept. Mechanical Engineering, Kyoto University, Japan.

[20] Patankar, S.V. (1980): Numerical Heat Transfer and Fluid Flow, Hemisphere Publishing Corporation, Washington.

[21] Carbonell, R.G., Whitaker, S. (1984): Heat and Mass Transfer in Porous Media, Fundamentals of Transport Phenomena in Porous Media, eds. Bear, J. & Corapcioglu, M.Y., Martinus Nijhoff Publishers, Dordrecht, Netherlands, pp. 123-198.

[22] Vafai, K., Tien, C.L. (1981): Boundary and Inertia Effects on Flow and Heat Transfer in Porous Media, Int. J. Heat Mass Transfer, Vol. 24, pp. 195-203.

[23] Incropera, F.P., Dewitt, D.P. (1996): Introduction to Heat Transfer 3rd Edition, John Wiley & Sons, New York.

[24] Bird, R.B., Stewart, W.E., Lightfoot, E.N. (2002): Transport Phenomena 2nd Edition, John Wiley & Sons, New York.

[25] Bromley, L.A., Wilke, C.R. (1951): Viscosity Behavior of Gases, Industrial and Engineering Chemistry Research, Vol. 43, No. 7, pp. 1641-1648.

[26] Dean, D.E., Stiel, L.I. (1965): The Viscosity of Nonpolar Gas Mixtures at Moderate and High Pressures, AIChE Journal, Vol. 11, No. 3, pp. 526-532.

[27] Lindsay, A.L., Bromley, L.A. (1950): Thermal Conductivity of Gas Mixtures, Industrial and Engineering Chemistry Research, Vol. 42, No. 8, pp. 1508-1511.

[28] Stiel, L.I., Thodos, G. (1964): The Thermal Conductivity of Nonpolar Substances in the Dense Gaseous and Liquid Regions, AIChE Journal, Vol. 10, No. 1, pp. 26-30.

[29] Wilke, C.R. (1950): Diffusional Properties of Multicomponent Gases, Chemical Engineering Progress, Vol. 46, No. 2, pp. 95-104.

[30] Fuller, E.N., Schettler, P.D., Giddings, J.C. (1966): A New Method for Prediction of Binary Gas-Phase Diffusion Coefficients, Industrial and Engineering Chemistry Research, Vol. 58, No. 5, pp. 19-27.

[31] Perry, R.H. (1997): Perry's Chemical Engineers' Handbook 7th Edition, McGraw-Hill, New York.

[32] Hageman, L.A., Young, D.M. (1981): Applied Iterative Methods, Academic Press, New York.

[33] Lehnert, W., Meusinger, J., Thom, F. (2000): Modelling of gas transport phenomena in SOFC anodes, Journal of Power Sources, Vol. 87, pp. 57-63.

[34] Chase, Jr. M.W., Davies, C.A., Downey, Jr. J.R., Frurip, D.J., McDonald, R.A., Syverud, A.N. (1985): JANAF Thermochemical Tables 3rd Edition, Journal of Physical and Chemical Reference Data, Vol. 14, Supplement No. 1.

[35] Achenbach, E. (1994): Three-dimensional and time-dependent simulation of a planar solid oxide fuel cell stack, Journal of Power Sources, Vol. 49, pp. 333-348.

[36] Bessette II, N.F., Wepfer, W.J., Winnick, J. (1995): A Mathematical Model of a Solid Oxide Fuel Cell, Journal of Electrochemical Society, Vol. 142, No. 11, pp. 3792-3800.

# Nomenclature

| | | |
|---|---|---|
| $a$ | coefficient in the discretized equations | |
| $A$ | activation energy | [J/mol] |
| $b$ | source term in the discretized equations | |
| $C_p$ | specific heat at constant pressure | [J/kg K] |
| $C_{pj}$ | specific heat at constant pressure of species $j$ | [J/kg K] |
| $D_{jk}$ | binary diffusivity for a gas mixture composed of species $j$ and $k$ | [$m^2$/s] |
| $D_{jm}$ | diffusivity of species $j$ in a multicomponent gas mixture | [$m^2$/s] |
| $D_{\mathrm{eff}jm}$ | effective diffusivity of species $j$ in a multicomponent gas mixture in porous area | [$m^2$/s] |
| $\mathcal{D}$ | diffusion conductance | |
| $e$ | emissivity | [−] |
| $E$ | electromotive force | [V] |
| $E^0$ | standard electromotive force | [V] |
| $\tilde{E}$ | substantial electromotive force defined by eqn (3-71) | [V] |
| $E_{\mathrm{av}}$ | average electromotive force | [V] |
| $\mathcal{E}$ | energy conversion efficiency | [%] |
| $f$ | inertia coefficient | [−] |
| $F$ | Faraday constant, 96486.7 | [C/mol] |
| $F_{11}, F_{12}, F_{21}, F_{22}$ | configuration factors | [−] |
| $\mathcal{F}$ | convection conductance | |
| $h$ | thickness | [m] |
| $H_j$ | lower heating value of species $j$ | [J/mol] |
| $i$ | electric current density | [A/$m^2$] |
| $i_{\mathrm{av}}$ | average current density | [A/$m^2$] |
| $I_{\mathrm{cell}}$ | total electric current | [A] |
| $J$ | radiosity | [W/$m^2$] |
| $k_{\mathrm{hyd}}, k_{\mathrm{co}}, k_{\mathrm{oxy}}$ | coefficients in eqns (3-60) to (3-62) | [A/$m^2$] |
| $k^+_{\mathrm{shift}}, k^-_{\mathrm{shift}}$ | velocity constants of the water-gas shift reaction | [mol/$m^3Pa^2s$] |
| $K$ | permeability | [$m^2$] |
| $K_{\mathrm{shift}}$ | equilibrium constant of the water-gas shift reaction | [−] |
| $L$ | cell length | [m] |
| $M_j$ | molecular weight of species $j$ | [kg/mol] |
| $\overline{M}$ | molar averaged molecular weight | [kg/mol] |

| | | |
|---|---|---|
| $n_{\mathrm{a}j}$ | mass flux of species $j$ from the anode surface to the fuel flow | [kg/m$^2$s] |
| $n_{\mathrm{c}j}$ | mass flux of species $j$ from the cathode surface to the air flow | [kg/m$^2$s] |
| $N_j$ | molar flow rate of species $j$ | [mol/s] |
| $P$ | total pressure | [Pa] |
| $P_j$ | partial pressure of species $j$ | [Pa] |
| $P_{\mathrm{cr}}$ | critical pressure | [Pa] |
| $P_{\mathrm{cr}j}$ | critical pressure of species $j$ | [Pa] |
| $\mathcal{P}$ | output power | [W] |
| Pe | Peclet number | [−] |
| $q_{\mathrm{hyd\cdot oxy}}, q_{\mathrm{co\cdot oxy}}$ | thermodynamic heat generations by the electrochemical reactions (per unit area of the electrolyte) | [W/m$^2$] |
| $q_{\mathrm{rad}}$ | net radiant flux | [W/m$^2$] |
| $Q$ | heat generation | [W/m$^3$] |
| $Q_{\mathrm{ohm}}$ | ohmic heat generation | [W/m$^3$] |
| $Q_{\mathrm{steam}}, Q_{\mathrm{shift}}$ | thermodynamic heat generations by the reforming reactions | [W/m$^3$] |
| $r$ | radial coordinate | [m] |
| $R$ | ohmic resistivity | [Ω m] |
| $R_{\mathrm{steam}}, R_{\mathrm{shift}}$ | reaction rates of the reforming reactions | [mol/m$^3$s] |
| $R_0$ | universal gas constant, 8.31434 | [Pa m$^3$/mol K] |
| $\mathcal{R}$ | reforming rate | [%] |
| $s_{\mathrm{hyd\cdot oxy}j}, s_{\mathrm{co\cdot oxy}j}$ | mass generations of species $j$ by the electrochemical reactions (per unit area of the electrolyte) | [kg/m$^2$s] |
| $S_j$ | mass generation of species $j$ | [kg/m$^3$s] |
| $S_{\mathrm{steam}j}, S_{\mathrm{shift}j}$ | mass generations of species $j$ by the reforming reactions | [kg/m$^3$s] |
| $\hat{S}$ | source term in the general transport equation | |
| $T$ | temperature | [K] |
| $T_{\mathrm{b}j}$ | boiling temperature of species $j$ | [K] |
| $T_{\mathrm{cr}}$ | critical temperature | [K] |
| $T_{\mathrm{cr}j}$ | critical temperature of species $j$ | [K] |
| $U_x, U_r$ | velocity components | [m/s] |
| $\mathcal{U}_{\mathrm{fuel}}$ | fuel utilization factor | [%] |
| $\mathcal{U}_{\mathrm{air}}$ | air utilization factor | [%] |
| $V$ | electric potential | [V] |
| $V_{\mathrm{cell}}$ | cell terminal voltage | [V] |
| $W_{\mathrm{cat}}$ | catalyst mass density | [g/cm$^3$] |
| $x$ | axial coordinate | [m] |
| $X_j$ | molar fraction of species $j$ | [−] |
| $Y_j$ | mass fraction of species $j$ | [−] |
| $Z_{\mathrm{cr}}$ | critical compressibility factor | [−] |

## Greek letters

| | | |
|---|---|---|
| $\alpha, \beta, \gamma$ | coefficients in eqn (3-21) | [–] |
| $\Gamma$ | diffusivity in the general transport equation | |
| $\delta r$ | range between grid points for $r$ direction | [m] |
| $\delta x$ | range between grid points for $x$ direction | [m] |
| $\delta\theta$ | range between grid points for $\theta$ direction | [rad] |
| $\Delta G^0_{\text{hyd·oxy}}, \Delta G^0_{\text{co·oxy}}$ | standard Gibbs free energy changes for the electrochemical reactions | [J/mol] |
| $\Delta H_{\text{hyd·oxy}}, \Delta H_{\text{co·oxy}}$ | enthalpy changes for the electrochemical reactions | [J/mol] |
| $\Delta H_{\text{steam}}, \Delta H_{\text{shift}}$ | enthalpy changes for the reforming reactions | [J/mol] |
| $\Delta N_j$ | variation of the molar flow rate of species $j$ | [m] |
| $\Delta r$ | range of a control volume for $r$ direction | [m] |
| $\Delta x$ | range of a control volume for $x$ direction | [m] |
| $\Delta\theta$ | range of a control volume for $\theta$ direction | [rad] |
| $\epsilon$ | porosity | [–] |
| $\zeta_{\text{e av}}, \zeta_{\text{a av}}, \zeta_{\text{c av}}$ | average ohmic losses in the electrolyte, anode and cathode | [V] |
| $\eta$ | activation overpotential | [V] |
| $\eta_{\text{av}}$ | average activation overpotential | [V] |
| $\theta$ | circumferential coordinate | [rad] or [ ° ] |
| $\Theta_j, \Theta_{jk}$ | parameters defined by eqn (3-20) | [K] |
| $\lambda$ | thermal conductivity | [W/m K] |
| $\lambda_{\text{eff}}$ | effective thermal conductivity in porous area | [W/m K] |
| $\lambda_{\text{s}}$ | thermal conductivity of solid | [W/m K] |
| $\lambda_j$ | thermal conductivity of species $j$ | [W/m K] |
| $\mu$ | viscosity | [Pa s] |
| $\mu_j$ | viscosity of species $j$ | [Pa s] |
| $\rho$ | density | [kg/m$^3$] |
| $\rho_{\text{cr}}$ | critical density | [kg/m$^3$] |
| $\rho_{\text{cr}j}$ | critical density of species $j$ | [kg/m$^3$] |
| $\rho_{\text{re}}$ | reduced density | [–] |
| $\hat{\rho}$ | density in the general transport equation | |
| $\sigma$ | Stefan-Boltzmann constant, $5.667\times10^{-8}$ | [W/m$^2$K$^4$] |
| $\Sigma v_j$ | diffusion volume of the molecules of species $j$ | [m$^3$/mol] |
| $\phi$ | variable in the general transport equation | |
| $\Phi_{jk}, \Psi_{jk}$ | interaction parameters for each pair of species $j$ and $k$ | [–] |

## Subscripts

| | |
|---|---|
| a | anode |
| air | air gas |
| av | cell-averaged value |

| | |
|---|---|
| c | cathode |
| cat | catalyst |
| cell | cell terminal/total value |
| co | anode reaction of CO: eqn (2-4) |
| co·oxy | electrochemical reaction of CO: eqn (2-7) |
| cr | critical value |
| e | electrolyte |
| eff | effective value |
| feedout | outlet of the feed tube |
| fuel | fuel gas |
| hyd | anode reaction of $H_2$: eqn (2-3) |
| hyd·oxy | electrochemical reaction of $H_2$: eqn (2-6) |
| inlet | inlet of the cell |
| outlet | outlet of the cell |
| oxy | cathode reaction of $O_2$: eqn (2-5) |
| rad | radiation |
| re | reduced value |
| s | solid |
| steam | steam reforming reaction: eqn (2-1) |
| shift | water-gas shift reaction: eqn (2-2) |
| 1 | inner surface of the cell tube |
| 2 | outer surface of the feed tube |
| $e, w, n, s, Ee, Ne, Se$ | velocity grid points |
| $E, W, N, S$ | normal grid points |
| $u, u', d, d'$ | grid points for $i$ |
| $U, U', D, D'$ | grid points for $V$ |
| $P, P'$ | intended grid points |
| $P_1, P_2$ | intended position on the cell/feed tube surfaces |
| $PP'$ | electrolyte between the grid points $P$ and $P'$ |

## Superscripts

| | |
|---|---|
| $P'$ | superscript for $a$ and $b$ in the algebraic equations of $P'$ |
| $U_x$ | superscript for $a$ and $b$ in the algebraic equations of $U_x$ |
| $U_r$ | superscript for $a$ and $b$ in the algebraic equations of $U_r$ |
| $V$ | superscript for $a$ and $b$ in the algebraic equations of $V$ |
| $*$ | guessed value |
| $'$ | correction value |

# Acknowledgments

This study has been carried out over the last three years I spent in Heat Transfer Laboratory and Thermal System Engineering Laboratory of Kyoto University. I would like to express my sincere gratitude to Professor Kenjiro Suzuki for his invaluable guidance on my first two-year research in the Heat Transfer Laboratory. I would also like to show my full appreciation to Professor Hideo Yoshida for his experienced advice and suggestions in the Thermal System Engineering Laboratory over the last one year.

I wish to express my cordial thanks to Dr. Hiroshi Iwai for his general assistance and suggestions during all the three years. I also have to thank my predecessors — Dr. Pei-Wen Li and Mr. Hajime Komori — for their achievements and practical advice on the basic parts of the computational code used in the present study. I could not have achieved success in this study without their cooperation.

I am also grateful to all the members of the two laboratories, particularly Dr. Zheng Dang, Mr. Tatsuo Ishikawa and Mr. Daisuke Shiomi, for many valuable discussions on SOFCs. Special thanks also goes to the ex-members of the Heat Transfer Laboratory — Professor Kazuyoshi Nakabe, Dr. Peter L. Woodfield, Dr. Kazuya Tatsumi and Dr. Takuto Araki — for their thoughtful advice and kindness.

Finally, I would like to express my best thanks to my parents for their understanding and continuous support throughout my six-year study in Kyoto University.